CONTROL OF CONSTRAINED MOVING-BOUNDARY PROCESS WITH APPLICATION TO STEEL CONTINUOUS CASTING

BY

ZHELIN CHEN

DISSERTATION

Submitted in partial fulfillment of the requirements
for the degree of Doctor of Philosophy in Mechanical Engineering
with a concentration in Computational Science and Engineering
in the Graduate College of the
University of Illinois at Urbana-Champaign, 2020

Urbana, Illinois

Doctoral Committee:

Professor Joseph Bentsman, Chair
Professor Brian G. Thomas
Professor Prashant Mehta
Professor Eduard-Wilhelm Kirr
Professor Chenhui Shao

ABSTRACT

Continuous casting is an important engineering process producing nearly all steel currently used worldwide. Regulation of the steel temperature through the water spraying during casting critically affects the final product quality as well as operational safety. Most of the cooling spray control techniques currently used in the steel industry are effectively open-loop due to the lack of reliable measurements to enable feedback. Namely, the high temperatures, the variable surface emissivity, the scale formation, and the steam from water spray make accurate measurements of the steel surface temperature impossible with current technology. Another difficulty is the inadequacy of the existing feedback control techniques for coping with the nonlinear moving boundary problem dynamics. The present work provides several key building blocks towards a comprehensive solution of the continuous steel casting feedback control problem.

In the first part of this dissertation, a mathematical model of the process and a state-of-the-art industrial control system are introduced. The steel casting process can be described as a single-phase Stefan problem under some simplifying but practically justified assumptions on the unknowns. The temperature and the shell growth are controlled by the steel surface heat flux generated by the cooling sprays. In the industrial control system, a real-time computational model of the caster is used as a software sensor to estimate the temperature and the shell thickness of the strand. The model is calibrated through the steady-state measurements of the thin-slab caster from reliable pyrometer measurements outside the spray zone as well as the metallurgical length detection trials and verified by comparing model predictions with the transient measurements of the roll forces.

In the second part, the control problem is studied for the simpler, but still fundamentally nonlinear PDE model of the caster. A boundary-sensing-based observer that under an additional physically valid assumption provides a stable reconstruction of the full system state is proposed. By combining a full state enthalpy-based controller with an observer, an output feedback control law is presented, and the stability of the closed-loop output feedback system is proven. This estimation framework is then extended in the current work to a more realistic sensing setting. Online calibration using a single discrete-in-time temperature measurement is introduced to remove the estimation error arising due to the mismatch of a single unknown parameter in the model. One-phase Stefan problem with hysteresis induced by the interaction of the cooling water sprays with the hot surface under Neumann boundary actuation is then considered. A hysteresis-compensating full state feedback control law and an output feedback control law are developed for this problem by introducing the hysteresis inverse. An optimal control approach for minimizing the metallurgical length deviation during casting speed increase under constraints on the secondary cooling flow rates for the continuous steel casting process is proposed. A cost function reflecting the tracking error of a reference shell thickness is chosen, and the control objective is formulated as the minimization of this cost function under the spray rate constraints.

In the third part, the verified transient 2-D thermal solidification model of the process, ConOffline, is used to assess the effect of the transient thermal behavior on the product quality in the continuous casting of steel.

ACKNOWLEDGMENTS

This thesis has been completed with the help of many people. In my research and writing, I have borrowed the ideas and the results of hard work from numerous others whose names are not on the front page. I will try to thank as many as I can below, but the list is by no means complete. I apologize to those whose names I forgot to include.

I would like to express my deepest gratitude to my advisor, Professor Joseph Bentsman, for his patience, enthusiasm, immense knowledge, and providing me with an excellent atmosphere for doing research. He is the person who led me into the field of control and optimization, his suggestions helped me in building my background, and his guidance helped me at all times in carrying out research and writing of this thesis.

My co-advisor, Professor Brian G. Thomas, has always been there to listen and give advice. The door to Prof. Thomas's office was always open whenever I ran into a trouble spot or had a question about my research or writing. After his move to Colorado School of Mines, Prof. Thomas has been always available via email and phone calls. I am very grateful to him for those long discussions that helped me sort out the technical details of my work and the high standards he set for his students in their work. Especially, I am sincerely grateful for his efforts in helping me improve this thesis. Also, I am grateful for the opportunity to work in the Continuous Casting Center at the Colorado School of Mines.

I need to thank Dr. Kai Zheng, Xiaoxu Zhou, Dr. Bryan Petrus, and all those people who have worked on the programming of the CONONLINE system for their previous contribution. Without them, the present work would not have been possible.

Dr. Bryan Petrus, a former Ph.D. student at the University of Illinois and now working at Nucor Decatur, taught me how to use CONONLINE and provided me with a lot of help, not only in research but also in daily life.

Madeline Rembold, Bob Williams, Wes Rollings, Madison Milligan, Daniel Stephens, Franny Gorius, Kris Sledge, and many others from Nucor Decatur are gratefully acknowledged for their kind support of the project and their warm welcome of my internship there.

This work has been funded in part by the National Science Foundation under Grants CMMI-1300907 and CMMI-17-47876.

My sincere thanks go to the sponsors of the Continuous Casting Center, both in particular for funding this research, and in general for funding a group where I have been able to watch researchers at a major research university work with the best operators, engineers, and metallurgists in the industry.

Thank you to my fellow lab mates in Control System Design and Application Lab and Continuous Casting Center: Dr. Insu Chang, Dr. Bryan Petrus, Oyuna Angatkina, Dr. Huirong Zhao, Ya Wang, Willian Drennan, Donnie Xu, Lu Chen, Dr. Cho, Matt Zappulla, Olia Hamed, Dr. Hyunjin Yang for their occasional help and continuing friendship.

I also want to thank the IT staff who maintained all the computers in my lab, especially Michael Marks, for helping me set up new Linux computers.

I am also thankful to all the staff of the Department of Mechanical Science and Engineering at the University of Illinois, including Kathy Smith, Laurie Macadam, Emily Lange, Marcia Mathis, Robbie Vermillion, and others for their various forms of support during my study.

Most importantly, none of this would have been possible without the love and support from my parents and my wife. They have been a constant source of love, care, support, and strength all these years. I would like to express my heartfelt gratitude to them.

At last special thanks to my daughter Olivia Chen for bringing a new meaning to my life.

To my daughter, Olivia Chen

To my wife, Yuqiao

To my parents, Jinqian Chen and Saiting Zhang

for their love and support.

TABLE OF CONTENTS

CHAPTER 1. INTRODUCTION 1

1.1 CONTINUOUS STEEL CASTING PROCESS 1
1.2 MOTIVATING EXAMPLE 4
1.2.1 Straightening/Bending cracks 6
1.2.2 Whale formation 7
1.2.3 Segregation 8
1.2.4 Hysteresis due to boiling 10
1.3 PREVIOUS RESULTS IN CONTROL LITERATURE 10
1.4 CONTRIBUTION AND ORGANIZATION 13

CHAPTER 2. MATHEMATICAL FORMULATION 16

2.1 HEAT TRANSFER IN THE SOLIDIFYING STEEL 17
2.1.1 Effective specific heat 18
2.1.2 Model simplification: scaling analysis 19
2.1.3 Lagrangian (or material) coordinate system 21
2.2 BOUNDARY CONDITIONS 24
2.2.1 Eulerian coordinates 24
2.2.2 Lagrangian coordinates 25
2.3 STEFAN FORMULATION 26
2.3.1 Stefan problem 27
2.3.2 Existence and uniqueness of solution 30
2.3.3 Enthalpy formulation 33

CHAPTER 3. MATHEMATICAL FORMULATION 34

3.1 HEAT TRANSFER MODEL: CON1D 34
3.2 SOFTWARE SENSOR: CONSENSOR 37
3.3 INDUSTRIAL CONTROL SYSTEM: CONONLINE/CONOFFLINE 41
3.4 MODEL VALIDATION 43
3.4.1 Thermal shrinkage model 43
3.4.2 Casting conditions 46
3.4.3 Steady-state simulation results 48
3.4.4 Transient simulation results 52

CHAPTER 4. OUTPUT FEEDBACK CONTROL 55

4.1 REFERENCE ERROR SYSTEM 56
4.2 PRELIMINARIES AND NOTATION 57
4.3 ESTIMATION AND OUTPUT FEEDBACK 59
4.4 DISCRETE-IN-TIME RECALIBRATION 68
4.4.1 Calibration of Stefan problem 69
4.4.2 Discussion and simulation 73

CHAPTER 5. SPRAY COOLING CONTROL UNDER PROCESS INPUT HYSTERESIS 75

5.1 HYSTERESIS DUE TO BOILING 76
5.2 FULL-STATE FEEDBACK CONTROLLER DESIGN WITH THE KNOWN HYSTERESIS 78
5.2.1 Controller design via hysteresis inverse 78
5.2.2 Existence of solution 78
5.2.3 Enthalpy-based controller design 79
5.2.4 Numerical simulation 82
5.3 ENTHALPY-BASED OUTPUT FEEDBACK CONTROL WITH KNOWN HYSTERESIS 85
5.3.1 Observer design 85
5.3.2 Output feedback control 88
5.3.3 Numerical simulation 90
5.4 RECALIBRATION DESIGN FOR UNKNOWN HYSTERESIS 91
5.4.1 Hysteresis model 92
5.4.2 The hysteresis inverse 94
5.4.3 Recalibration design for the full-state feedback control 97
5.4.4 Recalibration design for output feedback control 103
5.5 SUMMARY 105

CHAPTER 6. OPTIMAL CONTROL FOR METALLURGICAL LENGTH MAINTENANCE 107

6.1 SINGLE-SLICE OPTIMIZATION PROBLEM 108
6.1.1 Problem formulation 108
6.1.2 Existence of optimal controls 110
6.1.3 Derivation of the optimality system 111
6.2 MULTI-SLICE OPTIMIZATION PROBLEM 114
6.2.1 Control problem formulation 114
6.2.2 Derivation of the optimality system 115
6.3 NUMERICAL APPROACH 117
6.4 NUMERICAL RESULTS 120
6.4.1 Single-slice optimization 121
6.4.2 Two-slice optimization 123
6.5 SUMMARY 124

CHAPTER 7. INVESTIGATING THE CENTERLINE BRIDGING WITH CONOFFLINE 125

7.1 THE CENTERLINE BRIDGING 126
7.1.1 A centreline bridging example 126
7.1.2 Steps in the bridging mechanism 128
7.2 PARAMETRIC STUDIES 129
7.2.1 Effect of the speed drop size 130
7.2.2 Effect of the strand thickness 131
7.2.3 Effect of incrementally dropping speed 132
7.2.4 The effect of a steel alloy 134
7.2.5 Effect of the spray cooling control 135
7.3 SUMMARY 141

CHAPTER 8. DYNAMIC MODELING OF THE UNSTEADY BULGING WITH CONOFFLINE 142

8.1 A Dynamic Bulging Model 143
8.1.1 A steady bulging model 143
8.1.2 A dynamic bulging model for the unsteady bulging 144
8.1.3 A stopper rod flow model 148
8.1.4 The computational procedure 149
8.2 Simulation Results and Discussion 150
8.2.1 The casting conditions 150
8.2.2 The stopper rod flow model results 151
8.2.3 The dynamic bulging model results 153
8.3 Summary 155

CHAPTER 9. SUGGESTION FOR FUTURE WORK 157

9.1 Motion Planning for Steel Casting 157
9.2 Developing Realistic Hysteresis Operator and Proving the Convergence 159
9.3 The Spray-zone Control 159
9.4 Extended Application 160

APPENDIX A. NUMERICAL SIMULATION BACKGROUND 161

APPENDIX B. MATHEMATIC BACKGROUND 163

B.1 Lagrangian and Eulerian Coordinates System 163
B.1.1 Lagrangian description 163
B.1.2 Eulerian description 163
B.1.3 Material derivative 164
B.2 Lyapunov Stability and LaSalle Invariance 165
B.3 Infinite–dimensional Systems 166
B.4 Useful Inequalities and Estimates 169

REFERENCES 171

CHAPTER 1.

INTRODUCTION

1.1 Continuous Steel Casting Process

Although steel continuous casting was introduced over 60 years ago, it is still the most common method of casting steel today. In 2016, 96.2% of the steel produced worldwide was made by continuous casting [1]. A schematic of the steel continuous casting process is shown in Figure 1. During this process, the molten steel flows from a ladle, through a tundish, into the mold, where the molten steel is maintained at a constant height through a mold level controller. In the mold, the molten steel circulates in the liquid pool and freezes against the water-cooled copper mold walls to form a solid shell. The solidifying shell and the liquid steel inside it continuously move out of the mold at a rate called the 'casting speed' that matches the rate of the incoming molten steel flow.

After the mold exit, the solidifying shell, which acts as a container to support the remaining liquid, enters the spray cooling region. In this region, the steel strand is supported by a series of rolls, which hold the strand under the ferrostatic pressure, with the latter causing the shell bulging between the rolls. Water and air mist sprays cool the surface of the strand between rolls to maintain its surface temperature until the molten core solidifies. The distance from the meniscus to the point of full steel solidification is called the metallurgical length (ML), as illustrated in Figure 1. After the center is completely solid (at the ML), the steel strand can be cut into slabs for future processing and shipment.

The continuous steel casting process has two cooling stages: mold (or primary) cooling and water (or secondary) cooling. Heat transfer at the metal/mold interface in the mold is referred to as the primary cooling, and the heat transfer that happens in the spray cooling region is called the secondary cooling [2]. Heat is removed through the slag-formed gap between the solidifying steel shell and the mold wall while in the mold, and by natural convection, radiation, spray nozzle cooling (based on water flux), and conduction through contact with the containment rolls while in the secondary cooling region. All of the above are discussed in detail in[3], [4], but the heat transfer in the secondary cooling region deserves special mention since it highly influences the product quality and process safety.

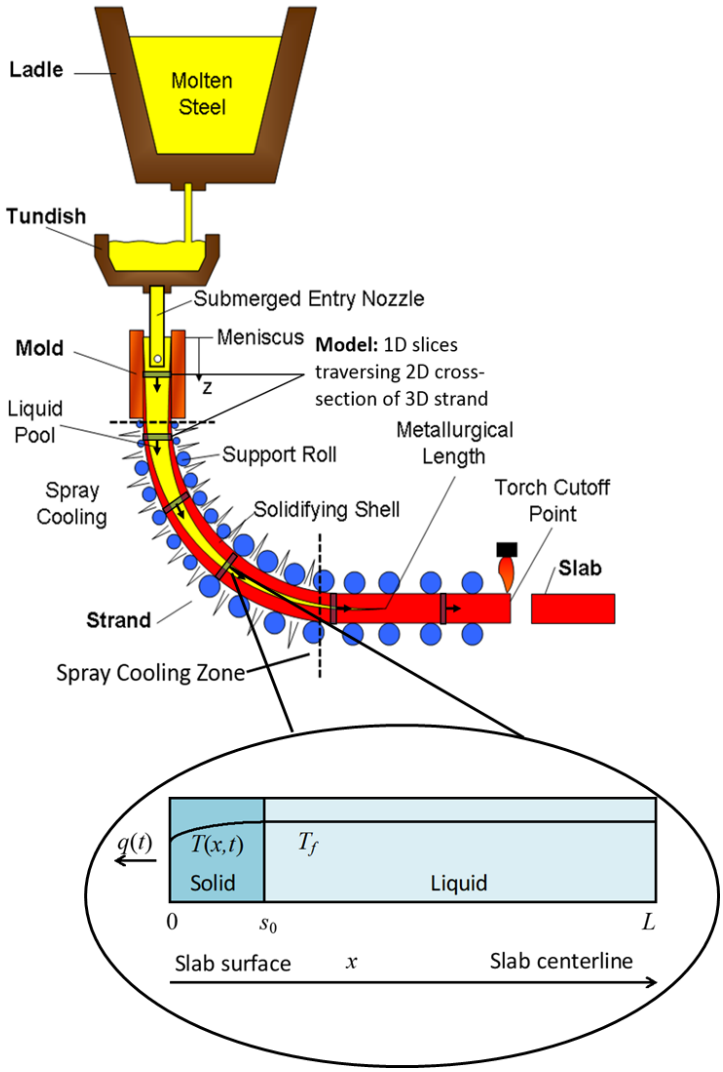

Figure 1. Schematic diagram of continuous steel caster and simulation domain of process model.

The control of the secondary cooling water sprays has a significant effect on steel quality and operational safety. In most continuous steel casters, the mold is vertical at the top, and the caster is shaped to bend the material to horizontal profile so that it may be moved directly out of the machine to be shipped, stored, or further processed elsewhere in the mill. The supporting rolls in the secondary cooling region push on the steel strand surface to act against the ferrostatic pressure of the liquid steel. If the steel is under-cooled and not fully solid exiting the containment provided by the supporting rolls, the pressure becomes large enough to bulge the steel shell outward,

distorting the shape of the steel and causing both the quality and the safety problems. At the same time, over-cooling the steel can cause other defects. The ductility of steel varies with temperature, and transverse cracks may be created at the bending and unbending area of the caster, where tensile stresses are greatest due to the shaping of the strand, if the temperature of the strand surface is within low ductility region. The following section discusses these and many other motivations in detail.

Many steel quality and productivity goals can be met by regulating the strand temperature using the secondary-cooling water sprays. This would appear to be a classical application for feedback control. Yet, most steel mills currently use only open-loop methods for controlling the cooling water sprays[4]. This is because casting presents several key challenges: first, the process is inherently distributed and non-linear. That is, the entire distributed temperature profile must be controlled to meet quality and safety requirements; second, while the classical heat equation is perhaps the most well-studied partial differential equation (PDE) in the burgeoning field of distributed parameter control systems, the material in a caster is solidifying. This makes the system non-linear, and not a small perturbation of the linear heat equation. Therefore, existing methods for controlling linear parabolic PDEs do not apply. As the continuous casting process is the most widely used method for steel making, small improvements in the spray cooling method that improves the steel quality can lead to a big impact worldwide.

1.2 Motivating Example

Starting a continuous casting machine involves placing a dummy bar (a curved metal beam) up through the spray chamber to close off the base of the mold. Molten steel is poured into the mold and once the solidified shell is thick enough, it is withdrawn with the dummy bar; this is

called a ‘startup’. When it is time to shut down the caster, steel flow into the mold is stopped, and the remaining liquid-filled steel shell will continue to solidify and be withdrawn from the caster by the drive rolls. This process is called a ‘tailout’. The steel produced during startups and tailouts is usually discarded and later re-melted due to quality issues. After startup, whenever a ladle is almost empty, a new ladle of molten steel will replace the previous ladle, and the tundish would act as a steel reservoir between the ladle and the mold to distribute the molten steel into the mold. Depending on the customers’ needs, steel with different width and chemistry is ordered. These steel orders are joined together as a schedule, which typically includes sequences of different ladles to maximize productivity and minimize loss due to quality problems. One of the worst catastrophic process failures that can occur during the continuous casting process is the breakout of liquid steel. Breakout occurs when solidifying strand steel shell ruptures or tears beneath the mold. To avoid the occurrence of the breakout, it is critical to detect improper solidification of the steel shell, which can be achieved through the breakout detection system.

In the continuous steel casting process, most defects form during a transient or change in the normally steady process. Casting speed may change during a number of casting procedures like startups, tailouts, ladle changes, schedule changes, breakout detection system alarms, upstream delays in steel melting and making, and delays downstream during rolling. To prevent defects, as the first step, it is crucial to understand how these events affect the dynamic thermal behavior of the solidifying steel, including the metallurgical length and the strand surface temperature.

For many operations in the continuous casting process, the surface temperature profile is very important, because it controls surface crack formation. These operations prefer to maintain surface temperature during casting speed changes and transitions. In other operations, the metallurgical length has a considerable influence on the operation layout. Such influence extends to the choices

of unbending location to prevent cracks, support zone geometry to prevent whales, and, especially, the soft reduction equipment placement for preventing the centerline segregation. Thus, for these operations, it is very helpful to minimize fluctuations in metallurgical length during transitions and other transients.

1.2.1 Straightening/Bending cracks

As shown in Figure 1, the mold and the top of the secondary cooling zone are vertical, and the caster is shaped to bend the solidifying steel to the horizontal direction upon exiting the machine. During bending, the upper surface has compressive strains and the lower surface has tensile strains, and the strains are reversed during straightening. Bending and straightening introduce relatively large axial strains and tensile stresses in the solid shell, which can create transverse cracks if the steel is too brittle. For this reason, the steel should not be fully solid in either the bending or straightening regions of the machine, so that it be easier to deform.

In addition, it is known that the ductility of steel varies with temperature. There are three distinct temperature ranges where steel has low strength and/or ductility and therefore is susceptible to cracking: the high temperature zone from around $1340^{o}C$ to solidus, the intermediate temperature zone from $800^{\circ}C$ to $1200^{\circ}C$, and the low temperature zone from $700^{\circ}C$ to $900^{\circ}C$ [5]. Bending or straightening cracks can form if straightening or bending operations are carried out for a section with a liquid center or when the center is solid, but above $1340^{\circ}C$ [5].

The ductility of steel is strongly temperature-dependent, with the actual temperature of minimum ductility depending on grade. Therefore, a common practice for preventing these transverse surface cracks is to ensure that the surface temperature in the bender or straightener, where tensile stresses are greatest, is either below or above the low-ductility region.

1.2.2 Whale formation

Once the solidifying steel slab, referred to as the strand, exits the mold, it enters the secondary cooling region where a series of rolls provide the strand support. The rolls serve two primary purposes: they allow the strand to move through the caster without sticking, and they hold the strand shape by preventing the strand from excessively bulging under the ferrostatic pressure.

The distance from the meniscus to the last supporting rolls is called the machine length. The metallurgical length, i.e. the distance from the meniscus to the location where the steel is completely solid, should be shorter than the machine length. Otherwise, a defect known as 'whale' might form. It is evident that if the metallurgical length extends beyond the machine length, the final portion of the partially solidified strand will no longer be supported by the rolls at the strand broad faces. The ferrostatic pressure transmitted from the meniscus via the liquid pool acting internally on the steel shell will then cause this unconstrained portion of the strand to bulge out excessively, as illustrated in Figure 2.

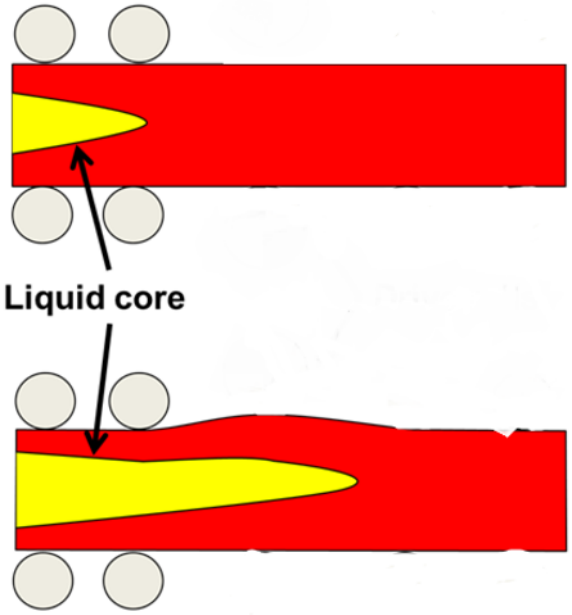

Figure 2. Illustration of the formation of a whale.

When a whale happens, the bulged steel cannot fit through the cut-off device located at the end of the caster. The casting process must then be stopped until the steel is completely solid, and the whale subsequently cut up and removed before casting can resume. In the worst cases, liquid steel could rupture the shell and spout through the crack, potentially causing severe damages or serious injuries [4]. To help prevent this from happening, the casting speed and the water sprays in the secondary cooling region must be controlled to cool the steel sufficiently to make sure that the metallurgical length is shorter than the machine length.

1.2.3 Segregation

The centerline segregation is a defect that is related to a non-uniformity of chemical composition during solidification. It appears as a line of impurities near the centerline of the slab, in which region cracks could appear and will be very harmful when the slab is rolled into thin plates [6]. The most common ways of evaluating centerline segregation in the industry are sulfur printing and macro etching [7]. Sulfur printing reveals the size and the distribution of the mainly manganese sulfur inclusions in the steel. This method is insensitive when applied to the low sulfur steels (less than about 0.006 wt%) [8]. An example of a sulfur print is shown in Figure 3. Macro etching is a method of revealing the centerline segregation by the chemical etching using a range of possible etchants [7]. The image from macro etching is similar to that of sulfur printing

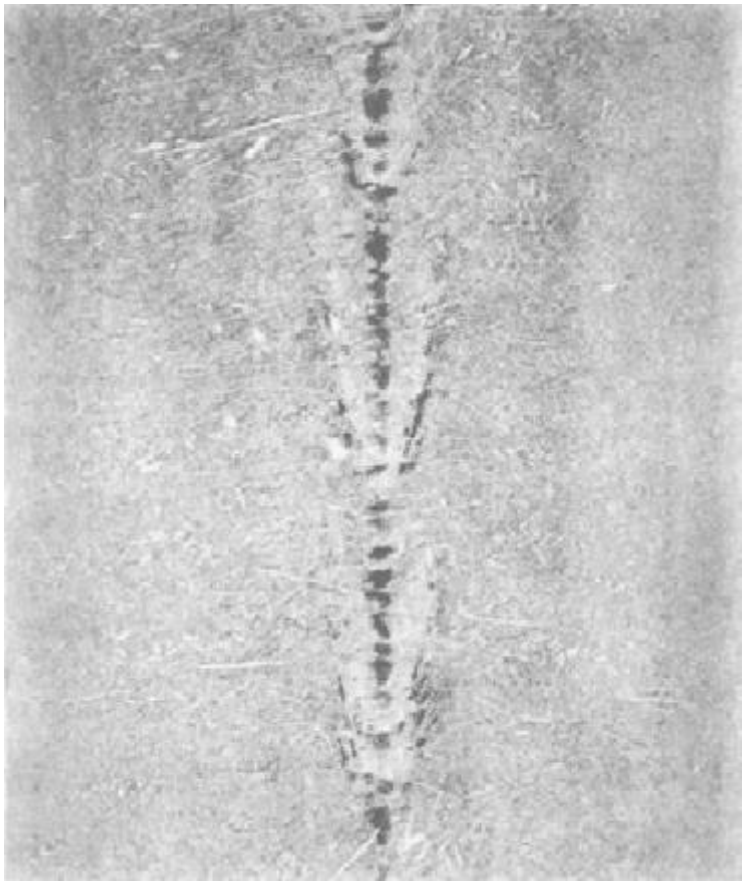

Figure 3. An example of Sulfur print of a longitudinal section showing centerline segregation [9].

During the solidification process, the steel will shrink while transitioning from liquid phase to solid phase. Therefore, the centerline is susceptible to segregation and other defects if the roll gap profile does not match the desired shrinkage. One method to reduce the centerline segregation is to apply soft reduction in the casting machine at the segments prior to the final point of solidification. The purpose is to compensate for the solidification and the thermal shrinkage by softly compressing the strand in the final solidification area and in that way to prevent the solute-enriched melt from flowing toward the center and thus to reduce the centerline segregation and porosity [10]. The choice of the location of the soft reduction region depends greatly on the shell thickness profile and the metallurgical length. If the steel is completely solid when the slab enters the soft reduction region, then the rolls experience large forces from the solid steel, which could

damage both the slab and the rolls. Therefore, it is essential to make sure the metallurgical length stays within the soft reduction region during the casting conditions changes.

1.2.4 Hysteresis due to boiling

In the secondary cooling region, the heat extraction by the cooling water is governed by the water boiling phenomena, which greatly depend on the temperature. The cooling water droplets impinge onto the hot steel surface and vaporize immediately to form a stable steam layer, which will prevent the water droplets from coming in contact with the steel strand surface and decrease the heat removal. An experiment was done to determine the boiling curve from 200 ^{o}C to 1200 ^{o}C and then back to 200 ^{o}C for a Pt-specimen under air-mist spray nozzles [11]. The curves (Figure 10 in [11]) reveal the existence of hysteresis due to boiling in the water cooling process, as time is needed for the steam layer conditions to change. To the best of our knowledge, the control of the solidification process with the hysteresis effect of the heat extraction has never been considered in any other control literature.

1.3 Previous Results in Control Literature

The continuous steel casting process can be described in a simplified form by a 1D single-phase Stefan problem partial differential equation (PDE) [12], [13] or a more detailed enthalpy formulation [3]. A set of simplified 1D models could be assembled into a 2D cross-section transient model of the 3D slab solidification process through spatial step interpolation [4]. A 2D model could then be used to estimate the distributed temperature profile within the strand in real-time employing only the boundary measurements.

In the control literature of the Stefan problem, there have been many techniques suggested. The approach used in [14] is to solve the inverse Stefan problem, i.e. impose a desired trajectory of the boundary and determine a temperature profile computationally. This would satisfy the whale constraints but could still result in temperature-related cracks. The papers [13], [15], attempt to deal with the distributed 1-D control problem using Lyapunov stability analysis on the underlying nonlinear Stefan PDE. The follow-up paper [16] gave some extensions to improve the fidelity of the control-oriented model with respect to the actual continuous casters. These papers are the first, to our knowledge, results giving control of both the temperature (distributed throughout the material) and the solidification front at the same time.

In [17], the authors proposed a full-state geometric control law that ensures the exponential convergence of the temperature, however, the proposed control law requires the knowledge of the derivative of the free boundary which is impossible to measure in many solidification process, and did not prove the convergence of free boundary. Also the problem formulation in [17] takes a fixed free boundary setpoint as the reference, resulting in the temperature converges to the melting temperature, while in real casting process, often the time-varying free boundary and the distributed temperature reference are needed to ensure the product quality and the operational safety. The proof provided will not hold for that problem considered in this work. In [18], the authors proposed a full-state feedback control law, an observer design, and the associated output feedback control law of both Neumann and Dirichlet boundary actuation via the backstepping method for a one-phase Stefan problem. The proposed control laws ensure the convergence of the moving boundary and the temperature to a reference setpoint, which is not enough for solidification process like continuous casting of steel which requires the convergence of the temperature distribution and the moving boundary profile to a reference profile instead of a single point, like the problem

considered in [13]. The Neumann boundary actuation proposed in [18] is essentially the enthalpy-based control law proposed in [13]. The observer designed in [18] requires the measurements of the moving boundary location and its derivative, which are not applicable for the continuous casting process considered in the current work, where typically only surface temperature measurement is available. In [19], a similar observer and output control law are proposed for the sea-ice melting problem. The proposed observer also requires the measurements of the moving boundary. These papers follow a familiar idea in control systems: the system internal energy provides guidance to formulating a Lyapunov functional for controller design. For distributed parameter systems, common Lyapunov functionals are the L_2 norm of the temperature, and the Sobolev norms that include the L_2 norms of the temperature and one or more of its spatial derivatives. These norms generate Hilbert spaces, which allow for many useful results from functional analysis to be used in proving boundedness and well-posedness.

The optimal control of the Stefan problem has been considered in several publications. In [20], the authors first proposed the optimal control law for a one-phase Stefan problem to maximize the interface movement at a certain time through boundary input, and then proved the control law uniqueness. The problem considered in the present work is more complicated, and optimal control cannot be proposed beforehand. Hinze and Ziegenbalg [21] represent the interface in a two-phase Stefan problem as the graph of a function over a rectangular domain. They use the temperature at the boundary of the container as the control variable and aim to track the desired interface motion. However, Dirichlet boundary control is not implementable in continuous steel casting, since cooling is accomplished through boundary heat flux extraction corresponding to Neumann boundary condition.

Hysteresis effect, which can be characterized as a special type of memory-based relation between an input signal $v(t)$ and an output signal $w(t)$, arise in different areas of science, such as physics, engineering, economics, and biology. There is an extensive body of research concerning the modeling of hysteresis. The common models consist of Duhem model, Bouc-Wen model, Prandtl-Ishlinskii model, and Preisach model [22]–[24]. A generic approach to control hysteresis systems is to combine inverse compensation with feedback [25]–[27]. While many control schemes have been proposed for nonlinear ordinary differential equation (ODE) system models with hysteresis [20], [28], [29], the control of PDE systems with hysteresis is studied in relatively few publications. Friedman and Hoffmann [30] considered optimal control of the free boundary of a two-phase Stefan problem with hysteresis-type boundary conditions. Periodic control of the two-phase Stefan problem with Dirichlet boundary control with hysteresis was considered in [31].

1.4 Contribution and Organization

In Chapter 2, two process models are described: a mathematical model of the process and a model associated with a state-of-the-art industrial control system. The process can be described as a single-phase Stefan problem under some simplifying but practically justified assumptions on the unknowns. In this fundamentally nonlinear PDE, solidification is defined by a moving boundary separating the material into the liquid and the solid spatial sub-domains. The temperature evolves according to the usual linear parabolic diffusion equations inside each sub-domain. The boundary itself moves over time according to an energy balance equation involving the discontinuous temperature gradients at the boundary called the Stefan condition. In Chapter 3, the industrial control system, a real-time computational model of the caster is used as a software sensor to estimate the temperature and the shell thickness of the strand, since the measurements from the

physical sensors are impractical due to the complex nature of the casting process. Using the model for feedback, several control methods are developed or modified to give a satisfactory performance under different operational objectives. The model is calibrated through the steady-state measurements of the thin-slab caster from reliable pyrometer measurements outside the spray zone and metallurgical length detection trials, and verified by comparing the model predictions with the transient measurements of the roll forces in another caster.

In Chapter 4-6, the control of the process is studied. In Chapter 4, a boundary-sensing-based observer is proposed that under an additional physically valid assumption provides a stable reconstruction of the full system state. Finally, by combining a full state enthalpy-based controller with an observer, an output feedback control law is presented, and the stability of the closed-loop output feedback system is proven. These estimation frameworks are then extended in the current work to a more realistic sensing setting. An online calibration using a single discrete-in-time temperature measurement is introduced to remove the estimation error arising due to a mismatch of a single unknown parameter in the model. In Chapter 5, the one-phase Stefan problem with a water cooling hysteresis under the Neumann boundary actuation is considered. The full state feedback control law for this problem was designed in an earlier work and proved to provide asymptotic convergence of both the temperature distribution and the solidification front. However, for the casting process, only the boundary sensing is available. To address the latter problem, an hysteresis compensated observer is proposed. The stability of the observer is proved with the Lyapunov method. Finally, an output feedback control law is proposed and proved to ensure an asymptotic convergence of the temperature and the solidification front errors to zero. In Chapter 6, an optimal control approach for minimizing the metallurgical length deviation during the casting speed increase under constraints on the secondary cooling flow rates for the continuous steel

casting process is proposed. A cost function reflecting the error in the tracking of a reference shell thickness is chosen, and the control objective is formulated as the minimization of this cost function under the spray rate constraints.

In Chapter 7, the validated industrial model is used to perform computational experiments on the generation mechanism of the centerline bridging. The latter occurs near the final solidification at the metallurgical length of a caster, when the two solidification fronts touch, entrapping a pocket of liquid downstream. Shrinkage of this entrapped liquid leads to porosity and the centerline segregation problems. In Chapter 8, the ConOffline model is combined with a stopper-position-based flow model (PFSR), developed at the Colorado School of Mines [32] to investigate the mold level fluctuations in a thin-slab caster under the real casting conditions. The model is verified by comparing the simulation results with the transient measurements in a commercial thin-slab caster. In Chapter 9, suggestions for the future work are offered.

CHAPTER 2.

MATHEMATICAL FORMULATION

Several mathematical descriptions of the temperature and solidification in a continuous caster are discussed below in this chapter. The temperature evolution of the strand in this domain is three dimensional. Computations of the temperature evolution of the strand must at least take into account heat diffusion, advection at the casting speed, and the phase.

Due to the large aspect ratio of the extruding cross-section of the strand, the heat transfer in the width direction only matters at the corner of the slab so that this coordinate axis may be ignored. For casters where this is the case, the temperature distribution may be approximated as a two-dimensional function of the distance through the slab's thickness and the casting direction. Moreover, the scaling argument given in Section 2.1.2 shows that advection in the casting direction dominates over heat diffusion in that direction. This allows for casting direction conduction to be ignored. The problem may be reposed as solving for the temperature distribution in a series of one-dimensional cross-sections through the thickness of the caster, which themselves move at the casting speed. The problem is further simplified by assuming that the temperature distribution in a given one-dimensional slice is symmetric about the center of the strand so that only the region between the center of the strand and the surface needs to be considered.

Process modeling and simplification, including the coordinate system transformation, is introduced in Section 2.1.3.

2.1 Heat Transfer in the Solidifying Steel

Figure 4(a) shows a 3-D schematic of a continuous caster. z is the axial coordinate in the casting direction, x is a span-wise coordinate through the thickness of the slab (the smaller of the two cross-sectional dimensions), and y is a span-wise coordinate through the width of the slab. The origin is at the center of the strand and the meniscus of the caster. The strand continuously moves down the caster at the casting speed while jets of water from spray nozzles imping upon the wide face of the slab.

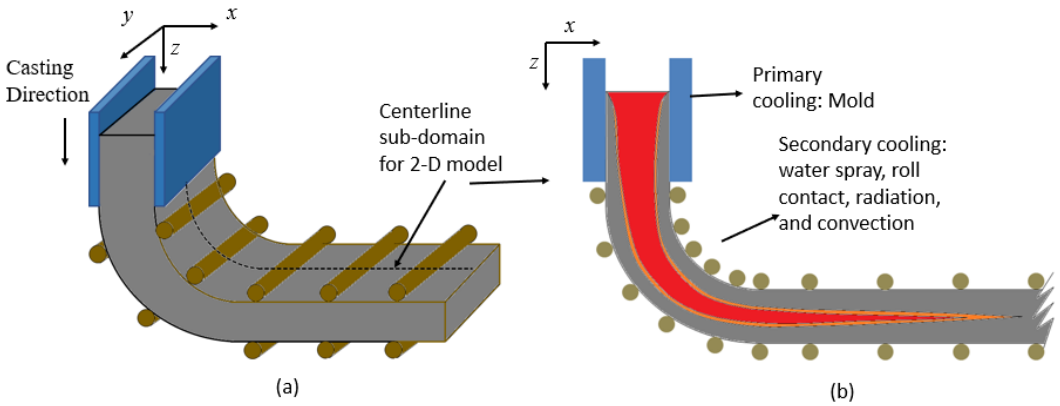

Figure 4. (a) Schematic diagram of the coordinate system and calculation domain and (b) centerline cross-section view of the steel strand.

The conservation of energy for heat diffusion can be written as:

$$\rho\left(\frac{\partial h}{\partial t}+\vec{v}\cdot\nabla h\right)=k\triangle T, \tag{2.1}$$

where $h(T)$ is the thermodynamic internal energy of the material called enthalpy, $T(x,y,z,t)$ is the temperature at a given point (x,y,z) in the cast material and $\vec{v}=(v_x,v_y,v_z)$ is the velocity of the material at that point. In a single-phase material, the enthalpy is approximately proportional to the temperature. However, for a solidifying pure material, there is a step change in enthalpy at the

melting temperature, T_f, equal to the latent heat of solidification, L_f. Altogether, this means the enthalpy can be described as a function of temperature, as shown in Figure 5:

$$h(T) = \begin{cases} c_p T & T < T_f, \\ c_p T + L_f & T > T_f, \end{cases} \tag{2.2}$$

where the density ρ, the thermal conductivity k, and the specific heat c_p are (temperature-dependent) properties of the cast material.

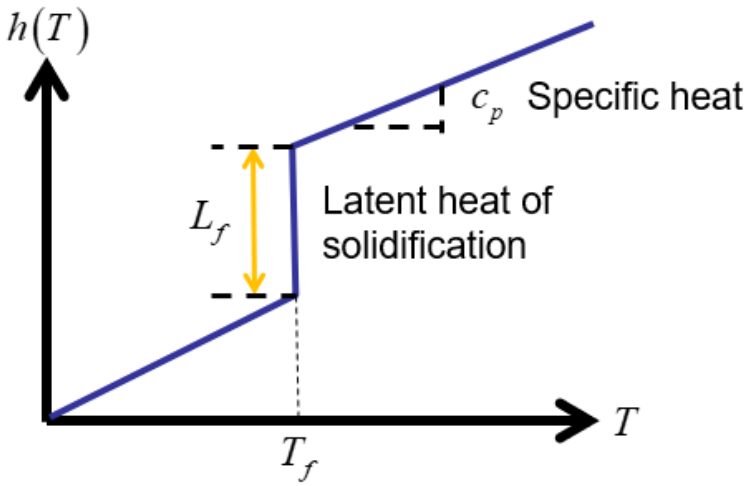

Figure 5. Enthalpy function with regard to temperature.

2.1.1 Effective specific heat

During the continuous casting of steel, other alloying elements besides iron are intentionally added during the process to modify the characteristics of steel. Therefore, as an alloy, steel does not have a single melting temperature. Instead, the steel solidifies in a range of temperatures, in which the steel is partially solid and partially liquid. One way to handle this is to mollify (2.2) slightly to give a similar function $h^*(T)$ that is differentiable. Define the effective specific heat, c_p^* to be this derivative, as shown in Figure 6.

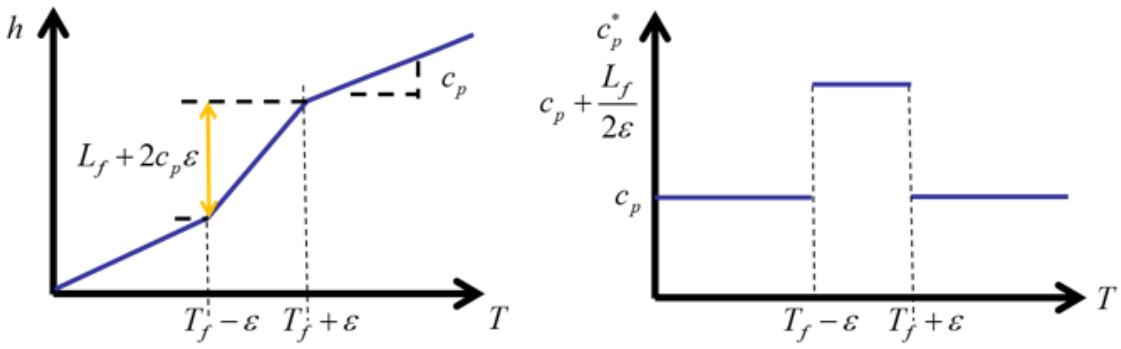

Figure 6. Mollified enthalpy function for effective specific heat.

$$c_p^* = \frac{dh^*}{dt} = c_p + L_f \frac{df_s}{dT}. \tag{2.3}$$

Then (2.1) becomes

$$\rho c_p^* (\frac{\partial T}{\partial t} + \vec{v} \cdot \nabla T) = k \triangle T. \tag{2.4}$$

2.1.2 Model simplification: scaling analysis

Expanding (2.4) yields

$$\rho c_p^* \left(\frac{\partial T}{\partial t} + v_x \frac{\partial T}{\partial x} + v_y \frac{\partial T}{\partial y} + v_z \frac{\partial T}{\partial z} \right) = k \frac{\partial^2 T}{\partial x^2} + k \frac{\partial^2 T}{\partial y^2} + k \frac{\partial^2 T}{\partial z^2}. \tag{2.5}$$

In most casters, the steel only moves along the casting direction at the casting speed v_c, i.e. $v_y = 0$, $v_x = 0$, and $v_z = v_c$. In this case, (2.5) becomes

$$\rho c_p^* \left(\frac{\partial T}{\partial t} + v_c \frac{\partial T}{\partial z} \right) = k \frac{\partial^2 T}{\partial x^2} + k \frac{\partial^2 T}{\partial y^2} + k \frac{\partial^2 T}{\partial z^2}. \tag{2.6}$$

In order to perform the scaling calculation, first, a group of dimensionless variables needs to be chosen:

$$\begin{cases} \theta = \dfrac{T - T_\infty}{T_{surf} - T_\infty}, \\ x^* = \dfrac{x}{L_x}, \\ y^* = \dfrac{y}{L_y}, \\ z^* = \dfrac{z}{L_z}, \\ t^* = \dfrac{t}{L_t}, \end{cases} \rightarrow \begin{cases} \partial T = \left(T_{surf} - T_\infty\right)\partial\theta, \\ \dfrac{\partial}{\partial x} = \dfrac{1}{L_x}\dfrac{\partial}{\partial x^*}, \\ \dfrac{\partial}{\partial y} = \dfrac{1}{L_y}\dfrac{\partial}{\partial y^*}, \\ \dfrac{\partial}{\partial z} = \dfrac{1}{L_z}\dfrac{\partial}{\partial z^*}, \\ \dfrac{\partial}{\partial t} = \dfrac{1}{t_c}\dfrac{\partial}{\partial t^*}, \end{cases} \tag{2.7}$$

where T_{surf} is the strand surface temperature, T_∞ is the ambient temperature, L_x, L_y, L_z is the characteristic length in $x-, y-, z-$directions, respectively. and L_t is the characteristic time.

Substituting (2.7) into (2.6) and simplifying the latter yields:

$$\frac{\partial\theta}{\partial t^*} + \frac{\partial\theta}{\partial z^*} = \frac{kL_z}{\rho c_p v_c L_x^2}\frac{\partial^2\theta}{\partial x^{*2}} + \frac{kL_z}{\rho c_p v_c L_y^2}\frac{\partial^2\theta}{\partial y^{*2}} + \frac{k}{\rho c_p v_c L_z}\frac{\partial^2\theta}{\partial z^{*2}}. \tag{2.8}$$

As an example, consider the ArcelorMittal 260 mm thick slab caster at the Burns Harbor CC1 caster [33] characterized as follows: L_z, the length of the whole caster, is 30 m; L_x, the half thickness, is 0.13 m; L_y, the slab width, is 1.5 m; the casting speed, v_c, is 1 m/min; density, ρ, is 7400 kg/m^3; thermal conductivity, k, is 30 W/mk; and effective specific heat, c_p^*, is 670 J/kgK, The following equation is derived by choosing $t_c = \dfrac{L_z}{v_c}$ and substituting the values into equation (2.8) :

$$\frac{\partial\theta}{\partial t^*} + \frac{\partial\theta}{\partial z^*} = 0.6445\frac{\partial^2\theta}{\partial x^{*2}} + 0.0048\frac{\partial^2\theta}{\partial y^{*2}} + 1.21\times10^{-5}\frac{\partial^2\theta}{\partial z^{*2}}. \tag{2.9}$$

The relative magnitudes of the coefficients in (2.9) suggest that it is reasonable to drop $\frac{\partial^2\theta}{\partial y^{*2}}$ and $\frac{\partial^2\theta}{\partial z^{*2}}$, which means that the heat conduction along $y-$ and $z-$ axis is negligible, compared with the axial advection and the transverse conduction. Thus, (2.6) simplifies to:

$$\rho c_p^* \left(\frac{\partial T}{\partial t} + v_z \frac{\partial T}{\partial z} \right) = k \frac{\partial^2 T}{\partial x^2}. \tag{2.10}$$

Remark 1. Dropping the term $\frac{\partial^2 T}{\partial z^2}$ means that the heat conduction in the casting direction has a negligible effect on the heat transfer from a physical point of view, it does not imply $\frac{\partial^2 T}{\partial z^2} = 0$ mathematically.

2.1.3 Lagrangian (or material) coordinate system

The heat transfer governing equation (2.10) derived in Section 2.1.2 is in Eulerian (or field) reference frame, i.e. the temperature evolution $T(x,z,t)$ of the steel is recorded at every point (x,z) in space as time varies.

Consider now a slice of steel through the slab thickness and track the temperature evolution , denoted as $T_P(x,t)$, within this slice of steel as it moves down the caster at the casting speed, as shown in Figure 7. As the steel slice advances, its temperature may change in time. Then the detailed temperature history of the entire caster, $T(x,z,t)T(x,z,t)$, can be described by tracking the temperature history of each steel slice. This representation is called the Lagrangian (or material) coordinate system.

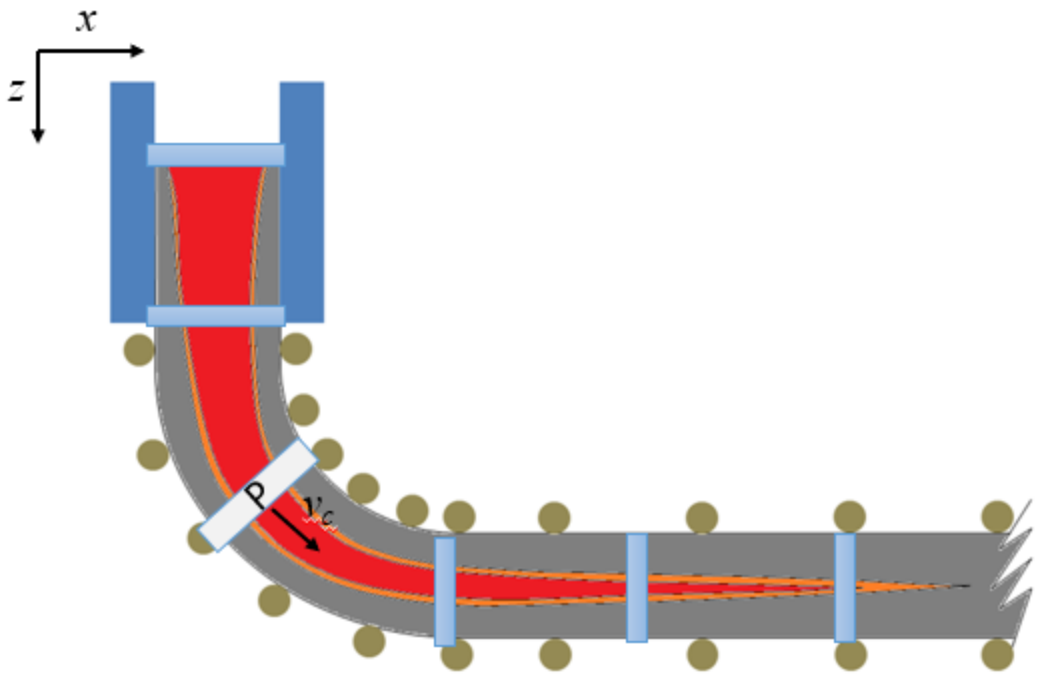

Figure 7. Example snapshot of Lagrangian description of continuous steel casting.

Consider a slice P that starts at the meniscus $z = 0$ at t_0. Then, given the speed history $v_c(t)$, the position of the slice P at all latter times, $t > t_0$ is,

$$z_P(t) = \int_{t_0}^{t} v_c(\tau) d\tau, \tag{2.11}$$

and the temperature distribution of the slice P at time t, $T_P\left(x,t\right) T_P(x,t)$ will be the temperature distribution $T\left(x, z_P(t),t\right) T(x, z_P(t), t)$ in the Eulerian coordinate system. By recording the detailed history of each moving slice, the entire temperature evolution along the caster can be generated.

2.1.3.1 Transforming time derivative

The temperature of a moving slice is identical to that observed in an Eulerian frame at that same time and the slice position. This suggests that we should be able to write the time rate of

change following a slice in terms of Eulerian variables. Given casting speed, $v_c(t)$, and current location, $z_P(t)$, the time rate of change of $T_P(x,t)\,T_P(x,t)$ as experienced by the moving slice *P* is

$$\frac{dT_P(x,t)}{dt} = \lim_{\delta t \to 0} \frac{T(x, z_P + v_c \delta t, t + \delta t) - T(x, z_P, t)}{\delta t}. \tag{2.12}$$

Applying the chain rule, yields,

$$\frac{dT(x, z_P(t), t)}{dt} = \frac{\partial T(x, z_P(t), t)}{\partial t} + \frac{\partial T(x, z_P(t), t)}{\partial z} \frac{\partial z}{\partial t} \tag{2.13}$$

Substitute (2.13) into (2.12) yields,

$$\frac{dT(x, z_P(t), t)}{dt} = \frac{\partial T(x, z_P(t), t)}{\partial t} + v_c \frac{\partial T(x, z_P(t), t)}{\partial z} \tag{2.14}$$

The generalized notation:

$$\underset{\text{Lagrangian}}{\frac{D}{Dt}} = \underbrace{\frac{\partial}{\partial t} + v_c \frac{\partial}{\partial z}}_{\text{Eulerian}}. \tag{2.15}$$

Therefore, by taking the material (Lagrangian) reference frame for a simulation domain: a slice through the slab thickness (x-direction), which moves with the steel in the z-direction at the casting speed, the Eulerian frame equation (2.10) can be transferred into the Lagrangian frame as follows:

$$\rho c_p^* \frac{\partial T(x,t)}{\partial t} = k \frac{\partial^2 T(x,t)}{\partial x^2}. \tag{2.16}$$

2.2 Boundary Conditions

The boundary conditions are quite complex. The top surface temperature, defined at the meniscus ($z = 0$), is to fix the steel at the pouring temperature. The effects of turbulent fluid flow in the liquid pool are neglected in this study. At the steel surface ($x = 0$), the heat is removed by the heat flux across the interfacial gap while in the mold, and by natural convection, radiation, convection to the spray water hitting the surface, and conduction contact with the containment rolls while in the secondary cooling region. All are discussed in detail in [3]. In this section, the mathematical representations of the boundary and the initial conditions of the Eulerian and the Lagrangian coordinates are discussed briefly.

2.2.1 Eulerian coordinates

The Eulerian coordinates fixate on a particular location in the caster and track the properties of the steel passing through that location. Mathematically, $T(x, z, t)$ is calculated for each location (x, z).

The temperature superheat (the temperature increment above the melting temperature) entering the mold from the tundish is typically monitored on-line at the steel plant. Therefore, the first initial condition is,

$$T(x, 0, t) = T_{pour}(x, t). \tag{2.17}$$

The second initial condition is regarding the initial temperature distribution along the caster at the initial time, i.e.,

$$T(x, z, 0) = T_0(x, z). \tag{2.18}$$

Denote the boundary heat flux at location z at time t as $u(z,t)$. Then the boundary condition in the Eulerian frame can be expressed as

$$\left.\frac{\partial T(x,z,t)}{\partial x}\right|_{x=0} = u(z,t). \tag{2.19}$$

For simplicity, the work in this paper will also assume the temperature is symmetric across the center of the strand, i.e. there is no heat transfer at the center of the slab thickness. This will simplify the notation and allow for generalization of the results.

$$\left.\frac{\partial T(x,z,t)}{\partial x}\right|_{x=L} = 0. \tag{2.20}$$

2.2.2 Lagrangian coordinates

For the Lagrangian coordinates, on the other hand, we follow a moving slice through the thickness (material point) as it moves through the caster starting at the meniscus at time $t = 0$. Then the initial condition would be

$$T(x,0) = T_{pour}(x). \tag{2.21}$$

And the heat flux at the surface would be

$$\left.\frac{\partial T(x,t)}{\partial x}\right|_{x=0} = u(t), \tag{2.22}$$

where $u(t)=u(z(t),t), z(t) = \int_0^t v_c(\tau)d\tau$ in Eulerian coordinates. No heat transfer through the centerline gives another boundary,

$$\left.\frac{\partial T(x,t)}{\partial x}\right|_{x=L} = 0. \tag{2.23}$$

2.3 Stefan Formulation

In slab casters, i.e., when the aspect ratio of the 2-D cross-sectional slice is substantial, heat transfer is dominant in the smaller span-wise dimension. Rather than model the entire 3-D domain, reasonable accuracy is achievable by modeling a 2-D centerline cross-section of the caster, as shown in Figure 1. Furthermore, inside the strand of a caster, heat is transferred by two phenomena: advection and diffusion. The former is heat transported by the actual movement of metal through the caster. The scaling analysis in the Subsection 2.1.2 shows that th advection heat transfer is much faster than the diffusion heat transfer, to the point where the latter is negligible in the casting direction.

The 3-D to 2-D dimension reduction is a reduction in space (from (x, y, z) to (x, z)). However, the 2-D to 1-D dimension reduction changes the frame of reference, and, as a result, changes the nature of the measurement. The 1-D slice model is in the Lagrangian (or material) reference frame, i.e., the slice moves with the steel at casting speed, while the 2-D centerline cross-section model is in the Eulerian coordinates. In the 2-D reference frame, a pyrometer is a point measurement in space. In the 1-D reference, a pyrometer measurement is instead discrete in time, $\int_0^{z*} \frac{dz}{v_c}$, since it is taken only when the slice passes beneath the location $z*$, where the pyrometer is installed. The change of reference frame also changes the nature of the control input, as discussed in Section 2.2.

Mathematical models of the 1-D slice will be used for this work and will be introduced in this section. For simplicity, the work in this dissertation (unless otherwise noted) will also assume the temperature is symmetric across the center of the strand. This will simplify the notation, and the

results can mostly be generalized straightforwardly. For clarity, the corresponding 2-D model will also be introduced in this section.

2.3.1 Stefan problem

2.3.1.1 Lagrangian coordinates

The Stefan problem [34] models a solidifying material, in this case, the moving 1D slice of the steel, by dividing it into two separate sub-domains, solid and liquid, as shown in Figure 8. Within each sub-domain, temperature evolves according to the usual linear parabolic heat diffusion equation. The boundary between the two domains moves according to the conservation of energy.

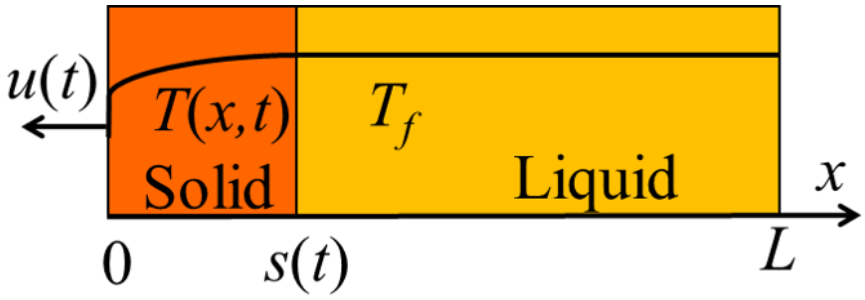

Figure 8. Example snapshot of the Lagrangian description of continuous steel casting.

Denote x to be the spatial variable, t - the time variable, $T(x,t)$ - the temperature, and $s(t)$ - the location of the liquid-solid interface. In the equations to follow, subscripts of x and t indicate partial derivatives. Then, the Stefan problem is given by

$$T_t(x,t) = aT_{xx}(x,t), \quad x \in (0, s(t)) \cup (s(t), L), \tag{2.24}$$

$$T(s(t),t) = T_f, \quad T_x(0,t) = u(t), \quad T_x(L,t) = 0, \tag{2.25}$$

$$T(x,0) = T_0(x), \quad s(0) = s_0 \tag{2.26}$$

$$\dot{s}(t) = b\left(T_x\left(s^-(t),t\right) - T_x\left(s^+(t),t\right)\right), \tag{2.27}$$

where T_f is the melting temperature, $a = \frac{k}{\rho c_p}$ is the thermal diffusivity, $b = \frac{k}{\rho L_f}$, and L_f is the latent heat. All of these physical quantities are strictly positive. The control input u is applied at the strand surface as the Neumann boundary condition.

The following assumptions are made to simplify the problem:

(A1) The initial conditions satisfy: $0 < s_0 < L$, $T_0(x)$ is continuous and non-decreasing for all $0 \le x < s_0$ and $T_0(x) < T_f$ for $0 \le x < s_0$, $T_0(x) = T_f$ for $x \ge s_0$, and

$$T(x,0) = \begin{Bmatrix} T_0(x), x \in [0, s_0), \\ T_f, x \in [s_0, L]. \end{Bmatrix} \quad . \tag{2.28}$$

That is, the material is initially below the melting temperature in the solid and equal to the melting temperature in the liquid. The first condition is physically necessary. The second condition is simplistic, but not overly so. The temperature superheat (temperature above the melting temperature) in the liquid in a caster is around 25 to 50 ^oC, while the temperature at the strand surface is hundreds of degrees below the melting temperature. Therefore, neglecting the temperature gradients in the liquid is a common simplification in modeling continuous casters. Since it limits the temperature transients to the solid area, this simplification is sometimes called the single-phase Stefan Problem. With this simplification, $s_0 = 0$.

However, in the real process, sometimes a little superheat remains in the liquid when it first touches the mold wall, so solidification starts slightly below the top of the liquid level in the mold. For other situations, the meniscus can solidify slightly so that the shell thickness at the top of the liquid level is already slightly positive. Both cases of the initial solidification front position s_0 are reasonable approximations usable in a simple model. In this work, we take the case $s_0 > 0$.

One useful consequence of (A1) is that the Stefan condition (2.27) simplifies to

$$\dot{s}(t) = bT_x\left(s^-(t), t\right). \tag{2.29}$$

(A2) $u(t)$ is bounded and piecewise continuous.

This assumption is physically justified since in the actual caster, the feasible range of the cooling water flow rates is bounded due to the physical limitation of the spray cooling system, so the possible flux at the surface is bounded as well, and also piecewise continuous.

Assumptions (A1) and (A2) admit application of the maximum principle [35] (Theorem 8 on p.389), that a parabolic PDE solution attains its maximum value on the boundaries of its spatial and temporal domain, yielding

$$T < T_f, x \in (0, s), \text{ and } T = T_f, x \in (s, L) \forall t. \tag{2.30}$$

The existence and uniqueness of solution to the Stefan problem under (A1) and (A2) is discussed in [12], [36].

2.3.1.2 Eulerian coordinates

By using the generalized time derivative transfer equation (2.15), the 2D Eulerian model equivalent to the 1D Lagrangian model (2.24)-(2.27) is as follows:

$$T_t(x,z,t) + v_c(t)T_z(x,z,t) = aT_{xx}(x,z,t), x \in (0, s(z,t)) \cup (s(z,t), L), z \in \left[0, \infty\right), \tag{2.31}$$

$$s_t(z,t) + v_c(t)s_z(z,t) = b(T_x(x, s^-(z,t), t) - T_x(x, s^+(z,t), t)). \tag{2.32}$$

The initial conditions are

$$T(x,z,0) = \begin{Bmatrix} T_0(x,z), & x < s_0(z), \\ T_f, & x \geq s_0(z). \end{Bmatrix}, \tag{2.33}$$

$$s(z,0) = s_0(z). \tag{2.34}$$

The boundary conditions are

$$T(x,0,t)=\begin{Bmatrix} T_{pour}(x,t), & x<s(0,t),\, t>0, \\ T_f, & x\geq s(0,t),\, t>0, \end{Bmatrix}, \tag{2.35}$$

$$T_x(0,z,t)=u(z,t), \tag{2.36}$$

$$T_x(L,z,t)=0. \tag{2.37}$$

2.3.2 Existence and uniqueness of solution

This section provides the proof of the existence and uniqueness of solution to the Stefan problem (2.24)-(2.27) under the assumptions (A1) and (A2).

Lemma 2.1. The solution $T(x,t)$ of problem (2.24)-(2.27) under the assumptions (A1) and (A2) satisfies:

$$0\leq T_x\left(s^{-}(t),t\right)\leq M, \tag{2.38}$$

where $M=\max\{\ \max_{t,x}\{u(t),\frac{T_f-T_0(x)}{s_0-x}\}\}$.

Proof. Let us prove (2.38) for each fixed instant t^*. First, note that, the first inequality in (2.38) easily follows from the maximum principle. For each t^*, consider the function:

$$w(x,t)=M\left(s\left(t^*\right)-x\right)+T\left(x,t\right)-T_f. \tag{2.39}$$

For $0<t\leq t^*$, $0<x<s(t)$. Then,

$$w_{xx}=w_t, \tag{2.40}$$

$$w_x=-M+T_x\left(x,t\right)=-M+u\left(t\right)\leq 0, \tag{2.41}$$

$$w\left(s\left(t\right),t\right)=M\left(s\left(t^*\right)-s\left(t\right)\right)\geq 0, \tag{2.42}$$

$$w(x,0) = M\left(s\left(t^*\right) - x\right) + T_0(x) - T_f \geq 0. \tag{2.43}$$

Hence, by the maximum principle [35] (Theorem 8, p. 389), $w(x, t)$ >0 in its domain of definition. Since $w(s(t^*), t^*) = 0$, it follows that $w_x(s^-(t^*), t^*) \leq 0$ which implies $T_x(s^-(t^*), t^*) \leq M$ for each t^* and completes the proof of the Lemma. □

Theorem 2.1. (Existence) Under the assumptions (A1) and (A2) there exists a solution to the problem (2.24)-(2.27) which is defined for all t >0.

Proof. For each θ sufficiently small, define:

$$T_0^\theta = \begin{cases} T_0, & 0 \leq x \leq s_0 - \theta \ , \\ T_f, & s_0 - \theta < x \leq s_0. \end{cases} \tag{2.44}$$

Consider the time interval $0 \leq t \leq \theta$ and let $\left(T^\theta s^\theta\right)$ be the solution of problem (2.24)-(2.27) with T_0 replaced by T_0^θ, and $s(t)$ replaced by $s^\theta(t) \equiv s_0$. It is shown in [36] that, problem (2.24) -(2.27) has a unique solution $T^\theta(xt)$ for a given real-value function $s^\theta(t) \equiv s_0$. In this case it is easy to show that $T_x^\theta\left(s^{\theta-}(t), t\right) \equiv T_x^\theta(s_0^-(t), t)$ exists and is continuous in $[0, \theta]$ and by Lemma 2.1 we have $0 \leq T_x^\theta\left(s^{\theta-}(t), t\right) \leq M$. In the second time interval $\theta \leq t \leq 2\theta$, by retarding the argument in the boundary condition (2.27) we obtain:

$$s^\theta(t) = s_0 + \int_\theta^t T_x^\theta\left(s^\theta\left(\tau - \theta\right), \tau - \theta\right) d\tau. \tag{2.45}$$

Next we obtain $T^\theta(xt)$ for $\theta \leq t \leq 2\theta$ by solving (2.24)-(2.27) with new initial condition $T^\theta(x\theta)$ at $t = \theta$, and boundary s given by $s^\theta(t)$ for $\theta \leq t \leq 2\theta$.

Then, (2.45) can be used to define s^θ for $2\theta \leq t \leq 3\theta$. By induction, $\left(T^\theta s^\theta\right)$ can be defined for $0 \leq t \leq n\theta$.

Then, following the proof technique of existence of solution to the two-phase Stefan problem given in Theorem 1 in [37], there exists solution of (2.24)-(2.27) for $0 \le t \le t_\delta$, where

$$t_\delta = \inf\{t^* \mid t^* > 0, s(t^*) = \delta\}, \delta > 0. \tag{2.46}$$

Setting

$$t_0 = \sup_{0 \le \delta \le s_0} t_\delta. \tag{2.47}$$

The result in Theorem 2.1 follows. □

Lemma 2.2 (Theorem 2 of [37]). Let $(T_i, s_i), i = 1,2$ denote the solutions to the Stefan problem (2.24)-(2.27) for the respective boundary and initial conditions $T_0^i, s_0^i, u_i, i = 1,2$. Suppose $s_0^1 \le q s_0^2$, then there exists a constant C such that:

$$\left|s_1(t) - s_2(t)\right| \le C\left(\left|s_0^1 - s_0^2\right| + \int_0^{s_0^1} \left|T_0^1(x) - T_0^2(x)\right| dx + \int_{s_0^1}^{s_0^2} \left|T_0^2(x)\right| dx + \int_0^t \left|u_1(\tau) - u_2(\tau)\right| d\tau \right)$$

(2.48)

Proof. Please refer to [37] for a detailed proof. □

Theorem 2.2 (Uniqueness) Under assumptions (A1) and (A2) the solution to the problem (2.24)-(2.27) is unique.

Proof. This is an immediate corollary of Lemma 2.2 and maximum principle [35] (Theorem 8, p. 389). □

2.3.3 Enthalpy formulation

2.3.3.1 Lagrangian coordinates

Another PDE that can also be used to model the 1D slice of steel, which is also the actual equation used in [3], [4], is a generalized form of the conservation of energy. Enthalpy, $h(T)$, the thermodynamic internal energy of the material is defined in (2.2). Conservation of energy for heat diffusion can be written as:

$$\left(\rho h\left(T\left(x,t\right)\right)\right)_t = kT_{xx}\left(x,t\right), \quad x \in \left(0,L\right), \tag{2.49}$$

The boundary conditions remain the same as in (2.25), and the assumptions (A1) and (A2) can be similarly stated to ensure the problem is physically realistic.

It can be shown [38] that (2.49) with (2.2) and (2.24) with (2.27) under (A1) are actually equivalent in a weak sense. Since (2.49) involves taking the derivative of a step function, it will not have a solution in the classical sense. This makes the equation more difficult to analyze mathematically. However, since it does not explicitly require a moving boundary at s, it may be numerically modeled on a fixed computational domain, with (2.2) slightly regularized as (2.3).

2.3.3.2 Eulerian coordinates

The PDEs in Eulerian coordinates for the enthalpy formulation will be similar to (2.1),

$$(\rho h(T(x,z,t)))_t + \rho v_c (h(T(x,z,t)))_z = kT_{xx}, x \in (0,L), \tag{2.50}$$

with the same initial conditions as (2.33) and (2.34) and the same boundary conditions as (2.35)-(2.37).

CHAPTER 3.

MATHEMATICAL FORMULATION

3.1 Heat Transfer Model: CON1D

CON1D is a simple but comprehensive model of heat transfer and solidification of continuous casting of steel slabs. A brief overview of the model will be given in this section, but the reader may refer to [3] for more details.

The CON1D model includes phenomena in both the mold and the secondary spray cooling region. The simulation domain is a transverse slice through the strand thickness. CON1D computes the entire temperature distribution within the solidifying slice from the meniscus to the end of the containment. The CON1D model takes the Lagrangian reference frame and simulates a 1-D transverse slice through the thickness, which moves with the steel. The governing equation within the simulation domain is,

$$\rho c_p^* \frac{\partial T}{\partial t} = k \frac{\partial^2 T}{\partial x^2} + \frac{\partial k}{\partial T}\left(\frac{\partial T}{\partial x}\right)^2, \tag{3.1}$$

where $T(x,t)$ is the temperature distribution along the strand thickness at time t. The density ρ, the thermal conductivity k, and the effective specific heat c_p^* are the properties of the cast material. The effective specific heat includes the latent heat, as defined in (2.3).

The solution method CON1D uses is an explicit central finite difference method with a post-step correction to maintain an accurate balance on the latent heat [3]. CON1D is capable of considering complex boundary conditions in the mold and the secondary cooling region. Heat flux in the mold depends on many complicated phenomena. In this thesis, CON1D takes the measured

average mold heat flux – typically from the measurement of the temperature change of the mold cooling water – and fits it to a simplified local heat flux profile down the mold that has been calibrated to match measurements at previous casters [3].

The boundary conditions in the secondary cooling region must be considered in detail, since they profoundly influence the product quality and process safety. In CON1D, the heat transfer in the secondary cooling region is simplified to the following four main mechanisms: spray water cooling (h_{spray}), radiation (h_{radspray}), air convection (h_{conv}) and conduction to the supporting rolls (h_{roll}), as shown in Figure 9 [3].

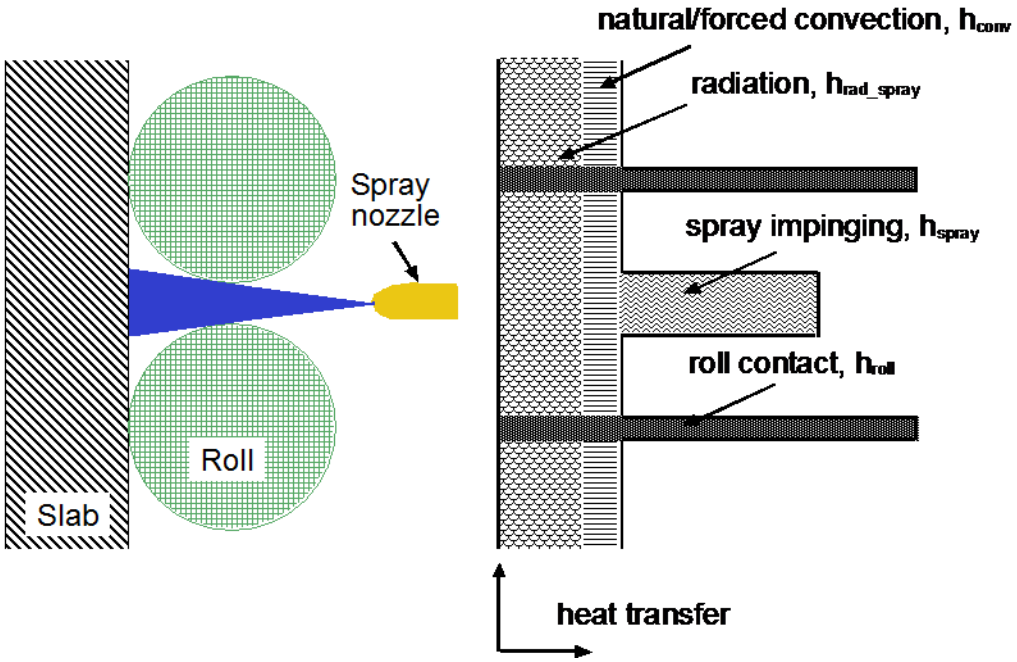

Figure 9. Schematic of the spray cooling region [3].

The heat extraction due to the spray cooling water is approximated by a function of the water flow rate of the following form [3]:

$$h_{spray} = A \times Q_{water}^{c} \times \left(1 - b \times T_{spray}\right), \tag{3.2}$$

where, Q_{water} is the local spray water flux (flow rate through the unit surface area) hitting the strand surface at time t, which is the primary method of temperature control in a continuous caster.

The term T_{spray} is the temperature of the spray water, which is easily measured. The constants A and c are the only fitting parameters in the paper. In general, they vary along the caster and depend on the design of the caster and the cooling sprays, as well as the steel grade being cast and the casting conditions. These parameters are unknown a priori and are determined by calibrating dynamic model simulations through experimental plant data and/or separate tests on a dedicated rig.

Radiation is calculated by:

$$h_{rad-spray} = \delta \times \varepsilon_{steel} \left(T_{sK} \times T_{ambK}\right)\left(T_{sK}^2 \times T_{ambK}^2\right), \tag{3.3}$$

where T_{amb} is the ambient temperature, T_s is the strand surface temperature, and T_{sK} and T_{ambK} are T_s and T_{amb} expressed in Kelvin, $\delta$is the Stefan-Boltzmann constant ($5.67\times10^{-8} W/m^2K^4$), and ε_{steel} is the emissivity of the strand surface (0.8). Because of the water cooling only, the air convection, h_{conv}, is not very important and is treated as a constant ($8.7 W/m^2K$).

The heat extraction into rolls is calculated based on the fraction of the total heat extraction to rolls, f_{roll}, which is calibrated as follow for each spray zone:

$$\begin{aligned} h_{roll} = \frac{f_{roll}}{L_{rollcontact}\left(1-f_{roll}\right)}\Big(&\left(h_{rad-spray} + h_{conv} + h_{spray}\right)L_{spray}n \\ &+\left(h_{rad-spary} + h_{conv}\right)\left(L_{spraypitch} - L_{spray} - L_{rollcontact}\right)\Big). \end{aligned} \tag{3.4}$$

A typical f_{roll} value of 0.05 produces local temperature drops beneath the rolls of about 100^oC [3]. Increasing f_{roll} will increase the heat extracted into the rolls and will result in more local temperature drop under the rolls. Beyond the spray cooling region, heat transfer simplifies to radiation and natural convection.

3.2 Software Sensor: CONSENSOR

CONSENSOR is designed to produce the temperature profile along the entire caster (z) and through its thickness (x) in real-time, by exploiting CON1D as a subroutine. It does this by managing the simulation of N different CON1D slices, each starting atthe meniscus at different times to achieve a fixed z-direction spacing between the slices. The model (50) can be solved by CON1D faster than real-time, but it only gives the temperature estimation at the locations of the moving reference frame, which in return depends on the casting speed history. By repeating the calculation for multiple slices simultaneously, CONSENSOR aggregates the temperature and the shell thickness profiles from the moving 1-D Lagrangian models into the stationary 2-D Eulerian frames.

Figure 10 shows an illustrative example with $N = 10$. CONSENSOR updates the temperature estimate $\hat{T}(x, z, t)$ every Δt seconds. During each time interval, CONSENSOR tracks the temperature and the shell thickness evolution in each slice over this interval, given the previously calculated and stored temperature distributions across the thickness of that slice at the start of the interval:

$$\hat{T}\left(x, z_i\left(t\right), t\right) = T_i\left(x, t\right), \tag{3.5}$$

where,

$$z_i\left(t\right) = \int_{t_i^0}^{t} v_{\mathrm{c}}\, \mathrm{d}t. \tag{3.6}$$

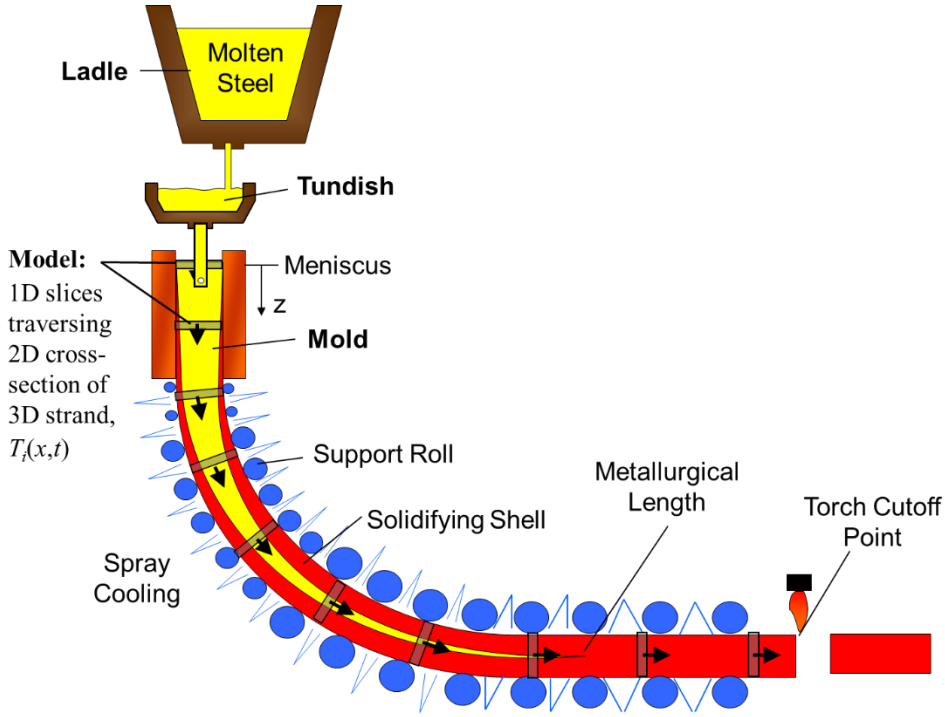

Figure 10. Illustration of the 2D Eulerian model aggregating multiple 1D Lagrangian moving slices.

The computer used to run CONSENSOR (quad-core 3.0 GHz processor) can currently handle up to 200 of these slices simultaneously while still running in real-time. In the 30 *m* long thick-slab caster discussed below, with slices evenly spaced, this yields a spacing of $30/200 = 0.15m$ between slices, which is roughly half the roll pitch. In order to get temperature estimation $\hat{T}(x,z,t)$ for locations between the slices, $z_{i-1} < z < z_i$, CONSENSOR uses "delay interpolation", substituting the most recent "exact estimate" of the temperature at that location, i.e., the temperature of the most recent slice to pass through that location. Mathematically, this means

$$\hat{T}\left(x, z_i(t), t\right) = T_i\left(x, t_i(z)\right), \tag{3.7}$$

where $t_i(z)$ can be found by solving for the inverse of (55), i.e.,

$$z = z_i\left(t_i(z)\right) = \int_{t_i^0}^{t_i(z)} v_c \, dt. \tag{3.8}$$

In practice, though, CONSENSOR stores the entire temperature history of each slice and searches through them to find the most recent temperature, rather than solving (3.8). Figure 11 illustrates the "delay interpolation" procedure with only two slices and constant casting speed v_c. In this case, we are trying to estimate the temperature at a specific time t^* and distance from the meniscus z^*. Slice 1 originated at the meniscus at time t_1^0, so at time t^* it is located at the position $z_1(t^*) = v_c(t^* - t_1^0)$. Similarly, slice 2 is at the position $z_2(t^*) = v_c(t^* - t_2^0)$. This means that we have the exact temperature estimates at these two locations. To estimate the temperature at a point between the two, i.e. at $z_1(t^*) < z^* < z_2(t^*)$, we look backward in time for the most recent exact estimate at that location. In this case, as the figure shows, it comes from when slice 1 was at that location. When the casting speed is constant, (3.8) can be solved directly to get

$$\hat{T}\left(x, z^*, t^*\right) = T_1\left(x, t = t_1^0 + z^* / v_c\right). \tag{3.9}$$

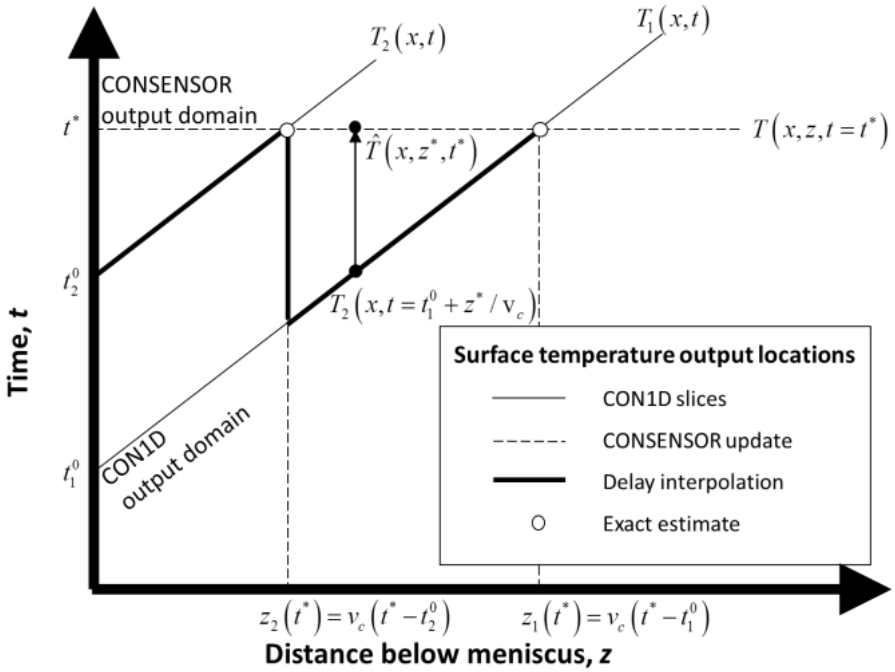

Figure 11. Illustration of the delay interpolation method, with two slices and the constant casting speed [4].

The “delay interpolation method" can be thought of as a version of the “sample and hold" interpolation method in the conversion of discrete measurements to analog signals, which assumes that the values of the data between the samples are constant at the most recent measurements. In the case of CONOFFLINE, the slice prediction is the "measurement" and the CONOFFLINE output at any point in the caster updates when a slice passes and is constant otherwise.

The approximation error introduced to location z^* in Figure 11 is the temperature change from $t1(z^*)$ to $t^* + \Delta t$, which is a function of the extent of transient effects in the laboratory frame and slice spacing [4] . This error will be most substantial when the casting speed is low, increasing the residence time of the slices in the caster, or when the casting conditions change drastically in a small amount of time. Figure 12 shows this error under the worst-case scenario, a sudden drastic casting speed drop. In the figure, slices 1, 2, and 3 were the consecutively created ones. Slices 2 and 3 are at the locations $z_2(t)$ and $z_3(t)$, respectively, at the time when the data is collected. Through the “delay interpolation method" [4] , CONOFFLINE takes the temperature and the shell thickness from the history of slice 3 before z_3, the history of slice 2 between z_2 and z_3, and the history of slice 1 after z_2. Due to the drastic speed drop, slice 3 is much colder than slice 2, which is much colder than slice 1. This leads to the jumps in the temperature and the shell thickness at the points where CONSENSOR switches from an older slice to a newer one.

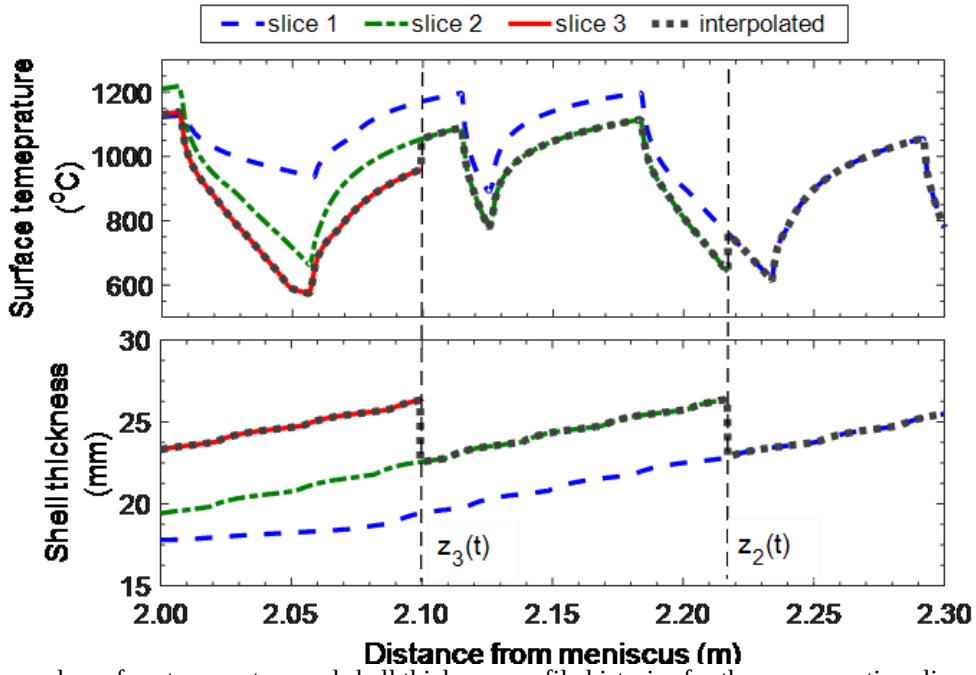

Figure 12. Example surface temperature and shell thickness profile histories for three consecutive slices, and delay-interpolated profiles from CONSENSOR.

Remark 1. The approximation error decreases as the number of slices, N, increases. When $N \rightarrow \infty$, the model will be the same as the 2-D Eulerian PDE (30) with slightly mollified $h^*(T)$ that has a derivative of effective specific heat, c_p^*, as in (3).

3.3 Industrial Control System: CONONLINE/CONOFFLINE

CONONLINE, developed by Petrus et al [4], is a real-time control system consisting of several programs running at the same time. The various programs communicate through 'shared memory', which is a block of memory that is accessible by any program and is updated every second. Figure 13 shows the schematic diagram of CONONLINE. Two major programs of CONONLINE are CONSENSOR and CONCONTROLLER. CONSENSOR, the "software sensor", takes the caster data as input and uses the CON1D subroutine to predict the temperature profile and the shell thickness profile through the strand thickness for the entire caster in real time.

Then CONCONTROLLER reads the temperature distribution and computes the spray water flow rates needed for each spray zone to maintain the surface temperature. The control algorithm used by CONCONTROLLER is a simple PI controller with the classic anti-windup.

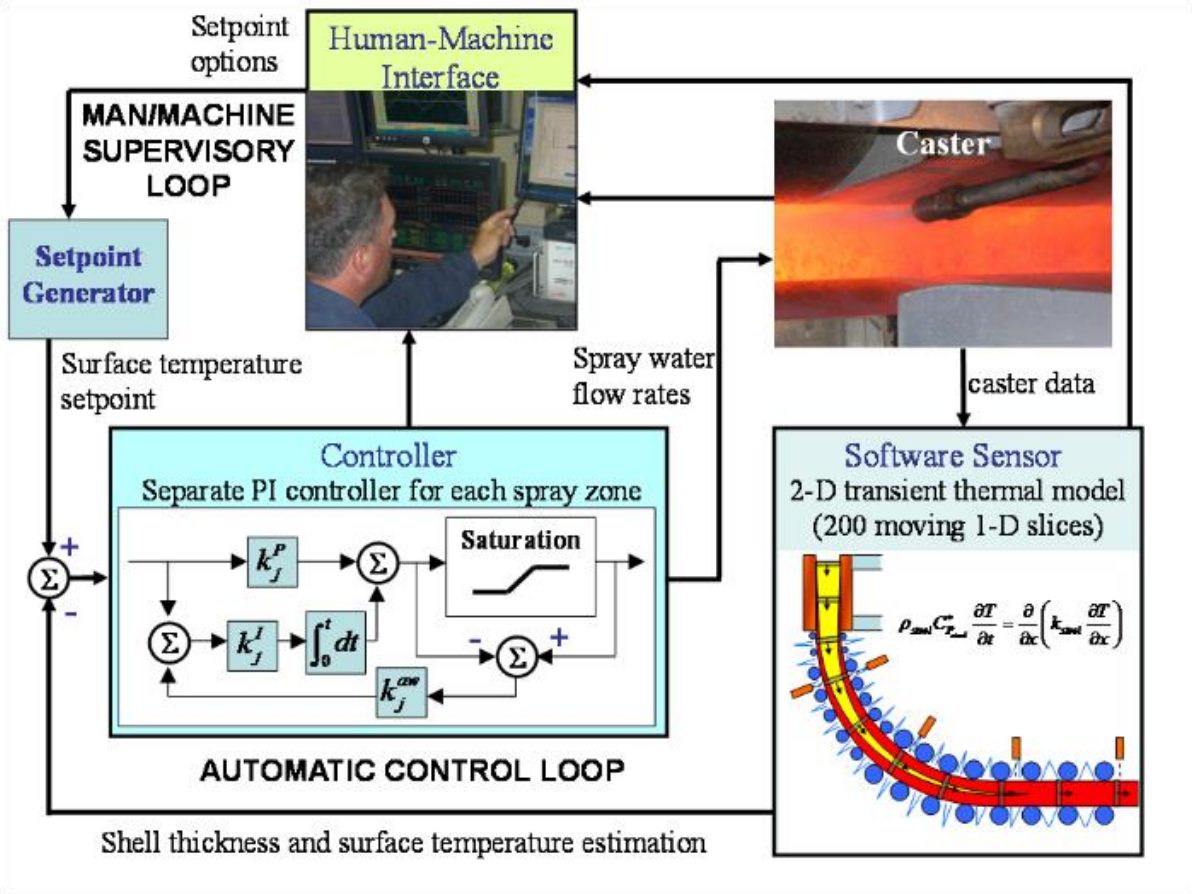

Figure 13. Structure of the software sensor-based control diagram–CONONLINE [4].

CONOFFLINE, as shown in Figure 14, is an offline version of CONONLINE that has been extensively used to study different transient behaviors of continuous casting [12], [39]. For CONOFFLINE, instead of getting the real caster data, CONSENSOR uses the recorded or the specified casting conditions. Also, instead of the PI controllers (CONCONTROLLER), other control methods are applied as well.

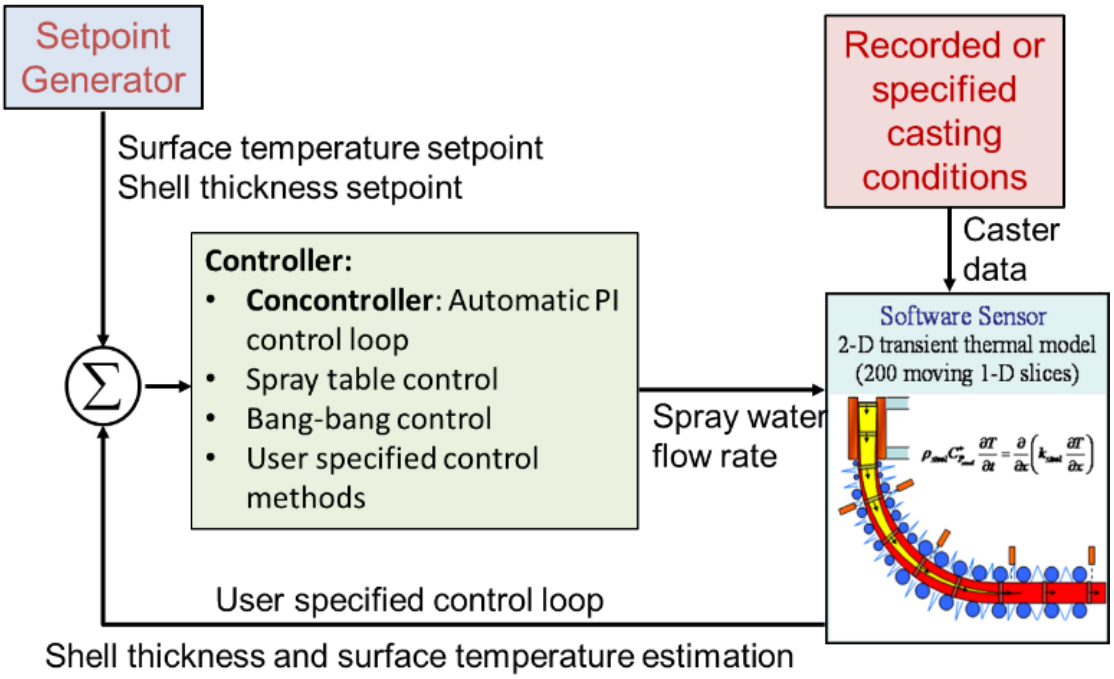

Figure 14. Structure of CONOFFLINE.

3.4 Model Validation

To investigate the transient change in metallurgical length during the casting speed changes, CONOFFLINE was applied to the ArcelorMittal $260mm$ thick slab caster at the Burns Harbor CC1 caster where measurements during transient conditions were made during trials to redesign the roll gap [33]. Strain gauges were installed on some of the supporting rolls to measure the changing forces exerted on those rolls by the strand [33] .

3.4.1 Thermal shrinkage model

The strand thickness, L, is estimated from the 2D thermal history solution described above by applying a thermal shrinkage model. As shown in Figure 15, ferrostatic pressure in the liquid tends to deform the strand outward at all locations where the shell has not yet fully solidified. In these locations down the caster, the width of the strand matches the roll gap. Elsewhere, after the strand is fully solid, the steel shrinks according to its temperature and natural thermal contraction. To

predict the average shrinkage of the strand thickness, as a post-processing step, the thermal linear expansion (TLE) function based on the previous measurements [40]–[42] is used. For a material of length L, the TLE is the relative change in thickness from the strand thickness at the reference temperature, T_{ref}, where TLE is chosen to be 0:

$$TLE(T) = \frac{\Delta L(T)}{L(T_{\text{ref}})} = \frac{L(T) - L(T_{\text{ref}})}{L(T_{\text{ref}})}. \tag{3.10}$$

TLE is calculated from the weighted average of the density of the individual phases, $\rho(T)$, as follows:

$$TLE(T) = \sqrt[3]{\frac{\rho_{\text{ref}}}{\rho(T)}} - 1. \tag{3.11}$$

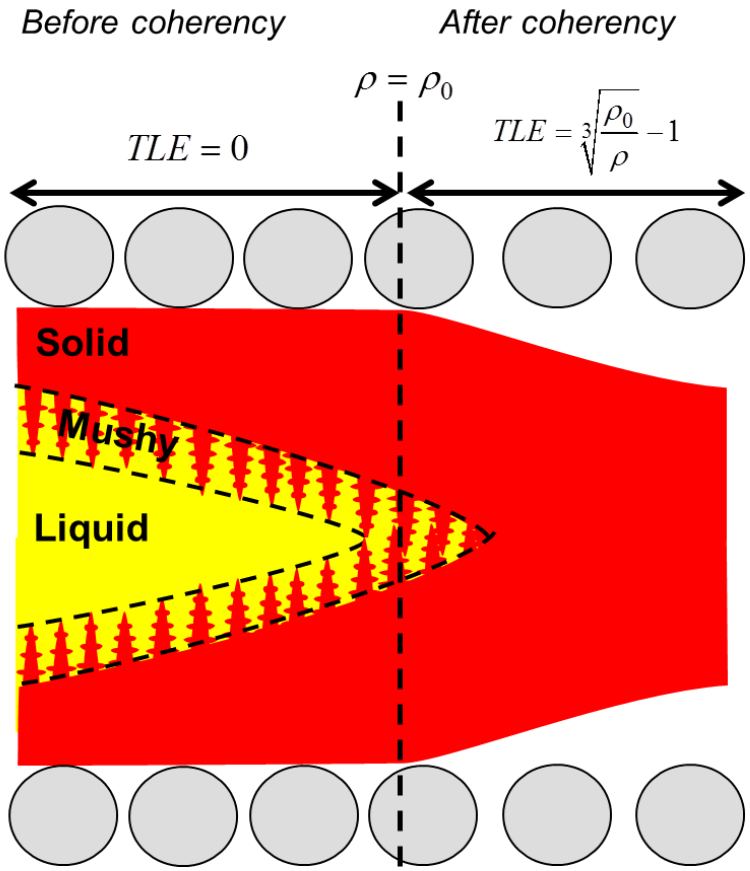

Figure 15. Illustration of the simple thermal shrinkage prediction method used in CONOFFLINE.

The functions [3] used to calculate the thermal properties for a low-carbon (0.05 wt-%C) steel are given in Figure 16, in which the reference temperature is chosen to be the liquidus temperature. The following fast and simple methodology to estimate strand shrinkage is implemented into CONOFFLINE as follows:

1. Calculate the temperature, $T(x,z)$, and the phase fractions, $f_s(x,z)$, everywhere in the strand.

2. Using the density models [42], the average nominal density over the cross-section, $\rho(z)$, is calculated as a function of the temperatures, the phase fractions, and the steel composition.

$$\rho(z) = \frac{1}{L}\int_0^L \rho\big(T(x,z)\big)\,dx. \tag{3.12}$$

3. Assuming the material is coherent (the dendrites form a rigid solid network that cannot move) for a solid fraction $f_s \geq f_{s,cohere}$ ($f_{s,cohere}$ is a user-defined variable), find the point of coherency. i.e., position z_{cohere} such that $f_s(x,z) \geq f_{s,coherent}$ for$z \geq z_{cohere}$. For $z < z_{cohere}$, the ferrostatic pressure pushes the strand out to the containment rolls. After z_{cohere}, normal thermal shrinkage applies. Hence, the density at z_{cohere} is used as the reference density for the shrinkage calculation.

4. Calculate the thermal linear expansion $TLE(z)$,

$$TLE(z) = \begin{cases} 0, z < z_{cohere}, \\ \sqrt[3]{\dfrac{\rho(z_{cohere})}{\rho(z)}} - 1, z \geq z_{cohere}. \end{cases} \tag{3.13}$$

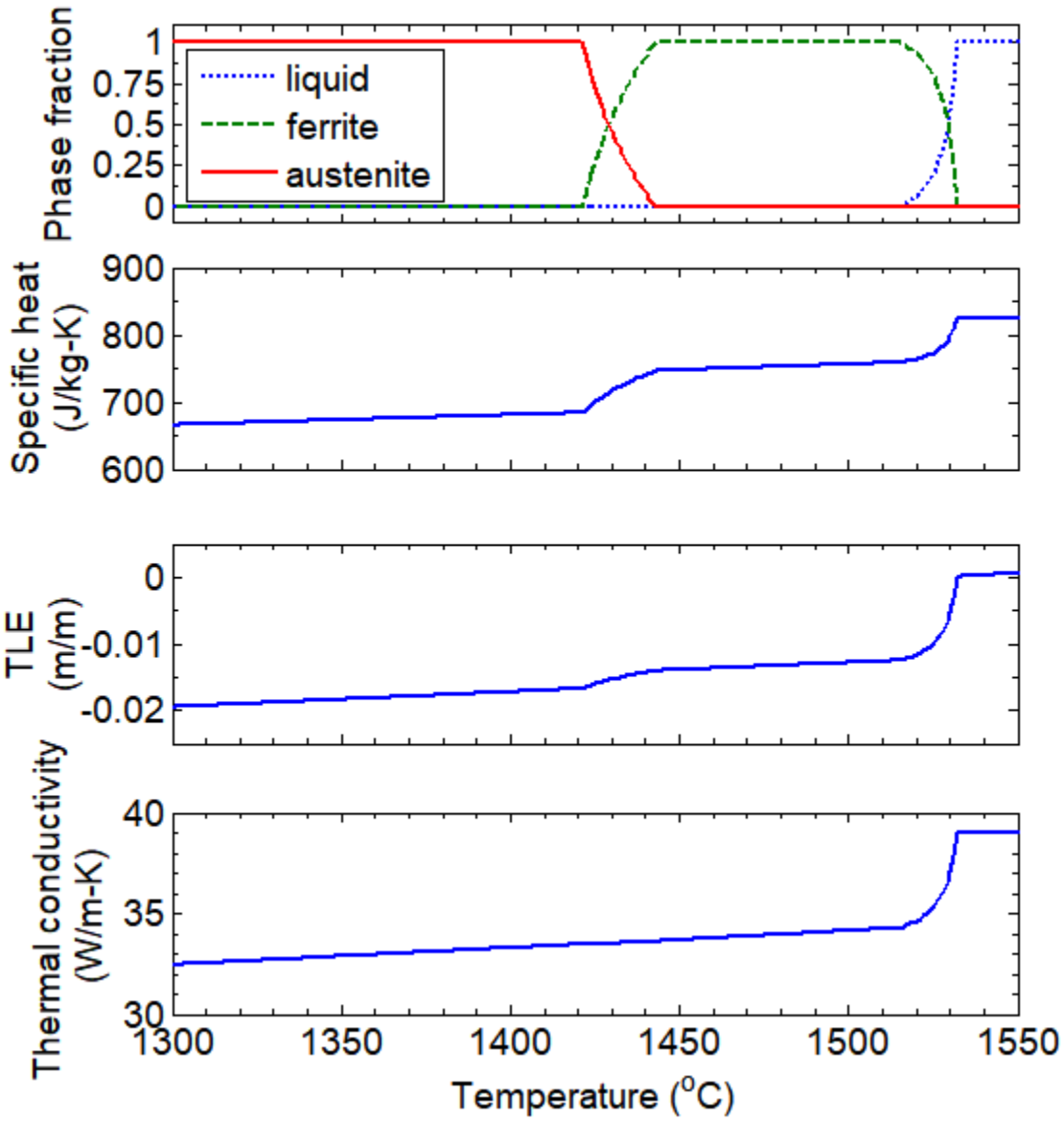

Figure 16. Properties of 0.05 wt-% Carbon steel **[3]**.

3.4.2 Casting conditions

Most of the casting conditions for the chosen trial of the speed-drop and the speed-up, including the caster geometry, the roll pitch profiles, and the casting speed histories, were taken from the reference [33]. Properties and pour temperature for a typical low-carbon steel grade (0.05 wt–%C assumed), are given in Table 1 and Figure 16. The assumed roll gap profile was taken from measurements prior to casting when the machine was cold, although the authors note that the gap

expanded when steel was in the caster. The boundary heat fluxes in the mold and the spray zones were estimated from the previous experience, as described below, and then calibrated to match the reported metallurgical lengths at a steady state. These steady-state boundary conditions were then interpolated or extrapolated, as explained below, to determine conditions for the dynamic case.

Table 1. Steel properties in simulation

Steel Property	Value
Liquidus temperature	1532.1 ^oC
Solidus temperature	1515.3 ^oC
Pour temperature	1550 ^oC
Latent heat	271 kJ/kg

For simplicity, the boundary heat flux is assumed to be the same on either side of the strand. In the mold, the average heat flux was based on an empirical correlation with the casting speed for a thin slab caster [43], as follows:

$$\bar{q}_{\mathrm{m}}\left[\mathrm{MW/m^2}\right] = 0.9535\left(v_c\left[\mathrm{m/min}\right]\right)^{0.5}. \tag{3.14}$$

The exponent is chosen to be 0.5, the theoretical value for the constant surface temperature in the mold [44], and close to that reported in the references [43], [45], and the coefficient was chosen to match the reported metallurgical lengths, $28m$ at a casting speed of 1.1 m/min and $23m$ at a casting speed of 0.9 m/min [33]. This average mold heat flux was converted into a heat flux profile as described elsewhere [4].

In the secondary cooling, the heat flux was assumed to depend on the water flux impacting the steel surface, according to relations given in the previous work [3], [4], [39], [46]. The water flow flux was assumed to vary linearly with the casting speed according to

$$Q_{\mathrm{sw}}\left[\mathrm{L/m^2/min}\right] = -160 + 600 v_{\mathrm{c}}\left[\mathrm{m/min}\right]. \tag{3.15}$$

All sprays were assumed to cover the length of 30 mm in the z direction, and the slope and the intercept were again chosen to match the reported metallurgical lengths at the steady casting speeds of 1.1 m/min and 0.9 m/min. These two speeds roughly approximate the 0.762 to 1.143 m/min speed range of the dynamic trial. These assumptions become increasingly unrealistic for the speeds outside of the calibrated range, and the variations caused by the separate heat extraction to the rolls and by different nozzle configurations in different spray zones are ignored. Therefore, the model-predicted surface temperatures are not expected to be accurate. However, because the metallurgical lengths were calibrated to be accurate, the overall heat flux profiles are expected to be reasonable, so the model predictions of the shell thickness and the internal temperature are expected to roughly match those at the plant.

More importantly, the dynamic behavior incorporated into the model through the 2-D transient heat conduction equation is expected to be accurate. Furthermore, this test case also serves as a validation of the solution approximation method of a series of 1D slices via (3.1).

3.4.3 Steady-state simulation results

As mentioned above, model calibration was performed by choosing the mold heat removal and the secondary cooling water spray rates to match the reported metallurgical lengths in the plant trial [33]. Figure 17 and Figure 18 display some of the simulation results at a steady casting speed of 1.1 m/min, which had a metallurgical length of 28 m. Figure 17 shows the temperature profiles through the thickness at four locations down the caster. In this figure, 0 mm on the x-axis is the inner radius surface and 259 mm is the outer radius surface. Figure 18 shows the corresponding results down the length of the entire caster from the meniscus to the last containment roll.

The middle graph in Figure 18 illustrates that final solidification actually occurs over a range, specifically from 25.4 m to 28.2 m. Steel, being an alloy, solidifies over the temperature range from liquidus to solidus. In this range, the centerline consists of dendrites and inter-dendritic liquid, which is often called the "mushy zone." Although different definitions are possible, the "metallurgical length" of primary interest in this work is when the dendrites growing from opposite sides of the strand weld together sufficiently to provide enough coherency to prevent the ferrostatic force from the liquid pool from pushing the strand against the containment rolls, leading to a drop in the roll force. In the previous work [3], [47], a solid fraction of 0.7 was found to match reasonably well with predicting this metallurgical length, which in this case gives 27.8 m, as shown in Figure 18.

The bottom graph in Figure 17 illustrates that a large amount of thermal shrinkage occurs near the metallurgical length, when the molten steel solidifies from liquid to delta-ferrite. Even more shrinkage occurs just after the strand becomes fully solid. This is also seen at the end of the bottom graph in Figure 18. This is due to the faster cooling that is possible when there is no more liquid to supply latent heat. Of course, the extent of the shrinkage also depends on the steel grade, which affects the shrinkage from delta-ferrite to austenite, and on the spray cooling conditions.

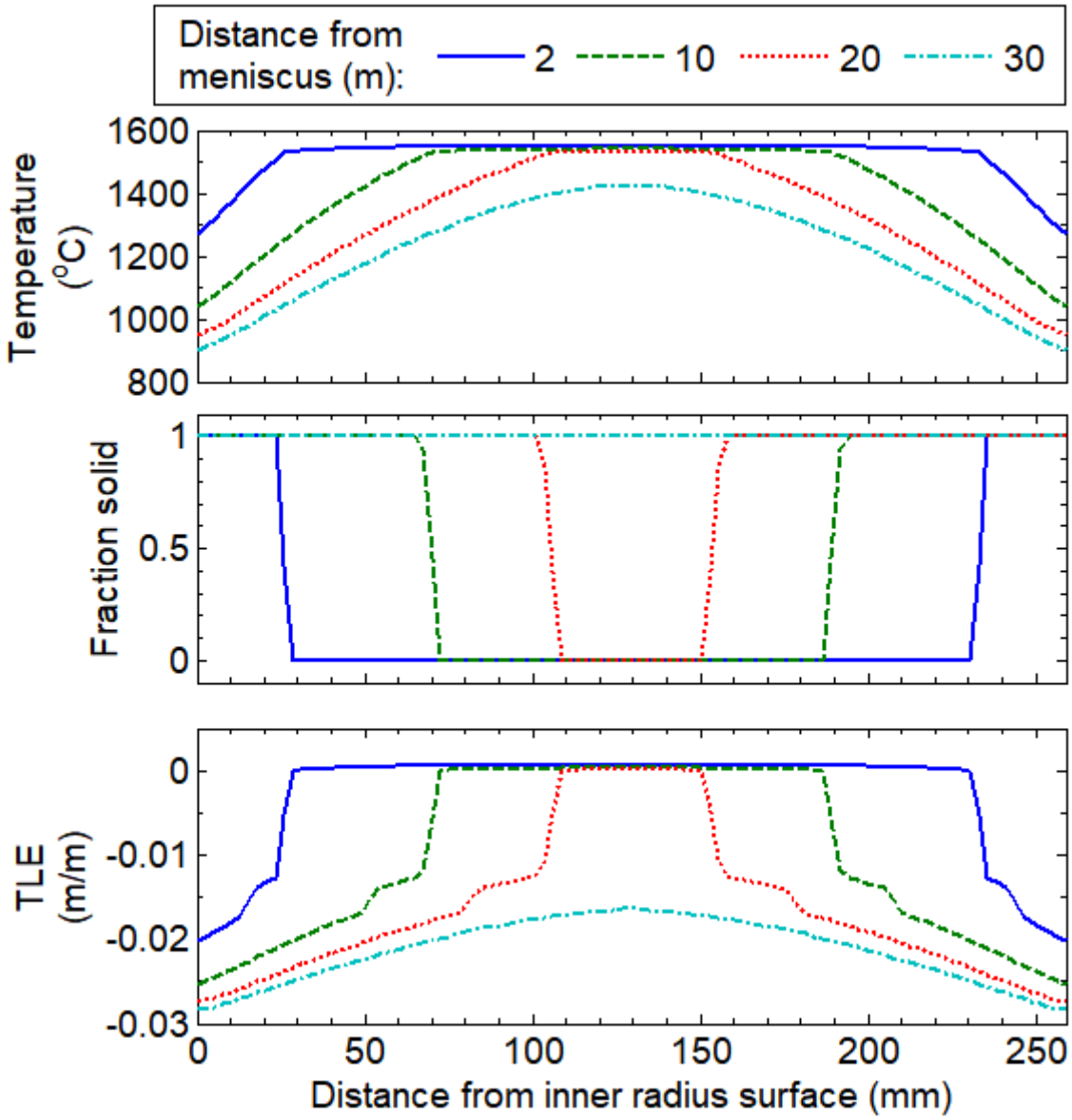

Figure 17. Th steady-state temperature, the solid fraction, and the TLE profiles through a transverse slice of the strand at different times / distances down the caster.

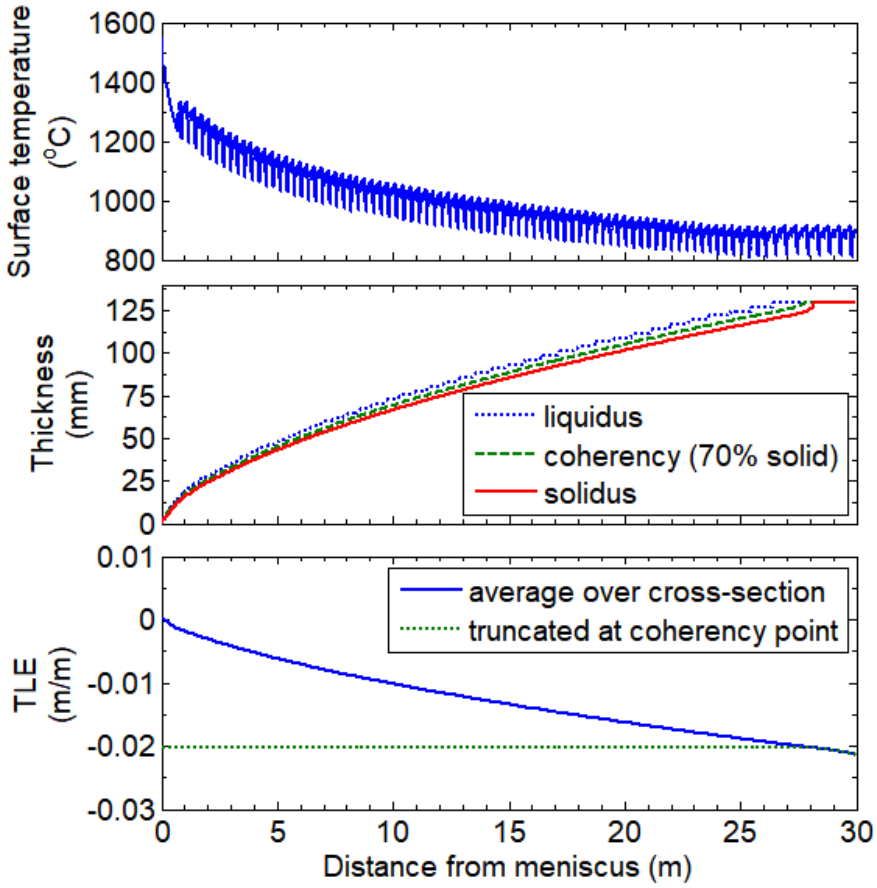

Figure 18. The steady-state surface temperature, the shell thickness, and average TLE profiles down the caster.

The plant trial [33] reports the improved slab centerline quality when the machine taper is set at 0.34 *mm*/*m*. It is well known that the centerline quality is the best when the machine taper approximately matches the natural shrinkage of the steel during the final solidification, which provides a possibility for the quantitative comparison with the model TLE prediction. Prior to the final solidification, the predicted TLE (solid blue line) contrasts with the dotted green line inFigure 18, which represents the strand thickness without consideration of the machine taper. This is illustrated qualitatively in Figure 15. Both of the predicted TLE lines then shrink from -0.02013 *m*/*m* when coherency is reached (27.77 *m*) to -0.02138 *mm*/*m* at the end of the caster (30 *m*), Converting these numbers to an average slope, the predicted ideal machine taper in the critical range near the final solidification is 0.145 *mm*/*m*. This is less than the reported machine taper by more than a factor of 2.

However, the TLE equation (3.11) assumes isotropic behavior, so there is equal thermal shrinkage in all directions. In the continuous casting strand, the results from a thermal-mechanical model [48] have shown that the strand shrinks more in the thickness direction because the axial (casting) and the width directions are more strongly constrained. This shows that the simple shrinkage prediction of this model behaves as expected and should produce a reasonable qualitative behavior.

3.4.4 Transient simulation results

Figure 19(a) and Figure 19(b) show the casting speed and the strain gauge measurements collected from the ArcelorMittal plant trial [33]. After a delay, the roll loads decrease when the casting speed decreases and increase when the casting speed increases. This change is related to the changing location of the liquid core. While there is still liquid beneath a given support roll, the ferrostatic pressure of the liquid pushes the shell against the roll, causing high roll load measurements. When the strand is solid beneath the support roll, there is no ferrostatic pressure and the measured loads are smaller, according to the shrinkage of the strand thickness. Thus, the shrinkage of the shell cross-section, predicted by CON1D from the simulated temperature and shell thickness distribution as described in the previous section, can be used as a relative indication of the roll force.

Figure 19(c)-Figure 19(e) show predictions of CONOFFLINE for the speed change in Figure 19(a). Comparing Figure 19(b) and Figure 19(c) shows good qualitative matches between the measured roll forces and the predicted TLE at the rolls. Furthermore, the results show matches of the timing of changes quantitatively. After the speed drop, the metallurgical length decreases, and the roll loads decrease as the metallurgical length passes the roll. Since roll 79 is further down in the caster from the meniscus and is closest to the metallurgical length before the speed drop, it is

the first roll to respond to change. Model results also predicted sequence time delay of the TLE at different rolls reacting to the speed drop, and the predicted times of change are very close to the measurements. The sequence change of roll loads after the speed up predicted by the model also matches the measurements. CONOFFLINE also correctly predicts sharp changes occurring after the strand is completely solid (that the changes are steeper while the caster is speeding up than when it is slowing down), and the undershoot and rebound that is present in the measurements.

An essential feature of the CONOFFLINE model, which ignores axial conduction and simulates independent 1-D slices, is that the transient behavior can last no longer than one "dwell time" of the caster, i.e. the time it takes for steel to travel from the meniscus to the caster exit. A previous model [49], which did include the effect of axial conduction, reported that transient effects after a slow down took longer to settle than after a speedup, and exceeded the dwell time, suggesting that axial conduction may be significant. These results reiterate that the timing of the measured transient response agrees with CONOFFLINE, meaning that the assumption of the axial heat transfer dominated by advection is validated.

For further examination, Figure 19(e) shows the surface temperatures at important locations in the strand during these transient conditions. For reference, segment 13 contains the four instrumented rolls where the load was measured and the TLE was predicted. The surface temperature first increases after the speed drop, as the "spray table" control drops the cooling water flow rate immediately after the speed drop that makes the strand surface temporarily hotter. After the initial increase, the surface temperature gradually decreases as the strand is moving slower, giving more time for the strand to cool down. Therefore, the overall strand is growing colder, as can be seen in the metallurgical length or the thermal shrinkage.

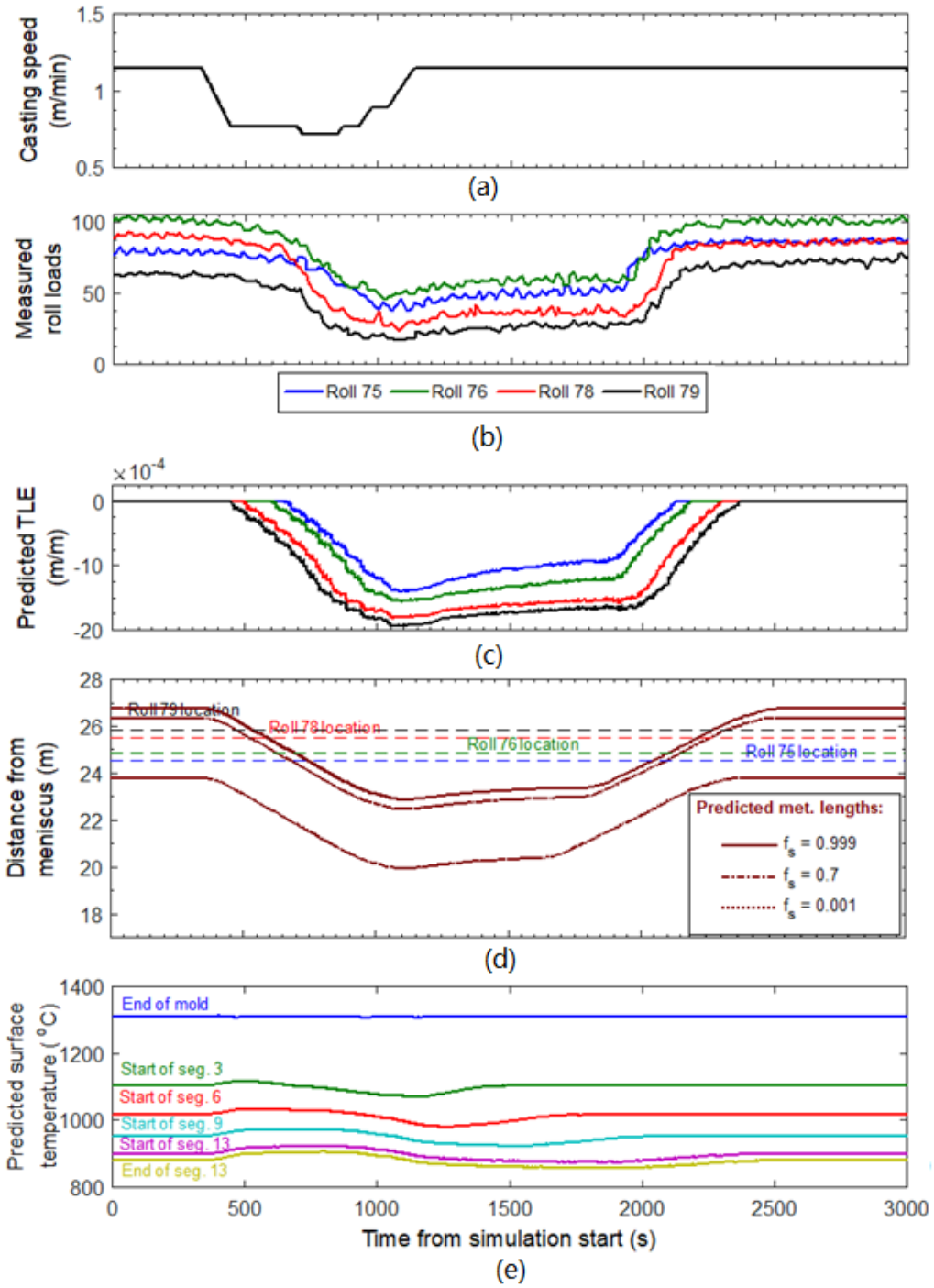

Figure 19. CONOFFLINE model predictions of dynamic temperature, solidification and thermal shrinkage compared with roll loads measured by strain gauges during a speed dip in AM caster.

CHAPTER 4.

OUTPUT FEEDBACK CONTROL

The current industry-standard control method is open-loop control that changes the water spray rates in response to the changes in the casting speed, but not to the grade, the mold heat removal rate, the initial temperature, or any other changing conditions. This open-loop control can be determined by experience, or through the use of offline optimization techniques such as [39], [50]. In [4], the authors developed a real-time control system consisting of a detailed computational model, CONSENSOR, to predict the temperature and the shell thickness of the strand, and applied PI controller to maintain the average temperature of each spray zone. However, this system primarily focuses on the process modeling, using a more detailed nonlinear PDE than the Stefan Problem, but applies a heuristic non-model-based control law.

In [13], the authors found a model-based enthalpy-based full-state feedback control law that ensured convergence of both the temperature and the solidification front to the desired reference profile for a simplified Stefan Problem. The paper also proposed an estimator, and presented simulation results of the output feedback controller, but no proofs were given. This chapter fills the gap by providing stability proofs. Sections 4.1 and 4.2 provides preliminaries, and Section 4.3 presents the stability proofs.

Section 4.3 is based on paper [51]. The goal is to develop recalibration techniques for the state estimators to overcome the discrete boundary sensing problem, as for the solidification processes like steel casting, measurements are only available at particular points in the caster. Each of these measurements corresponds to a single discrete-in-time boundary data point.

4.1 Reference Error System

Assume that the system motion to be tracked has been generated through the solution of the motion planning problem for system (2.24)-(2.27). This solution includes a known reference temperature $\bar{T}(x,t)$ and a solidification front position $\bar{s}(t)$, generated by the known reference control input $\bar{u}(t)$ with the initial conditions $\bar{T}(x,0) = \bar{T}_0$ and $\bar{s}(0) = \bar{s}_0$ satisfying assumptions (A1) and (A2). This reference temperature profile should satisfy the metallurgical objectives and the process constraints, and could, for example, be calculated for the continuous caster via the optimization methods of [52], [53] or the inverse methods of [21], [50], [54].That is, matching the reference temperature should result in a safe operation and good quality steel. One more assumption on the reference profile is made:

(A3) $\dot{\bar{s}}(t) \geq 0$ for all $t \geq 0$.

The reference system then takes the form

$$\bar{T}_t(x,t) = a\bar{T}_{xx}(x,t), \quad x \in \left(0, \bar{s}(t)\right) \cup \left(\bar{s}(t), L\right), \tag{4.1}$$

$$\bar{T}\left(\bar{s}(t),t\right) = T_f, \quad \bar{T}_x(0,t) = \bar{u}(t), \quad \bar{T}_x(L,t) = 0, \tag{4.2}$$

$$\bar{T}(x,0) = \bar{T}_0(x), \quad \bar{s}(0) = \bar{s}_0 \tag{4.3}$$

$$\dot{\bar{s}}(t) = b\left(\bar{T}_x\left(\bar{s}^-(t),t\right) - \bar{T}_x\left(\bar{s}^+(t),t\right)\right), \tag{4.4}$$

Denote the reference errors as $\tilde{T}(x,t) = T(x,t) - \bar{T}(x,t)$, and $\tilde{s}(t) = s(t) - \bar{s}(t)$. Also denote $\tilde{u}(t) = u(t) - \bar{u}(t)$. Subtracting the PDEs (4.1) from (2.24) and (4.2) from (2.25) yields,

$$\tilde{T}_t(x,t) = a\tilde{T}_{xx}(x,t), \quad x \in (0,L) - \{s, \bar{s}\}, \tag{4.5}$$

$$\tilde{T}_x(0,t) = \tilde{u}, \quad \tilde{T}_x(L,t) = 0. \tag{4.6}$$

Also, since solutions to (2.24) are twice spatially differentiable away from the solidification front, they must have continuous first spatial derivatives. Thus, if $\bar{s}(t) \neq s(t)$, then $\bar{T}_x(s^+(t), t) = \bar{T}_x(s^-(t), t)$, and so

$$\dot{s}(t) = b\left(\tilde{T}_x\left(s^-(t), t\right) - \tilde{T}_x\left(s^+(t), t\right)\right). \tag{4.7}$$

Similarly,

$$\dot{\bar{s}}(t) = -b\left(\tilde{T}_x\left(\bar{s}^-(t), t\right) - \tilde{T}_x\left(\bar{s}^+(t), t\right)\right). \tag{4.8}$$

From here on, simplified notation, $T(x)$ will be used to represent $T(x, t)$, or both arguments will be omitted altogether for brevity.

4.2 Preliminaries and Notation

If the solution (T, s) to the PDE (2.24)-(2.27) satisfies assumptions (A1) and (A2), a few facts immediately follow. First, $T(x) < T_f$ and is non-decreasing for all $0 \leq x < s(t)$, which in turn implies $\dot{s}(t) \geq 0$ for all $t \geq 0$. For the single-phase Stefan problem, $T_x \equiv 0$ when $s \leq x \leq L$. Since (2.24) is parabolic on the subdomains, if (A2) holds then T_x is uniformly bounded by a constant depending on the initial condition and bounds on u. (See, e.g., Theorem 11.1 from Section III.11, p. 211 of [55].) Due to (2.27), this means that the solidification front speed is bounded, i.e.

$$0 \leq v_{\min} \leq \dot{s} \leq v_{\max} < \infty. \tag{4.9}$$

Also $\left|\tilde{T}(0)\right|$ is bounded since

$$\left|\tilde{T}(0)\right| = \left|\tilde{T}(0) - \tilde{T}(L)\right| = \left|\int_0^L \tilde{T}_x dx\right| \leq \sqrt{L}\left\|\tilde{T}_x\right\|_2. \tag{4.10}$$

As a consequence of Poincaré's inequality given in [56] (Lemma 2.1, p. 17), the estimate on $\|T\|_2$ satisfies:

$$\int_0^L T^2 dx \le 2T^2(s) + 4L^2 \int_0^L T_x^2 dx = 2T_f^2 + 4L^2 \int_0^L T_x^2 dx \ . \tag{4.11}$$

That is, both T and T_x are bounded in the $L_2(0,L)$ norm, and hence T is bounded in the Sobolev space $H^1(0,L)$. Similarly, Agmon's inequality (Lemma 2.4, p. 20, [56]) ensures that $|T|$ is also uniformly bounded.

Introduce the "enthalpy function" $\eta(T)$ defined as:

$$\eta(T) := \begin{cases} \dfrac{1}{a}T, & \text{if } T < T_f \\ \dfrac{1}{a}T + \dfrac{1}{b}, & \text{if } T \ge T_f \end{cases}. \tag{4.12}$$

In the physical system, this is proportional to the enthalpy of the material at a given temperature, given in (2.2). Denote $\tilde{\eta} := \eta(T) - \eta(\bar{T})$ as the difference in enthalpy and

$$\tilde{H} := \int_0^L \tilde{\eta} dx = \frac{1}{a}\int_0^L \tilde{T} dx - \frac{1}{b}\tilde{s}, \tag{4.13}$$

as the total difference. Taking the time derivative of this value, and using the fact that $\tilde{T}$ is continuous,

$$\frac{d\tilde{H}}{dt} = \frac{d}{dt}\left(\frac{1}{a}\int_0^L \tilde{T} dx - \frac{1}{b}\tilde{s}\right) = \frac{1}{a}\int_0^L \tilde{T}_t dx - \frac{1}{b}\dot{\tilde{s}}$$

Using equations (4.1)-(4.4),

$$\begin{aligned} \tilde{H} &= \int_0^L \tilde{T}_{xx} - \frac{1}{b}\dot{s} + \frac{1}{b}\dot{\bar{s}} \\ &= \tilde{T}_x\Big|_0^{s_1^-} + \tilde{T}_x\Big|_{s_1^+}^{s^-} + \tilde{T}_x\Big|_{s^+}^{L} + \tilde{T}_x\Big|_{s^-}^{s^+} + \tilde{T}_x\Big|_{\bar{s}^-}^{\bar{s}^+} \\ &= -\tilde{T}_x(0) + \tilde{T}_x(L) = -\tilde{u}. \end{aligned} \tag{4.14}$$

The main results of [13] is that if the reference and the actual system both satisfy assumptions (A1) and (A2), and the Neumann boundary conditions satisfies

$$u(t) = \bar{u}(t) + K\tilde{H}(t), \tag{4.15}$$

where $K > 0$, then the reference temperature error $\tilde{T}$ converges asymptotically to 0 uniformly over the domain, and the interface position error $\tilde{s}$ converges to 0 as well. However, the full-state feedback for this problem is not implementable, since only the surface temperature, but not the enthalpy, can be realistically measured during the actual casting. Therefore, the sate estimation is required.

4.3 Estimation and Output Feedback

Let $\hat{T}$ and $\hat{s}$ be the estimates of the temperature T and the interface location s, respectively. Consider the following state estimator:

$$\hat{T}_t(x,t) = a\hat{T}_{xx}(x,t), x \in (0,L) - \{\hat{s}(t)\}, \tag{4.16}$$

$$\hat{T}(\hat{s}(t),t) = T_f, \quad \hat{T}_x(0,t) = u(t), \quad \hat{T}_x(L,t) = 0, \tag{4.17}$$

$$\hat{T}(x,0) = \hat{T}_0(x), \quad \hat{s}(0) = \hat{s}_0, \tag{4.18}$$

$$\dot{\hat{s}}(t) = -b\left(\hat{T}_x\left(\hat{s}(t)^+\right) - \hat{T}_x\left(\hat{s}(t)^-\right)\right) + l(t)\left(\hat{T}(0,t) - T(0,t)\right), \tag{4.19}$$

where the initial conditions satisfy assumption (A1) and the estimation gain $l > 0$

Theorem 4.1. Suppose (T, s) is a solution to (2.24)-(2.27) with initial conditions satisfy (A1) and boundary condition satisfies (A2). $(\hat{T}, \hat{s})$ is estimation from (4.16)-(4.19) with (A1), (A2), and (A3) satisfied. Then with sufficient small estimation gain l, $\hat{T}$ converges asymptotically to T uniformly over the domain.

Proof. Consider the following Lyapunov functional candidate:

$$V := \frac{1}{2}\int_0^L (\hat{T}-T)^2\,dx - \frac{a}{b}T_f\left(\hat{s}+s\right) + 2\frac{a}{b}T_f L. \tag{4.20}$$

Without loss of generality, assuming $\hat{s} < s$. Taking the time derivative of the first term in (4.20) yields,

$$\begin{aligned}\frac{d}{dt}\frac{1}{2}\int_0^L (\hat{T}-T)^2\,dx &= \frac{1}{2}\frac{d}{dt}\left[\int_0^{\hat{s}} (\hat{T}-T)^2 \mathrm{dx} + \int_{\hat{s}}^{s} (\hat{T}-T)^2 \mathrm{dx} + \int_s^L (\hat{T}-T)^2 \mathrm{dx}\right] \\ &= \int_0^{\hat{s}} (\hat{T}-T)(\hat{T}-T)_t \mathrm{dx} + \int_{\hat{s}}^{s} (\hat{T}-T)(\hat{T}-T)_t \mathrm{dx} + \\ &\quad \int_{\hat{s}}^{L} (\hat{T}-T)(\hat{T}-T)_t \mathrm{dx}.\end{aligned} \tag{4.21}$$

Then applying (2.24) and (4.16) and integrating by parts,

$$\begin{aligned}\frac{d}{dt}\frac{1}{2}\int_0^L (\hat{T}-T)^2 \mathrm{dx} &= a\int_0^{\hat{s}} (\hat{T}-T)(\hat{T}-T)_{xx} \mathrm{dx} + a\int_{\hat{s}}^{s} (\hat{T}-T)(\hat{T}-T)_{xx} \mathrm{dx} \\ &\quad + a\int_s^L (\hat{T}-T)(\hat{T}-T)_{xx} \mathrm{dx} \\ &= a(\hat{T}-T)(\hat{T}-T)_x\Big|_0^{\hat{s}^-} - a\int_0^{\hat{s}} (\hat{T}-T)_x^2 \mathrm{dx} \\ &\quad + a(\hat{T}-T)(\hat{T}-T)_x\Big|_{\hat{s}^+}^{s_2^-} - a\int_{\hat{s}}^{s} (\hat{T}-T)_x^2 \mathrm{dx} \\ &\quad + a(\hat{T}-T)(\hat{T}-T)_x\Big|_{s^+}^{L} - a\int_s^L (\hat{T}-T)_x^2 \mathrm{dx} \\ &= -a(\hat{T}-T)\left(0\right)(\hat{T}-T)_x\left(0\right) - a(\hat{T}-T)(\hat{T}-T)_x\Big|_{\hat{s}^-}^{\hat{s}^+} \\ &\quad - a(\hat{T}-T)(\hat{T}-T)_x\Big|_{s^-}^{s^+} + aT\left(L\right)T_x\left(L\right) - a\int_0^L (\hat{T}-T)_x^2 \mathrm{dx}.\end{aligned} \tag{4.22}$$

Applying boundary conditions (2.25), (2.27), (4.17), and (4.18),

$$\begin{aligned}\frac{d}{dt}\frac{1}{2}\int_0^{\ell} (\hat{T}-T)^2 \mathrm{dx} &= \frac{a}{b}(\hat{T}(\hat{s})-T(\hat{s}))\dot{\hat{s}} - \frac{l}{b}(\hat{T}(s)-T(\hat{s}))(\hat{T}(0)-T(0)) \\ &\quad - \frac{a}{b}(\hat{T}(s)-T(s))\dot{s} - a\int_0^{\ell} (\hat{T}-T)_x^2 \mathrm{dx}.\end{aligned} \tag{4.23}$$

Differentiating the second term in (4.20) gives

$$\frac{d}{dt}\frac{a}{b}T_f(\hat{s}+s)=\frac{a}{b}T_f(\dot{\hat{s}}+\dot{s}). \tag{4.24}$$

Combining (4.23) and (4.24), yields

$$\dot{V}(t)=-a\int_0^L(\hat{T}-T)_x^2dx-\frac{a}{b}\left(T(\hat{s})\dot{\hat{s}}+\hat{T}(\hat{s})\dot{s}\right)-\frac{l}{b}(\hat{T}(s)-T(\hat{s}))(\hat{T}(0)-T(0)). \tag{4.25}$$

By weak maximum principle, $\hat{T}_x(\hat{s}^-)\geq 0$, Then, choosing

$$l\leq\frac{b\min_t\left|\hat{T}_x\left(\hat{s}^-\right)\right|}{\max_t\left|\hat{T}(0)-T(0)\right|}, \tag{4.26}$$

ensures that $\dot{\hat{s}}\geq 0$. Further on, choosing an appropriate temperature unit system (K) to ensure that both T and $\hat{T}$ are non-negative:

$$\dot{V}(t)\leq-a\int_0^L(\hat{T}-T)_x^2\mathrm{dx}-\frac{l}{b}(T_f-T(\hat{s}))(\hat{T}(0)-T(0)). \tag{4.27}$$

Applying to (4.27) the Poincaré's inequality yields,

$$\dot{V}\leq-\frac{a}{4L^2}\int_0^L(\hat{T}-T)^2dx-\frac{l}{b}(T_f-T(\hat{s}))(\hat{T}(0)-T(0)). \tag{4.28}$$

If $\hat{T}(0)-T(0)\geq 0$,

$$\dot{V}\ \leq-\frac{a}{4L^2}\int_0^L(\hat{T}-T)^2dx\leq-\frac{a}{8L^2}\int_0^L(\hat{T}-T)^2dx:=-W(\hat{T}-T). \tag{4.29}$$

If $\hat{T}(0)-T(0)<0$, the following bound exists

$$\left|(\hat{T}-T)(0)\right|=\left|(\hat{T}-T)(0)-(\hat{T}-T)(L)\right|=\ \left|\int_0^L(\hat{T}-T)_xdx\right|\leq\sqrt{L}\left\|(\hat{T}_x-T_x)\right\|_2. \tag{4.30}$$

Then,

$$\begin{aligned}\dot{V}(t) &\le -\frac{a}{4L^2}\int_0^L (\hat{T}-T)^2\,dx - \frac{l\sqrt{L}C_1}{b}(\hat{T}(0)-T(0)) \\ &\le -\frac{a}{4L^2}\int_0^L (\hat{T}-T)^2\,dx + \frac{l\sqrt{L}C_1}{b}\left\|(\hat{T}_x - T_x)\right\|_2,\end{aligned} \tag{4.31}$$

where,

$$C_1 = \max_t (T_f - T(\hat{s}(t))) > 0.$$

As mentioned in Section 4.2, T_x is uniformly bounded by a constant depending on the initial condition and the bounds on u. Therefore, there exists a constant C_2 such that

$$C_2 \ge \left\|(\hat{T}_x - T_x)\right\|_2.$$

Therefore,

$$\dot{V} \le -\frac{a}{4L^2}\int_0^L (\hat{T}-T)^2\,dx + \frac{l\sqrt{L}C_1C_2}{b}. \tag{4.32}$$

Obviously, $\left|\hat{T}-T\right|$ is bounded below by 0, and there exists an infimum. Choose

$$l(t) \le \frac{ab}{8L^{2.5}C_1C_2}\inf_{x\in(0,\max(s,\hat{s}))} |\hat{T}-T|^2. \tag{4.33}$$

Then (4.33) becomes,

$$\dot{V} \le -\frac{a}{8L^2}\int_0^L (\hat{T}-T)^2\,dx := -W(\bar{T}-T). \tag{4.34}$$

Combing (4.26) and (4.33), by choosing sufficient small l that satisfies both conditions, $\dot{V}(t)$ satisfies (4.34) for all t. Now, the infinite dimensional invariance principle in [57] (Theorem 6.3, p. 195) can be applied. Using the notation in [57], denote $\mathcal{X}$ to be $H^1(0,L)\times\mathbb{R}$, the state space of the problem, and $\mathcal{Y}$ to be $C^0(0,L)\times\mathbb{R}$. Denote $\widehat{W}$ and $\hat{V}$ to be the extensions of W and V respectively to $\mathcal{Y}$. By an application of the Rellich-Kondrachov theorem (Theorem 5.5, p. 269 in

[35]) and the Ascoli-Arzela criterion (Appendix C.7, p. 635, [35]), $\mathcal{X}$ can be shown to be compactly embedded in $\mathcal{Y}$. As noted above, the trajectories of $\hat{T} - T$ are bounded in the space $\mathcal{X}$. All conditions of the theorem are met, and therefore all trajectories of the system converge to the set

$$\mathcal{M}_3 \subset \left\{ y \in \mathcal{Y} : \hat{W}(y) = 0 \right\} = \left\{ \hat{T} - T \equiv 0 \right\},$$

in the $\mathcal{Y}$-norm. That is, $\hat{T} - T$ converges to 0 uniformly. □

Theorem 4.2. Suppose (T, s), $(\bar{T}, \bar{s})$, and $(\hat{T}, \hat{s})$ all satisfy assumptions in Theorem 4.1. Then under the control law

$$u = \bar{u} + K\left[\frac{1}{a} \int_0^L \left(\hat{T} - \bar{T} \right) dx - \frac{1}{b} \left(\hat{s} - \bar{s} \right) \right], \tag{4.35}$$

the temperature reference, $\tilde{T}$, and the estimation errors, $\hat{T} - T$, uniformly converge to 0.

Proof. The control law can be rewritten as

$$\tilde{u}(t) = K\left(\hat{H} - \bar{H} \right). \tag{4.36}$$

Taking the time derivative,

$$\begin{aligned} \dot{\tilde{u}} &= K\left[\int_0^{\ell} \left(\hat{T} - \bar{T} \right)_{xx} - \frac{1}{b} \dot{\hat{s}} + \frac{1}{b} \dot{\bar{s}} \right] \\ &= K\left[-\left(\hat{T} - \bar{T} \right)_x (0) + \left(\hat{T} - \bar{T} \right)_x (\ell) - \frac{l}{b} \left(\hat{T}(0) - T(0) \right) \right] \\ &= -K\tilde{u} - \frac{Kl}{b} (\hat{T}(0) - T(0)), \end{aligned} \tag{4.37}$$

which implies that $\tilde{u}$ converges to 0. The remainder of the proof is a Lyapunov argument on the moving boundary system, similar to the proof of Theorem 4.1.

Consider the Lyapunov functional candidate

$$V\left(\tilde{T},t\right):=\frac{1}{2}\int_0^L\tilde{T}^2dx+\frac{1}{2}\int_0^L\left(\hat{T}-T\right)^2dx-\frac{a}{b}T_f\left(\hat{s}+2s+\bar{s}\right)+4\frac{a}{b}T_fL. \tag{4.38}$$

Taking the time derivative, yields

$$\begin{aligned}\dot{V}&=-a\tilde{T}\left(0\right)\tilde{u}-a\int_0^L\tilde{T}_x^2dx-\frac{a}{b}\left(\overline{T}\left(s\right)\dot{s}+T\left(\bar{s}\right)\dot{\bar{s}}+T\left(\hat{s}\right)\dot{\hat{s}}+\hat{T}\left(s\right)\dot{s}\right)\\&\quad-a\int_0^L\left(\hat{T}-T\right)_x^2dx-\frac{l}{b}\left(T_f-T\left(\hat{s}\right)\right)\left(\hat{T}-T\right)\left(0\right)\\&\leq-\frac{a}{4L^2}\left(\int_0^L\tilde{T}^2dx+\int_0^L\left(\hat{T}-T\right)^2dx\right)-\frac{l}{b}\left(T_f-T\left(\hat{s}\right)\right)\left(\hat{T}-T\right)\left(0\right).\end{aligned} \tag{4.39}$$

Following the discussion similar to that for Theorem 4.1,

$$\dot{V}\leq-\frac{a}{4L^2}\left(\int_0^L\tilde{T}^2dx+\int_0^L\left(\hat{T}-T\right)^2dx\right). \tag{4.40}$$

Application of the invariance principle finishes the proof. □

Remark 4.3.1. It does not follow from Theorem 4.2 that the solidification front position $s,\hat{s}$ converges as well. If the temperature gradient in the reference profile, $\hat{T}$, is small, the solidification front position error may be arbitrarily large for the small temperature errors, as shown in Figure 20. For practical applications, though, this gradient is not small, and the solidification front converges to the reference position as illustrated in the simulation in Figure 21. Although the proof does not guarantee convergence, the control law in simulation has shown convergent behavior. Therefore, the following conjecture is formulated.

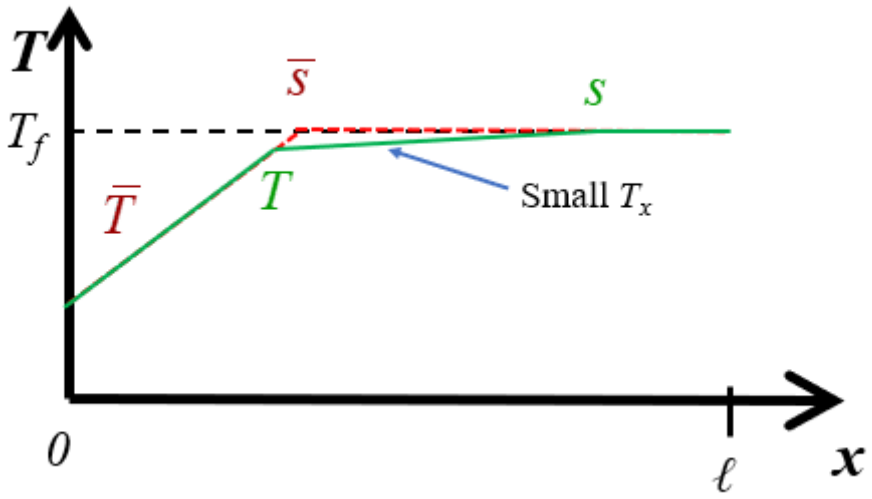

Figure 20. Convergence of $\tilde{\boldsymbol{T}}$ with arbitrary large $\tilde{\boldsymbol{s}}$.

Conjecture 4.1. Suppose (T, s), $(\bar{T}, \bar{s})$, and $(\hat{T}, \hat{s})$ all satisfy assumptions in Theorem 4.1. Then under the control law (94), the interface reference, $\tilde{s}$, and estimation errors, $\hat{s} - s$ converge to 0.

Figure 21 shows a simulation using this output-feedback control law. The initial estimation is the same as the reference, i.e. $\hat{T}_0 = \bar{T}_0, \hat{s}_0 = \bar{s}_0$. The temperature estimation error, the output temperature error, and the solidification front errors clearly converge to 0, and even appear to be converging exponentially fast, and the control action (as shown in Figure 22) remains bounded. However, this apparent result remains conjecture, and a subject of ongoing work.

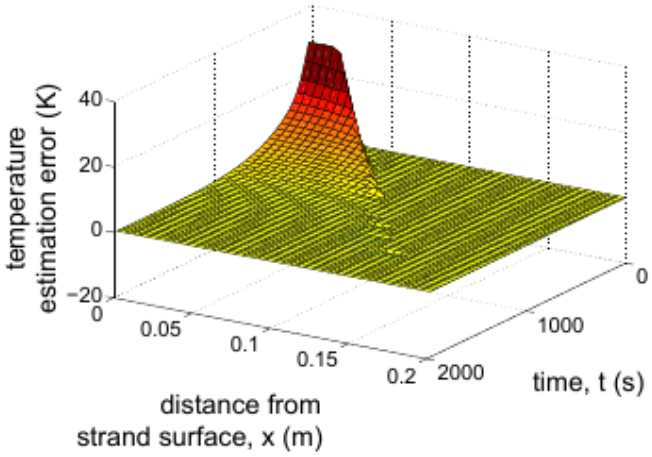

(a) Temperature estimation error $T - \tilde{T}$

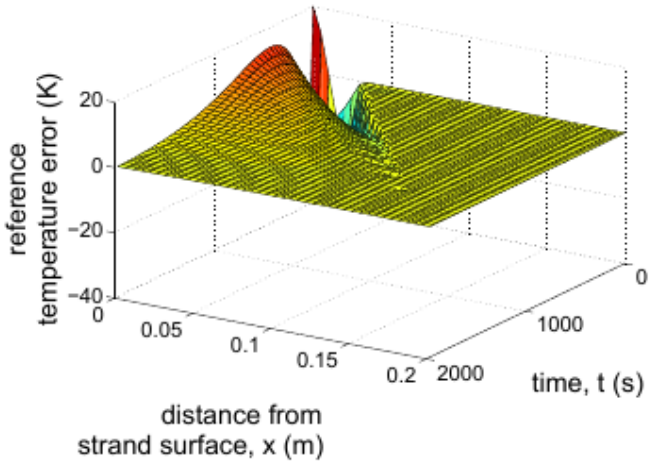

(b) Temperature error $\tilde{T}(x,t)$

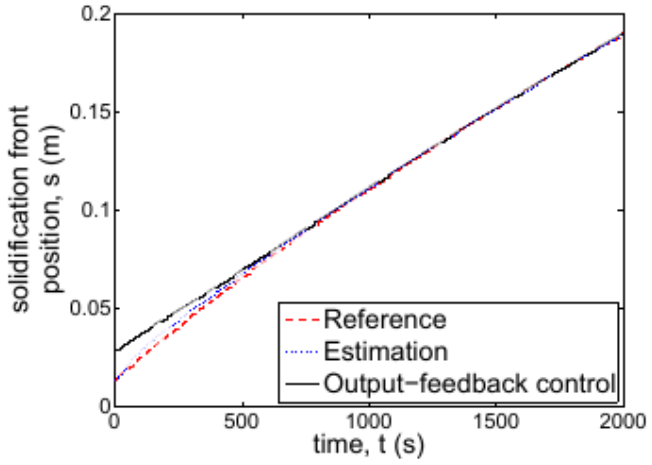

(c) Solidification front $s(t)$

Figure 21. Simulation of system (24)-(27) with initial condition mismatch and control law (94)**[13]**.

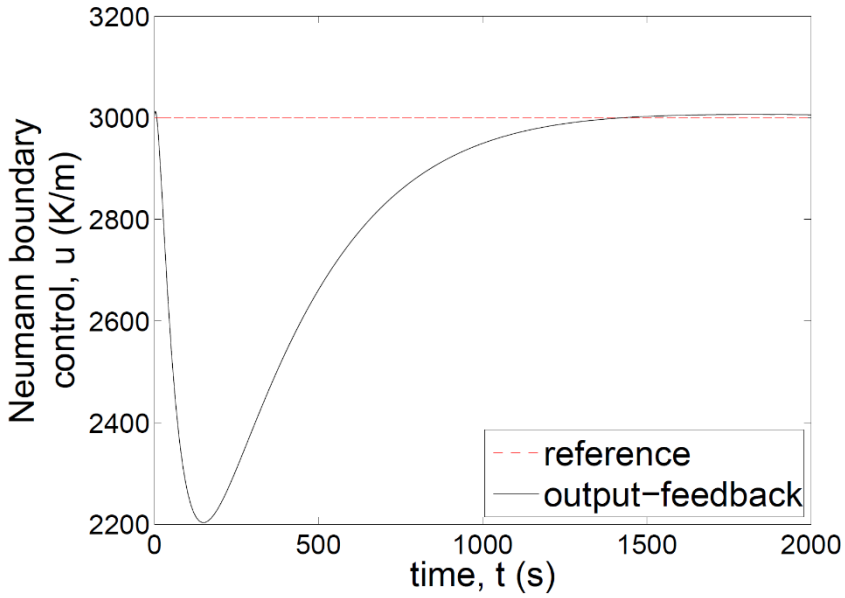

Figure 22. Output-feedback control law

Figure 23 shows a block diagram of this output-feedback law. The reliability of a temperature sensor, such as an optical pyrometer, in continuous steel casting is a serious problem due to the scale on the steel surface and the vapor in the water-cooling zone. In [51], the authors proposed online recalibration method to improve the estimate accuracy, which guarantees better control performance, using sparse discrete-in-time temperature measurements. This technique will be introduced in the next section.

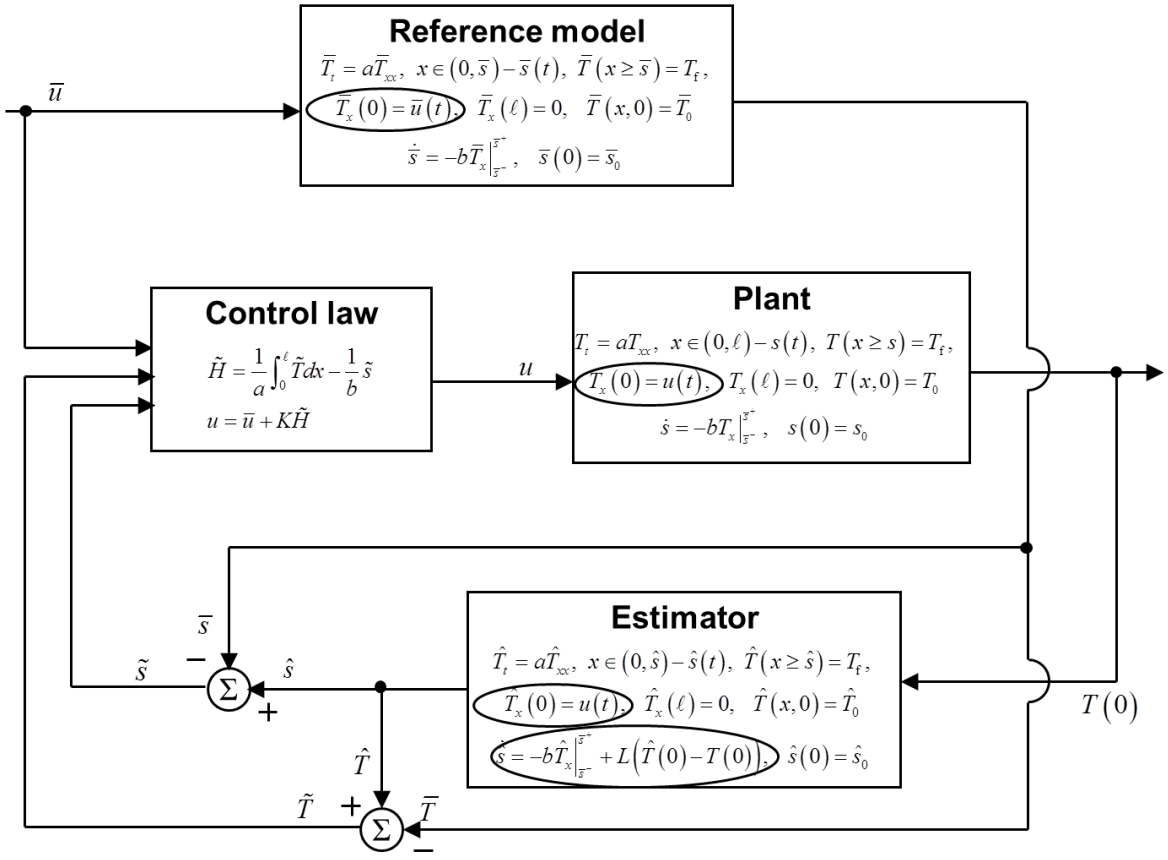

Figure 23. Block diagram of the proposed output-feedback control law.

4.4 Discrete-in-Time Recalibration

The purpose of this section is to start bridging the gap between the theoretical approach of section 4.3 and the software sensor described in section 3.3. One of the problems the model-based software sensor was developed to solve is the lack of the distributed temperature measurements in the strand. While at the mold exit the strand temperature could be reasonable estimated from the temperature difference and the flow rates of the incoming to the mold and the exiting from the mold cooling water and the high precision mold model, as the distance from the mold exit increases, the error in the model-based software sensor estimates increases as well. The only temperature measurements available in the spray zone in some casters are sparsely located

pyrometers, which are discrete-in-time with respect to the model and therefore do not lend themselves to the standard estimation techniques. However, one could attempt to "calibrate" the model - adjust its parameters to match sparse measurements - a common modeling problem. In general, this calibration problem assumes that the system dynamics are known except for a finite set of unknown parameters. In the present case of the continuous casters, the least well-known parameters are those related to the boundary heat flux.

4.4.1 Calibration of Stefan problem

Although the Stefan Problem is nonlinear, it is still parabolic in most of the strand. In addition, the unknown parameters in the boundary heat flux (3.2) all affect the heat flux monotonically: increasing the parameter increases the heat flux. Therefore, the well-known properties of parabolic PDEs, in particular the maximum principle, can be applied to the error equations.

Lemma 4.1. Let $T_1(x,t), s_1(t)$ and $T_2(x,t), s_2(t)$ be the solutions to (2.24)-(2.27), with the initial conditions $T_1(x,0) = T_2(x,0)$ and $s_1(0) \geq s_2(0)$ that satisfy (A1) and (A2), and have the same material properties a and b. Then, if the boundary heat flux satisfies

$$u_1(t) > u_2(t) \; \forall t,$$

the interface locations satisfy

$$s_2(t) \leq s_1(t) \; \forall t.$$

Proof. Suppose first that $s_1(0) > s_2(0)$. Then $s_2(t) < s_1(t)$. If not, then there exists the first time $\bar{t}$ such that $s_2(\bar{t}) = s_1(\bar{t})$. Denote $\bar{t} = \inf\{t | s_2(t) = s_1(t)\}$.

Then, for $v(x,t) = T_2(x,t) - T_1(x,t)$, we have:

$$v_t = a v_{xx},\ x \in (0, s_2), \tag{4.41}$$

$$v_x(0,t) = u_2(t) - u_1(t) < 0. \tag{4.42}$$

By weak maximum principle [35](Theorem 8, p. 389), $v(x,t)$ attains the minimum value on the parabolic boundary, i.e. minimum value attained on $t = 0$ or $x = s_2(t)$. Therefore,

$$v \geq 0,\ \forall x \in \left(0, s_2(\bar{t})\right), \forall t \in (0, \bar{t}\,]. \tag{4.43}$$

If the we have $v(x^*, t^*) = 0$ for $(x^*, t^*) \in \left(0, s_2(\bar{t})\right) \times (0, \bar{t})$, invoking the strong maximum principle [35] (Theorem 12, p. 397) we would obtain $v \equiv 0$ in $\left(0, s_2(\bar{t})\right) \times (0, t^*)$. This is inconsistent with (4.42). Thus, we have:

$$v(x,t) > 0, \forall x \in \left(0, s_2(\bar{t})\right), \forall t \in (0, \bar{t}\,]\ . \tag{4.44}$$

Then, v attains a minimum at $(s_2(\bar{t}), \bar{t}) = (s_1(\bar{t}), \bar{t})$, where

$$v\left(s_2(\bar{t}), \bar{t}\right) = 0, \tag{4.45}$$

and by the parabolic version of Hopf's Lemma:

$$v_x\left(s_2^-(\bar{t}), \bar{t}\right) < 0. \tag{4.46}$$

Now, due to (2.29) we have:

$$v_x\left(s_2^-(\bar{t}), \bar{t}\right) = s_{2t}(\bar{t}) - s_{1t}(\bar{t}), \tag{4.47}$$

which yields:

$$s_{2t}(\bar{t}) < s_{1t}(\bar{t}), \tag{4.48}$$

which is inconsistent with the definition of $\bar{t}$.

Now, suppose $s_1(0) = s_2(0)$. Let $T_\varepsilon(x,t), s_\varepsilon(t)$ be the solution to (2.24)-(2.27) with the initial conditions $u_1, T_1(0), s_1(0) + \varepsilon$. Then, from the first part of the proof, we have $s_2 < s_\varepsilon, s_1 < s_\varepsilon$.

And due to [58] (Theorem 2), we have

$$|s_1(t) - s_\varepsilon(t)| \leq C_1\varepsilon, \tag{4.49}$$

where C_1 is a constant which depends on temperature and material properties. Therefore,

$$s_2(t) < s_\varepsilon(t) \leq s_1(t) + \varepsilon. \tag{4.50}$$

Now, upon letting $\varepsilon \to 0$, we recover $s_2(t) \leq s_1(t)$. □

Lemma 4.2. Let $T_1(x,t), s_1(t)$ and $T_2(x,t), s_2(t)$ satisfy the conditions in Lemma 4.1, and have the same material properties a and b. Then, if the boundary heat fluxes satisfy

$$u_1(t) > u_2(t)\ \forall t,$$

then the temperatures satisfy

$$T_1(x,t) \leq T_2(x,t)\ \forall t, \forall x \in [0, s_1).$$

Proof. According to Lemma 4.1, $s_2(t) \leq s_1(t), \forall t$. Using weak and strong maximum principle as in the Lemma 4.1 proof yields:

$$T_1(x,t) < T_2(x,t)\ \forall t > 0, \forall x \in [0, s_2)\ . \tag{4.51}$$

On $[s_2, s_1]$, trivially by (2.30) and the maximum principle for T_1, we must have

$$T_1 < T_f = T_2. \tag{4.52}$$

Combining (4.51) and (4.52) yields

$$T_1(x,t) < T_2(x,t)\ \forall t,\ \forall x \in [0, s_1). \tag{4.53}$$

□

An immediate consequence of this Lemma is that certain simple calibration problems must have a unique solution. For example, suppose the heat flux follows (3.2), assuming that only the parameter *A* is unknown. Under the physical assumptions on the other parameters and variables in (3.2), increasing *A* increases the heat flux. Then, due to Lemma 4.1, if the pour temperature and a measurement at any single other point in the caster are available, the actual value of *A* can be found exactly.

Theorem 4.3. Let $T(x,t)$ be the solution of the single-phase Stefan problem (2.24)-(2.27) under the assumption (A1) with the boundary condition (3.2) satisfying assumption (A2), where either A or c is unknown. If the initial condition $T_0(x)$ and a measurement $T(x_{measure}, t_{measure}), x_{measure} \in [0, s_1]$, are known, the unknown parameter can be found to an arbitrary accuracy.

Proof. Applying Lemma 4.1 for a given initial condition T_0, since the heat flux (3.2) - and therefore the temperature gradient u - depends monotonically on A and c, the solution of the Stefan problem *T* will also depend monotonically on *A* and *c*. Therefore, there is a unique value of the unknown parameter that achieves a given measurement $T(x_{measure}, t_{measure})$. Furthermore, because of the monotonicity, it can be found, for example, by a simple binary search algorithm to any desired accuracy. □

4.4.2 Discussion and simulation

Clearly, this result provides a strong conclusion, but requires strict conditions. The heat flux does have a monotonic dependence on parameters A and c, but the parameters may vary throughout the caster. So, the assumption of a single missing parameter is not very likely. Nevertheless, the technique presented is seen below to provide a practical framework for recalibration based on a single measurement.

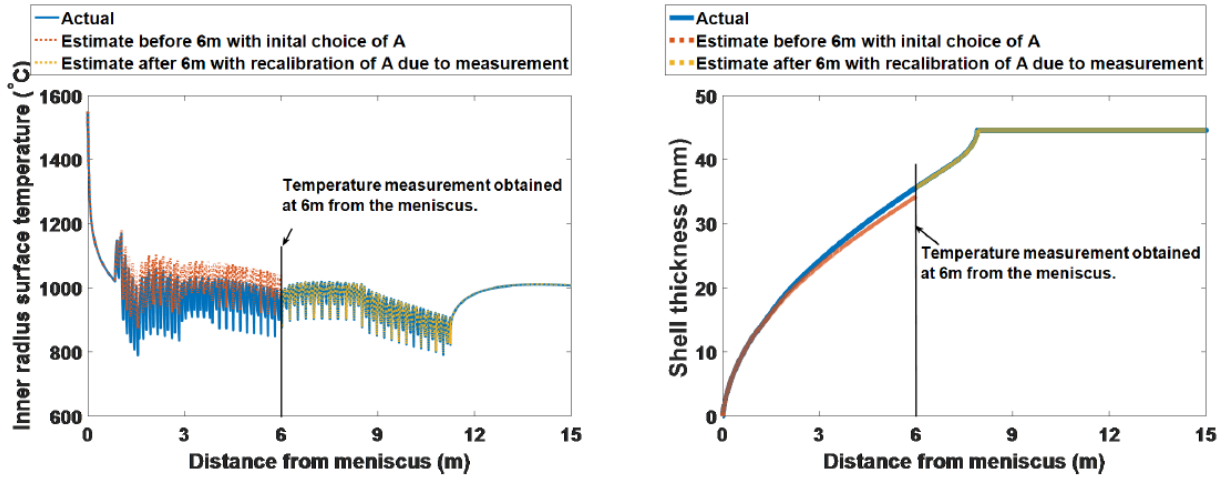

(a) Surface temperature $T(0,t)$ (b) Shell thickness $s(t)$

Figure 24. The effective specific heat based simulation showing mid-simulation calibration to match surface temperature measurement.

Figure 24 shows a simulation of an effective specific-heat-based PDE system CONSENSOR [4] based on (2.49)-(3.2), for which (2.24)-(2.27), (3.2) can be viewed as a simplified approximation. The simulation is carried out under 3 m/min constant casting speed. The simulated steel composition and spray zone input values are those given in Tables II and III of [4]. The parameters k, ρ, L_f, and c_p vary with temperature T according to [3]. Until the pyrometer is reached, at 6 m from the meniscus, the model assumes the value of A to be 1.57. In the actual system this value is 2. At 6 m from the top of the caster, a measurement of the surface temperature

is obtained, for example from a pyrometer, a dragged thermocouple, or an infrared camera. A Newton search is used to adjust A to match the measurement. The derivative is calculated numerically using a simple finite-difference approximation. Within 2 iterations, the Newton search returns a value of 1.988 for A. After setting the predicted temperature profile at 6 m to the predicted value from CONSENSOR using this value of A, the simulation is restarted and continues for the rest of the caster. As seen in Figure 24, the surface temperature and the shell thickness estimation errors are practically eliminated after recalibration at 6 m distance from the meniscus.

CHAPTER 5.

SPRAY COOLING CONTROL UNDER PROCESS INPUT HYSTERESIS

In this chapter, a free boundary problem with hysteresis type boundary conditions is considered. Hysteresis effects, which can be characterized as a special type of memory-based relation between an input signal $v(t)$ and an output signal $\omega(t)$, arise in various areas of science, such as physics, engineering, economics, and biology. There is an extensive body of research on hysteresis modeling [23], [59]. A generic approach to controlling hysteretic systems is to combine inverse compensation with feedback [25]–[27]. There are limited studies on the control of the Stefan problem with hysteresis. Hoffmann and Sprekels [60] considered a two-phase Stefan problem with hysteresis for a simple situation of thermostat control. Friedman and Hoffmann [30] considered optimal control of the free boundary of a two-phase Stefan problem with hysteresis-type boundary conditions. Periodic control of a two-phase Stefan problem with Dirichlet boundary control with hysteresis was considered in [31]. However, all these previous works propose hysteresis effects on the free boundary, rather than at the surface where heat flux is applied.

The existence of hysteresis [11] in a certain temperature interval, points to the significance of considering the thermal history of the actual cooling processes when designing controllers, which is the subject of the present chapter. The hysteresis model is given in Section 5.1. The control objective and our main result, a full-state feedback control law that guarantees simultaneous asymptotic convergence of the temperature and the solidification front location to the reference profile, are stated in Section 5.2. The results are then extended to the observer design and the output feedback control in Section 5.3. In Section 5.4 a recalibration method for an unknown hysteresis is proposed.

5.1 Hysteresis due to boiling

The heat extraction through cooling water is governed by the water boiling phenomena, which greatly depend on the temperature. In the spray-cooling region of the steel caster, cooling water droplets impinge onto the hot steel surface and vaporize immediately to form a stable steam layer. The latter prevents subsequent water droplets from coming in contact with the steel strand surface and decreases the heat removal. Time needed for the steam layer condition to change creates the hysteresis effects.

An experiment was done to determine the boiling curve from 200 ^{o}C to 1200 ^{o}C and then back to 200 ^{o}C for a Pt-specimen under air-mist spray nozzles [61]. The curves for both temperature processing histories (Figure 10 in [61]) reveal hysteresis due to boiling in the water cooling process, as time is needed for the steam layer conditions to change, and this hysteresis depends on the surface temperature of the strand. Denote $P(\cdot)$ as the hysteresis operator, then:

$$u(t) = P(T(0,t), q(t)), \tag{5.1}$$

where $q(t)$ denotes the accessible control input, i.e., the heat extraction flux due to the spray cooling water. The configuration of the process model with hysteresis is shown in Figure 25.

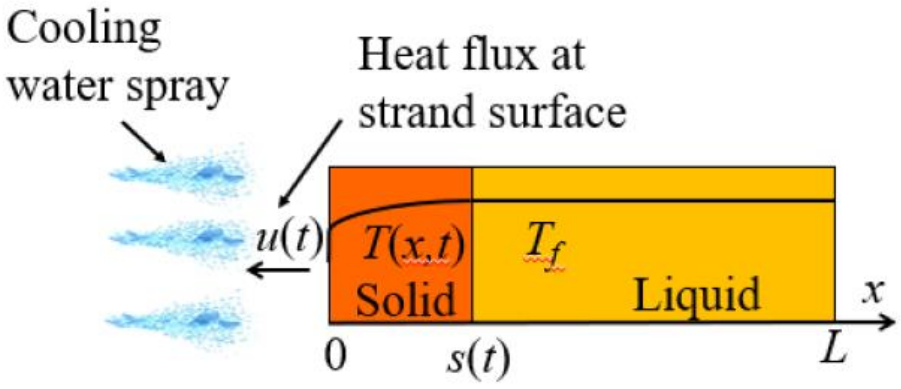

Figure 25. Schematic of 1D Stefan problem with hysteresis.

A simple way to account for boiling heat transfer effect that has been successfully used by other modelers [62] is to introduce a heat flux multiplier into equation (113)

$$P(T(0,t),q(t)) = F(T(0,t))q(t), \tag{5.2}$$

where $F\left(T_s(t)\right)$ is a simple hysteresis functional, as shown in Figure 26. Mathematically, it can be represented as follows:

$$F(T(0,t)) = \begin{cases} f_L(T(0,t)), & \text{if } \exists\, t^* \in (0,t], \text{ s.t. } T(0,t^*) \geq T_\beta \\ & \text{and } T(0,\tau) > T_\alpha \forall\, \tau \in [t^*,t], \\ 1, & \text{if } T(0,t) < T_\alpha \text{ or } T(0,t) > T_\beta, \\ f_H(T(0,t)), & \text{if } \exists\, t^* \in (0,t], \text{ s.t. } T(0,t^*) \leq T_\alpha \\ & \text{and } T(0,\tau) < T_\beta \forall\, \tau \in [t^*,t], \end{cases} \tag{5.3}$$

where $f_L(\cdot), f_H(\cdot)$ are heat flux multipliers.

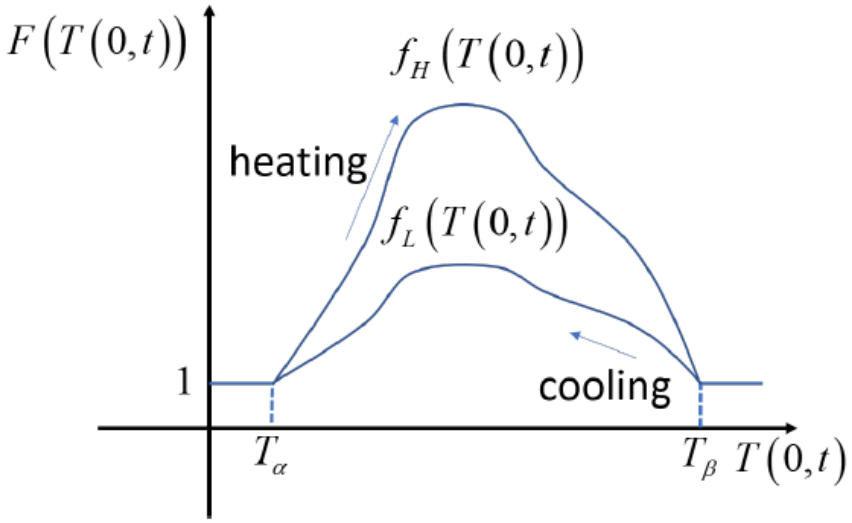

Figure 26. Hysteresis loop due to boiling.

5.2 Full-state Feedback Controller Design with the Known Hysteresis

5.2.1 Controller design via hysteresis inverse

For this section, the heat flux multipliers are assumed known. For example, they can be measured through lab experiments. The following assumption is made for the hysteresis functional.

(A4) Functions $f_L(\cdot)$ and $f_H(\cdot)$ are known and continuous. For example, they can be measured in the laboratory through experiments.

A generic approach to controlling hysteretic systems is to design hysteresis compensation, like inversion operator [25] to ensure accurate control. As shown in Figure 27, given the desired boundary heat flux $u_d(t)$ and the initial memory of hysteresis operator $F(\cdot)$, the inverse operator $F^{-1}(\cdot)$ generates the required cooling water heat flux $q(t)$ to ensure $u = u_d$.

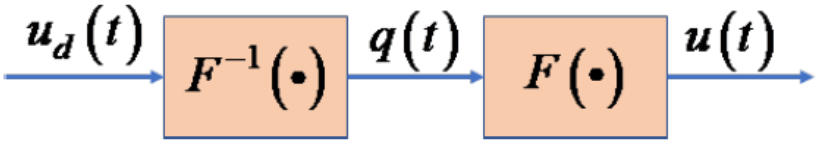

Figure 27. Illustration of the hysteresis inversion.

5.2.2 Existence of solution

Theorem 5.1. Under the assumptions (A1), (A2), and (A4), there exists a solution to (2.24)-(2.27) with boundary condition (5.1), which is defined for all $t > 0$.

Proof. Since typically $T_0(0) > T_\beta$, without loss of generality we assume $F\big(T_0(0)\big) = 1$. Take any small $\delta > 0$ and define:

$$F^\delta(t) \equiv 1, \forall 0 < t < \delta .$$

Based on Theorems 2.3.1 and 2.3.2, a unique solution to (2.24)-(2.27) with boundary condition (5.1) exists. Denote the solution as $\left(\mathrm{T}^{\mathrm{lta}}, \mathrm{s}^{\delta}\right)$. Next, define

$$F^{\delta}(t) = F(T(0, t-\delta)), \text{ for } \delta < t < 2\delta \tag{5.4}$$

Since $F^{\delta}(t)$ is known for this interval, (2.24)-(2.27) can be solved for $\delta < t < 2\delta$ with this $F^{\delta}(t)$ and with the initial values $\left(T^{\delta}(x, \delta), s^{\delta}(t)\right)$.

Now, define $F^{\delta}(t)$ for $2\delta < t < 3\delta$ as above in terms of the function $T(0, t)$ obtained in the second step, and solve (2.24)-(2.27) for $2\delta < t < 3\delta$. Continuing this way, we obtain a unique solution of (2.24)-(2.27) with boundary condition (5.1) with $F(t) = F^{\delta}(t)$.

From Lemma 2.1, there exists a constant $C > 0$ such that

$$0 \le \frac{d}{dx} T^{\delta}\left(s^{\delta-}, t\right) \le C \tag{5.5}$$

i.e.,

$$0 \le \dot{s}^{\delta}(t) \le C. \tag{5.6}$$

which implies that the functions s^{δ} form an equicontinuous, uniformly bounded family. Hence Ascoli-Arzela's theorem holds and we can select a subsequence s_{δ} that converges uniformly to $s(t)$ as $\delta \to 0$, and T^{δ} converges uniformly to T, i.e. (T, s) will be a solution. □

5.2.3 Enthalpy-based controller design

Theorem 5.2. Suppose the initial conditions satisfy assumption (A1), the reference profile satisfies assumptions (A2) and (A3), and the boundary condition satisfies the control law

$$q(t) = F^{-1}\left(T(0,t)\right) F\left(\bar{T}(0,t)\right) \bar{q}(t) + K F^{-1}\left(T(0,t)\right) \tilde{H}(t) \tag{5.7}$$

where K is the controller gain, F satisfies (A4), and $F^{-1}(\cdot)$ denotes the hysteresis inverse. Then, the reference temperature error $\tilde{T}$ converges asymptotically to 0 uniformly over the domain, and the free boundary error $\tilde{s}$ also converges to 0 asymptotically.

Proof. First, using equations (4.5)-(4.8), we have

$$\dot{\tilde{H}} = -\tilde{T}_x(0) + \tilde{T}_x(L) = -(F(T(0,t))q(t) - F(\bar{T}(0,t))\bar{q}(t)).$$

Then, applying control law (5.7) yields

$$\dot{\tilde{H}} = -K\tilde{H},$$

i.e., $|\tilde{H}|$ decreases exponentially. As noted in Section 4.2, if all the assumptions are satisfied, T, $\bar{T}$, and consequently also $\tilde{T}$ are bounded in $H^1(0,L)$ over time. Then $|\tilde{s}|$ must also be bounded.

The remainder of the proof is similar to the main proof given in Theorem 4.1. Consider the same Lyapunov functional candidate

$$V(T) = \frac{1}{2}\int_0^L T^2 dx - \frac{a}{b}T_f(s + \bar{s}) + 2\frac{a}{b}T_f L, \tag{5.8}$$

on the state space of the error system, $(\tilde{T}, \tilde{s}) \in H^1(0, L) \times R$. This function is clearly continuous on that space, and non-negative on the trajectories of the system.

Taking the time derivative of the first term of (5.8) along the trajectory of the system yields:

$$\begin{aligned}\frac{d}{dt}\frac{1}{2}\int_0^L \tilde{T}^2 dx = &-a\tilde{T}(0)(F(T_s(t))q(t) - F(\bar{T}_s(t))\bar{q}(t)) \\ &- a\int_0^L \tilde{T}_x^2 dx + \frac{a}{b}\tilde{T}(s)\dot{s} - \frac{a}{b}\tilde{T}(\bar{s})\dot{\bar{s}}.\end{aligned} \tag{5.9}$$

Also, note that,

$$(F(T_s(t))q(t) - F(\bar{T}_s(t))\bar{q}(t)) = K\tilde{H} = K\tilde{H}(0)e^{-Kt} \tag{5.10}$$

Differentiating the second term in (5.8) gives

$$\frac{d}{dt}\frac{a}{b}T_f\left(s+\bar{s}\right)=\frac{a}{b}T_f\left(\dot{s}+\dot{\bar{s}}\right). \tag{5.11}$$

Combining the above equations yields

$$\dot{V}\left(\tilde{T}\right)=-a\tilde{T}(0)K\tilde{H}(0)e^{-Kt}-a\int_0^L\tilde{T}_x^2dx-\frac{a}{b}\left(\bar{T}\left(s\right)\dot{s}+T\left(\bar{s}\right)\dot{\bar{s}}\right). \tag{5.12}$$

From (4.10), the first term is exponentially decreasing. Under the assumptions, both $\dot{s}$ and $\dot{\bar{s}}$ are positive and bounded below, as discussed above. Since the temperatures are bounded, choosing an appropriate temperature scale ensures that $\bar{T}(s)$ and $T(\bar{s})$ are also non-negative. So, after enough time,

$$\dot{V}\left(\tilde{T}\right)\le-a\int_0^L\tilde{T}_x^2 \tag{5.13}$$

Then, applying the Poincare inequality,

$$\begin{aligned}-a\int_0^L\tilde{T}_x^2dx&\le-\frac{a}{4L^2}\int_0^L\tilde{T}^2dx+2\tilde{T}^2\left(L\right)\\&=-\frac{a}{4L^2}\int_0^L\tilde{T}^2dx=-W\left(\tilde{T}\right).\end{aligned} \tag{5.14}$$

Now, the invariance principle can be applied. Using the notation of [35], let $\mathcal{X}$ now be $(\mathrm{H}^1(0,\mathrm{L})\times\mathrm{R}$, the state space of the problem, and $\mathcal{Y}$ be $C^0(0,L)\times\mathrm{R}$. Denote $\widehat{W}$ to be the extension of W to $\mathcal{Y}$. Then, $\mathcal{X}$ is compactly embedded in $\mathcal{Y}$ according to Rellich-Kondrachov theorem and the Ascoli-Arzela criterion [35]. The trajectories of the error system are bounded in $\mathcal{X}$. All conditions of the theorem are met, and therefore all trajectories of the system converge to the set

$$\mathcal{M}_3\subset\left\{y\in\mathcal{Y}:\hat{W}\left(y\right)=0\right\}=\left\{\tilde{T}\equiv0\right\}$$

in the $\mathcal{Y}$-norm. That is, $\tilde{T}$ converges to 0 uniformly. Finally, since both $\tilde{T}$ and $|\tilde{H}|$ converge to 0, according to the definition of $\tilde{H}$, $\tilde{s}$ must converge to 0 as well.

5.2.4 Numerical simulation

For simplicity and illustration in simulation, the hysteresis effect,

$$F(\cdot) = F\left(T_\alpha, T_1, T_2, T_3, T_\beta, \alpha_1, \alpha_2, \alpha_3, \beta_1, \beta_2, \beta_3; \cdot\right)$$

is parameterized by the constants $T_\alpha, T_1, T_2, T_3, T_\beta, \alpha_1, \alpha_2, \alpha_3, \beta_1, \beta_2, \beta_3$ and described in terms of connected straight lines [62] as shown in Figure 28.

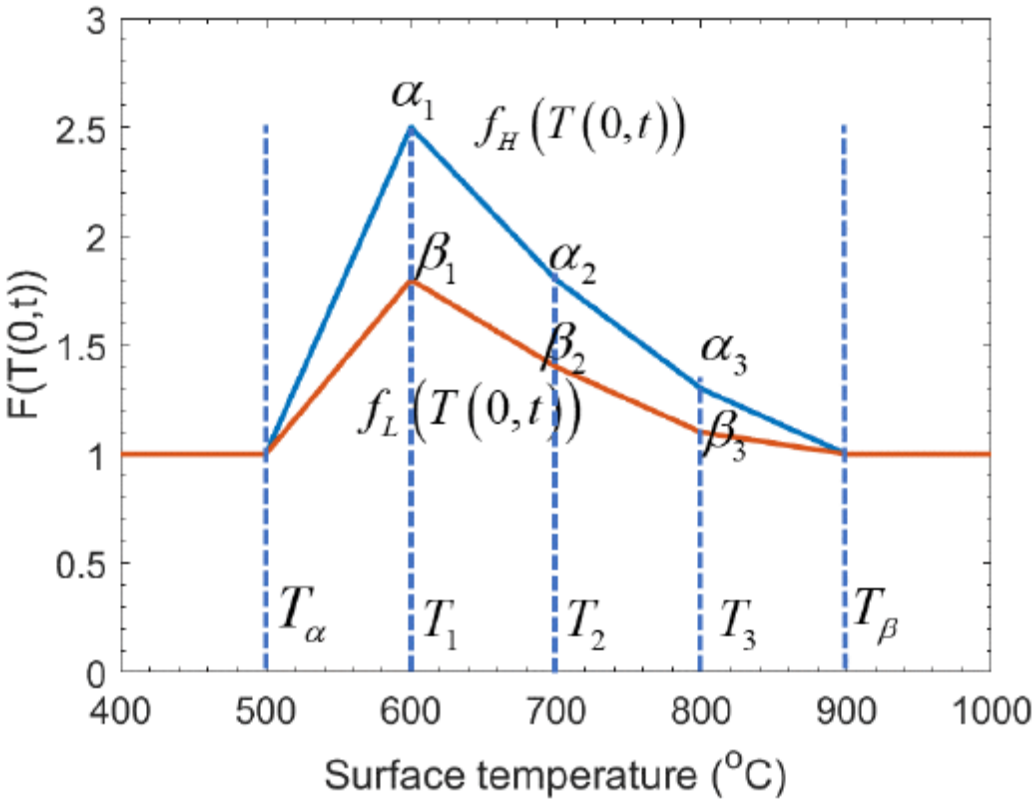

Figure 28. A hysteresis loop due to boiling.

The performance of the proposed hysteresis compensated controller is investigated through the numerical simulation by comparing its performance to that of the controller

$$q(t) = \bar{q}(t) + K\tilde{H}(t), \tag{5.15}$$

which is the previous uncompensated controller design for the Stefan problem [13]. The specific initial conditions used are shown in Figure 29, the hysteresis functional used is given in terms of the line segments shown in Figure 28, and the rest of the simulation parameters are given in Table 2. Varying $\bar{q}$ is used to simulate the spray zone, and the bounds of the control input are set to $q_L = 0.01\bar{q},\ q_H = 5\bar{q}$.

Table 2. Thermodynamic properties used in simulations.

Symbol	Description	Value
k	thermal conductivity	80.4 W/m · K
c_p	specific heat	460 J/kg · K
T_f	melting temperature	1538 °C
L	half-thickness of strand	0.002 m
ρ	density	7.87×10^3 kg/m^3

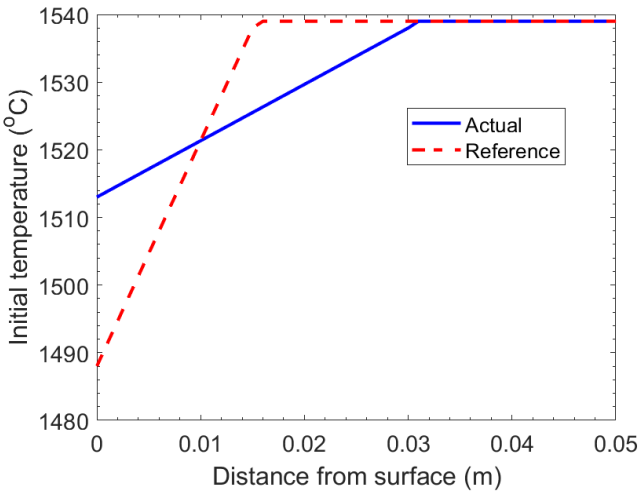

Figure 29. Initial condition for simulations.

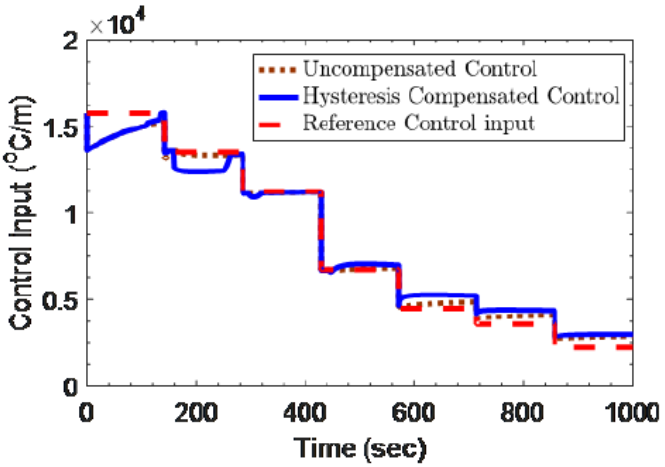

Figure 30. Boundary control $\boldsymbol{q(t)}$ with the control law (5.7).

The behavior of the surface temperature reference error, $\tilde{T}(0,t)$, the closed-loop response of the moving boundary $s(t)$, and the manipulated heat flux, $q(t)$ are depicted in Figure 31, Figure 32, and Figure 30, respectively. Hysteresis compensated control and uncompensated control show similar performance in driving $s(t)$ to $\bar{s}(t)$. However, for the surface temperature, the compensated control ensures that $\mathrm{eT}(0,\mathrm{t}) \to 0$, while the uncompensated control does not provide such a behavior. Due to the existence of the hysteresis, the compensated control varies more than the uncompensated control to account for the effects of the hysteresis.

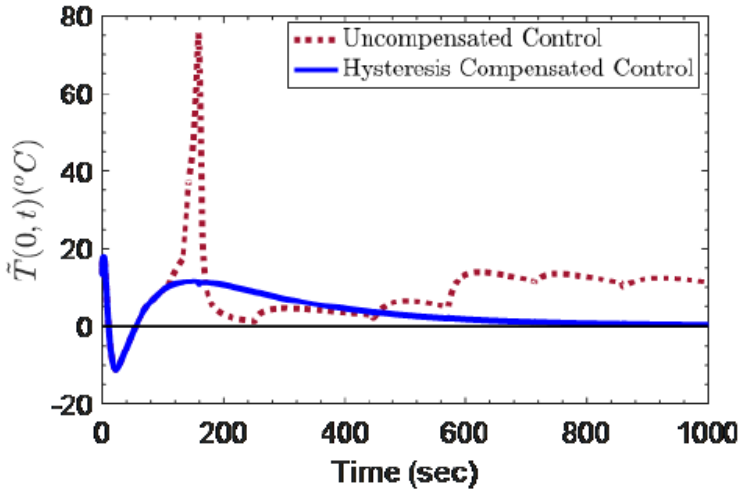

Figure 31. Temperature error $\tilde{\boldsymbol{T}}(\mathbf{0},\boldsymbol{t})$.

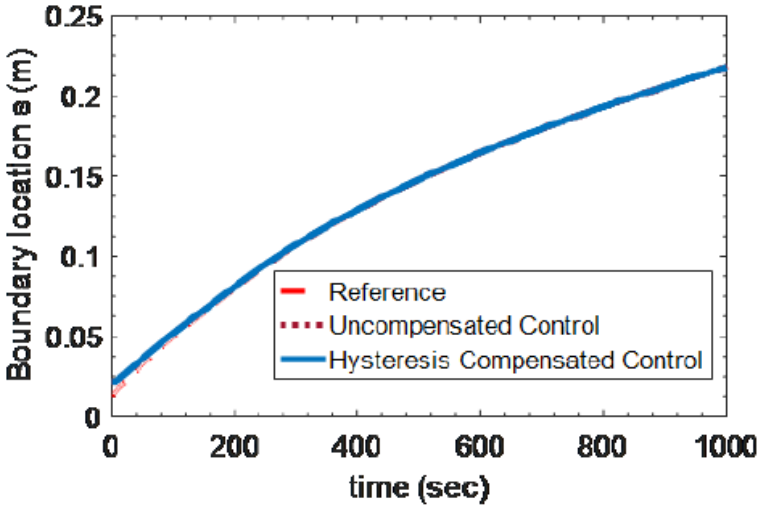

Figure 32. Solidification front $\boldsymbol{s(t)}$.

5.3 Enthalpy-based Output Feedback Control with Known Hysteresis

As mentioned in the previous Chapter, for the continuous casting process, only surface temperature measurement $T(0,t)$ is available, so the practical relevance of the full-state feedback controller is relatively limited. In this section, the controller from Section 5.2 is extended, considering surface temperature as the only available measurement.

5.3.1 Observer design

Denote the estimate of the temperature by $\hat{T}(x,t)$, and the estimate of the solidification front by $\hat{s}(t)$. Consider the following estimator:

$$\hat{T}_t(x,t) = a\hat{T}_{xx}(x,t),\ 0 \le x \le s(t) \tag{5.16}$$

$$\hat{T}(\hat{s}(t),t) = T_f, \tag{5.17}$$

$$\hat{T}_x(0,t) = F(T(0,t))q(t), \tag{5.18}$$

$$\hat{T}(x,0) = \hat{T}_0(x),\ \hat{s}(0) = \hat{s}_0 > 0 \tag{5.19}$$

$$\dot{\hat{s}}(t) = -b\left(\hat{T}_x\left(\hat{s}(t)^+\right) - \hat{T}_x\left(\hat{s}(t)^-\right)\right) + l\left(\hat{T}(0,t) - T(0,t)\right), \tag{5.20}$$

where the initial conditions satisfy the assumption (27) and the estimation gain $l > 0$.

Theorem 5.3. Consider the observer system (5.16)-(5.20). Suppose the assumptions (A1)–(A4) are satisfied. Then, with the sufficiently small estimation gain $l(t)$, $\hat{T}$ converges asymptotically to T.

Proof. Since (5.16) is parabolic on the sub-domains, if (A1) holds, then T_x is uniformly bounded (see, e.g., Theorem 11.1 from Section III.11, p. 211 of [55]) by a constant depending on the initial condition and the bounds on $q(t)$. Due to (5.20), this means that the solidification front speed is bounded, i.e.

$$0 \le v_{\min} \le \dot{s} \le v_{\max} < \infty. \tag{5.21}$$

Consider the following Lyapunov functional candidate

$$V\left(T - T\right) := \frac{1}{2}\int_0^L \left(T - T\right)^2 \mathrm{dx} - \frac{a}{b}T_f\left(\hat{s} + s\right) + 2\frac{a}{b}T_f L \tag{5.22}$$

Taking the time derivative of (5.22) yields

$$\dot{V} = -a\int_0^L \left(T_x - T_x\right)^2 \mathrm{dx} - \frac{a}{b}\left(T\left(\hat{s}\right)\dot{\hat{s}} + T\left(s\right)\dot{s}\right) - \frac{l}{b}\left(T\left(\hat{s}\right) - T\left(\hat{s}\right)\right)\left(T\left(0\right) - T\left(0\right)\right). \tag{5.23}$$

By the weak maximum principle, $\hat{T}_x(\hat{s}^-) \ge 0$, then choosing

$$l(t) \le \frac{b \min_t \left|T_x\left(\hat{s}^-\right)\right|}{\max_t \left|T\left(0\right) - T\left(0\right)\right|}, \tag{5.24}$$

ensures that $\dot{\hat{s}} \ge 0$. Choosing an Kalvin temperature scale to ensure $\hat{T}(s)$ and $T(\hat{s})$ are non-negative yields

$$\dot{V} \le -a\int_0^L \left(T_x - T_x\right)^2 \mathrm{dx} - \frac{l}{b}\left(T_f - T\left(\hat{s}\right)\right)\left(T(0) - T(0)\right), \tag{5.25}$$

Then, application of the Poincaré inequality yields

$$\dot{V} \le -\frac{a}{4L^2}\int_0^L \left(T - T\right)^2 \mathrm{dx} - \frac{l}{b}\left(T_f - T\left(\hat{s}\right)\right)\left(T - T\right)(0). \tag{5.26}$$

Since $T(\hat{s}) \le T_f$, if $\left(\hat{T} - T\right)(0) \ge 0$,

$$\dot{V} \le -\frac{a}{4L^2}\int_0^L \left(T - T\right)^2 \mathrm{dx} \ \le -\frac{a}{8L^2}\int_0^L \left(T - T\right)^2 \mathrm{dx} := -W\left(T - T\right). \tag{5.27}$$

If $\left(\hat{T} - T\right)(0) < 0$,

$$\left|\left(T - T\right)(0)\right| = \left|\int_0^L \left(T - T\right)_x \mathrm{dx}\right| \le \sqrt{L}\left\|T_x - T_x\right\|_2 . \tag{5.28}$$

Therefore,

$$\dot{V} \le -\frac{a}{4L^2}\int_0^L \left(T - T\right)^2 \mathrm{dx} - \frac{l\sqrt{L}C_1}{b}\left\|T_x - T_x\right\|_2 , \tag{5.29}$$

where,

$$C_1 = \max_t (T_f - T(\hat{s}(t))) > 0. \tag{5.30}$$

Since T_x is uniformly bounded by a constant depending on the initial condition and the bounds on u, there exists a constant C_2 such that

$$\left\|T_x - T_x\right\|_2 \le C_2. \tag{5.31}$$

Therefore,

$$\dot{V} \le -\frac{a}{4L^2}\int_0^L \left(T - T\right)^2 \mathrm{dx} + \frac{l\sqrt{L}C_1C_2}{b}. \tag{5.32}$$

Obviously, $\left|\hat{T} - T\right|$ is bounded below by 0, and there exists an infimum. Choose

$$l \le \frac{ab}{8L^{2.5}C_1C_2}\inf\left|T-T\right|^2. \tag{5.33}$$

Then (5.32) becomes,

$$\dot{V} \le -\frac{a}{8L^2}\int_0^L \left(T-T\right)^2 \mathrm{dx} := -W\left(T-T\right) \tag{5.34}$$

Combining (5.24) and (5.33), and choosing sufficient small l that satisfies both conditions, $\dot{V}(t)$ satisfies (5.34) for all t.

Now, the invariance principle [57] can be applied as in Theorem 4.1. following the same definition of $\mathcal{X}$ and *W*. It can be shown that all trajectories of the system converge to the set

$$M_3 \subset \left\{y \in Y : W\left(y\right)=0\right\} = \left\{T-T \equiv 0\right\}, \tag{5.35}$$

in the $\mathcal{Y}$-norm. That is, $\hat{T}-T$ converges to 0 uniformly. □

5.3.2 Output feedback control

The design of the output feedback controller is achieved using the reconstruction of the state through the observer defined through (5.16)-(5.20) and based on the only measurement $T(0,t)$.

Theorem 5.4. Suppose (T,s), $(\bar{T},\bar{s})$, and $\left(\hat{T},\hat{s}\right)$ all satisfy the conditions of Theorem 5.3. Then, under the control law

$$\begin{aligned} q = {} & F^{-1}(T(t,0))F(\bar{T}(t,0))\bar{q} \\ & - F^{-1}(T(t,0))K\left(\frac{1}{a}\int_0^L\left(\hat{T}-\bar{T}\right)dx - \frac{1}{b}\left(\hat{s}-\bar{s}\right)\right), \end{aligned} \tag{5.36}$$

the temperature reference error $\tilde{T}$ and estimation error $\hat{T}-T$uniformly converge to 0.

Proof. The control law can be rewritten as

$$\tilde{u}(t) = F\left(T(0,t)\right)q(t) - F\left(\bar{T}(0,t)\right)\bar{q} = K\left(\frac{1}{a}\int_0^L \left(\hat{T} - \bar{T}\right)dx - \frac{1}{b}\left(\hat{s} - \bar{s}\right)\right), \tag{5.37}$$

Taking the time derivative,

$$\begin{aligned}\dot{\tilde{u}} &= K\left[\int_0^\ell \left(\hat{T} - \bar{T}\right)_{xx} - \frac{1}{b}\dot{\hat{s}} + \frac{1}{b}\dot{\bar{s}}\right] \\ &= K\left[-\left(\hat{T} - \bar{T}\right)_x(0) + \left(\hat{T} - \bar{T}\right)_x(\ell) - \frac{l}{b}\left(\hat{T}(0) - T(0)\right)\right] \\ &= -K\tilde{u} - \frac{Kl}{b}(\hat{T}(0) - T(0))\end{aligned} \tag{5.38}$$

Since $\hat{T} \to T$, (5.38) implies that $\hat{u} \to 0$. The remainder of the proof is a Lyapunov argument for the moving boundary system similar to that in the proof of Theorem 5.3.

Consider the following Lyapunov functional candidate:

$$V\left(\tilde{T}, t\right) := \frac{1}{2}\int_0^L \tilde{T}^2 dx + \frac{1}{2}\int_0^L \left(\hat{T} - T\right)^2 dx - \frac{a}{b}T_f\left(\hat{s} + 2s + \bar{s}\right) + 4\frac{a}{b}T_f L \tag{5.39}$$

Taking the time derivative, yields

$$\begin{aligned}\dot{V} &= -a\tilde{T}(0)\tilde{u} - a\int_0^L \tilde{T}_x^2 dx - \frac{a}{b}\left(\bar{T}(s)\dot{s} + T(\bar{s})\dot{\bar{s}} + T(\hat{s})\dot{\hat{s}} + \hat{T}(s)\dot{s}\right) \\ &\quad - a\int_0^L \left(\hat{T} - T\right)_x^2 dx - \frac{l}{b}\left(T_f - T(\hat{s})\right)\left(\hat{T} - T\right)(0) \\ &\le -\frac{a}{4L^2}\left(\int_0^L \tilde{T}^2 dx + \int_0^L \left(\hat{T} - T\right)^2 dx\right) - \frac{l}{b}\left(T_f - T(\hat{s})\right)\left(\hat{T} - T\right)(0)\end{aligned} \tag{5.40}$$

Following the discussion similar to that for Theorem 5.3,

$$\dot{V} \le -\frac{a}{4L^2}\left(\int_0^L \tilde{T}^2 dx + \int_0^L \left(\hat{T} - T\right)^2 dx\right) \tag{5.41}$$

Application of the invariance principle finishes the proof.

□

5.3.3 Numerical simulation

The specific initial conditions used are shown in Figure 29, the hysteresis functional used is formed by the line segments as shown in Figure 28, and the rest of the simulation parameters are given in Table 2. Varying q is used to simulate the spray zone, and the bounds of the control input are set to $q_L = 0.01\bar{q}$ and $q_H = 5\bar{q}$. The controller gain and the estimator gain parameter are chosen as K =0.01 and $l = 2 \times 10^{-5}$, respectively.

The behavior of the surface temperature reference tracking error $\tilde{T}(0,t)$, the closed-loop response of the moving boundary, $s(t)$, and the manipulated heat flux, $q(t)$, are depicted in Figure 33. The hysteresis-compensated control and the uncompensated control show similar performance in driving $s(t)$ to $\bar{s}(t)$. However, for the surface temperature, the hysteresis-compensated control ensures that $\tilde{T}(0,t) \to 0$ while the uncompensated control does not provide such a behavior. Due to the existence of the hysteresis, the compensated control varies more compared to the uncompensated control to account for the effects of the hysteresis.

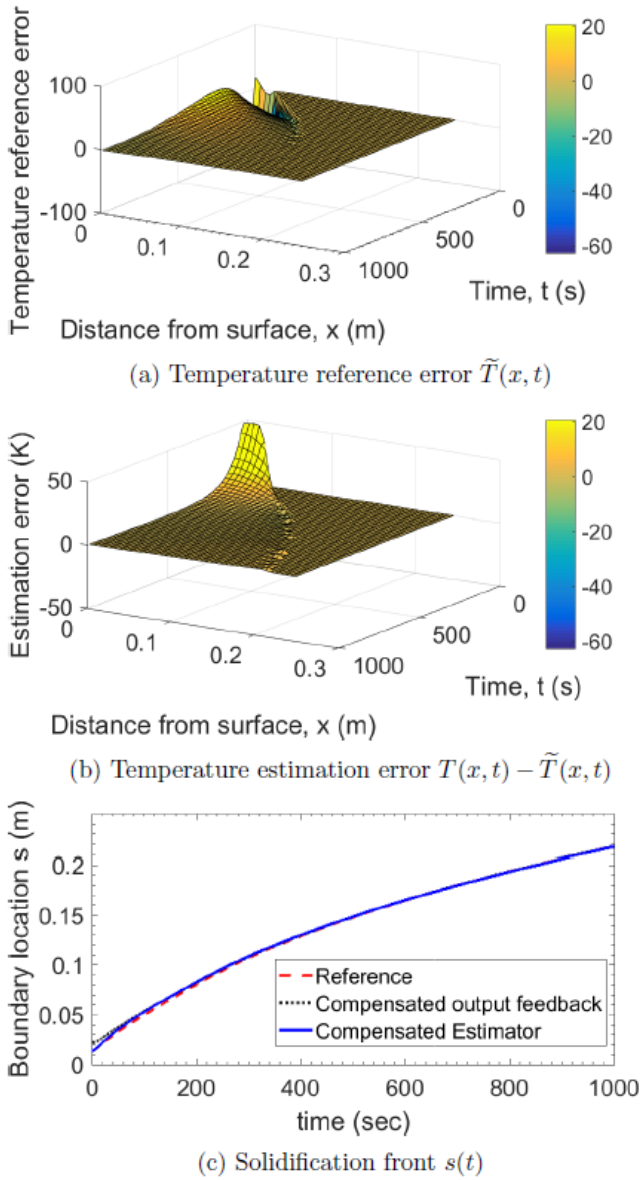

(a) Temperature reference error $\widetilde{T}(x,t)$

(b) Temperature estimation error $T(x,t) - \widetilde{T}(x,t)$

(c) Solidification front $s(t)$

Figure 33. Simulation of system (2.24)-(2.27) with the initial condition mismatch under the control law (148) with the estimator (5.16)-(5.20).

5.4 Recalibration Design for Unknown Hysteresis

A major weakness of the problem formulation in Section 5.2 lies in the assumption that the hysteresis operator F is known. The heat flux at the boundary of the steel can be measured in the laboratory setting like in [61], but the actual environment of the continuous casting process would be more complicated. The grade of the steel may also change due to the customer needs. Therefore,

in the actual application, the control problem is associated with an unknown hysteresis. An additional error will be introduced between the estimation of the hysteresis operator $\hat{F}\big(T(0,t)\big)$ and the actual hysteresis effect $F\big(T(0,t)\big)$.

5.4.1 Hysteresis model

For simplicity, in this section the hysteresis effect,

$$F(\cdot) = F\left(T_\alpha, T_\beta, k_1, k_2, g_1, g_2; \cdot\right),$$

is parameterized by constants $T_\alpha, T_\beta, k_1, k_2, g_1, g_2$ as shown in Figure 34, which is a simplified version of the water boiling effect model introduced in [62].

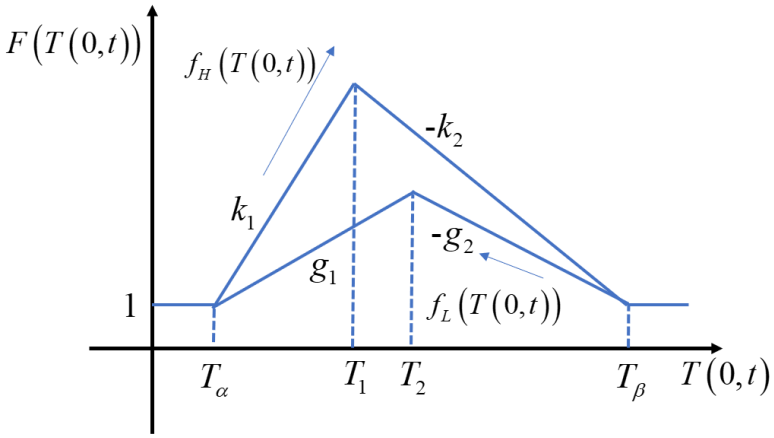

Figure 34. Hysteresis loop due to boiling.

Mathematically, the hysteresis can be expressed as

$$f_H(T(0,t)) = \begin{cases} 1 & \text{if } T(0,t) \le T_\alpha, \\ 1 + k_1(T - T_\alpha) & \text{if } T_\alpha < T(0,t) \le T_1 \\ 1 + k_2(T_\beta - T) & \text{if } T_1 < T(0,t) \le T_\beta \\ 1 & \text{if } T_\beta \le T(0,t) \end{cases} \tag{5.42}$$

And

$$f_L(T(0,t)) = \begin{cases} 1 & \text{if } T(0,t) \le T_\alpha, \\ 1+g_1(T-T_\alpha) & \text{if } T_\alpha < T(0,t) \le T_1 \\ 1+g_2(T_\beta - T) & \text{if } T_1 < T(0,t) \le T_\beta \\ 1 & \text{if } T_\beta \le T(0,t) \end{cases} \tag{5.43}$$

where,

$$\begin{cases} T_1 = \dfrac{k_1 T_\alpha + k_2 T_\beta}{k_1 + k_2}, \\ T_2 = \dfrac{g_1 T_\alpha + g_2 T_\beta}{g_1 + g_2}. \end{cases} \tag{5.44}$$

Typically, the pouring temperature $T(x, 0)$ is much higher than T_β. Therefore, the hysteresis law is defined as follows: set $F(T(0,0)) = 1$, and $F\big(T(0,0)\big) = f_L\big(T(0,0)\big)$. For $k \in N \cup \{0\}$, define

$$t_{k+1}^* = \begin{cases} \inf G_{k+1} & \text{if } G_{k+1} \neq \varnothing \\ \infty & \text{if } G_{k+1} = \varnothing \end{cases} \tag{5.45}$$

where,

$$G_{k+1} = \left\{ t \in (t_k^*, \infty); T\left(0,t\right) = \begin{cases} T_\beta & k+1 \text{ even} \\ T_\alpha & k+1 \text{ odd} \end{cases} \right\}, \tag{5.46}$$

and,

$$u(t) = F\left(T\left(0,T\right)\right) q\left(t\right) = \begin{cases} f_L\left(T\left(0,t\right)\right) q(t) & \text{if } t \in [t_k^*, t_{k+1}^*) \\ & \text{and } k+1 \text{ odd}, \\ f_H\left(T\left(0,t\right)\right) q(t) & \text{if } t \in [t_k^*, t_{k+1}^*) \\ & \text{and } k+1 \text{ even}. \end{cases} \tag{5.47}$$

The control objective is to design a feedback control $q(t)$ that drives the reference error $\tilde{T},\ \tilde{s}$ to 0 in the presence of the boundary hysteresis.

5.4.2 The hysteresis inverse

Let $u_d(t)$ be a control signal to be designed. As the inverse of the hysteresis (5.42)-(5.47), define the hysteresis-like characteristic $PI(\cdot)$:

$$q(t) = PI(u_d(t)) = F^{-1}\left(T_\alpha, T_\beta, k_1, k_2, g_1, g_2; T\left(0,t\right)\right)u_d(t), \tag{5.48}$$

where $F^{-1}\left(T\left(0,t\right)\right)$ is defined by:

$$f_H^{-1}(T(0,t)) = \begin{cases} 1 & \text{if } T(0,t) \le T_\alpha, \\ \dfrac{1}{1+k_1(T-T_\alpha)} & \text{if } T_\alpha < T(0,t) \le T_1, \\ \dfrac{1}{1+k_2(T_\beta - T)} & \text{if } T_1 < T(0,t) \le T_\beta, \\ 1 & \text{if } T_\beta \le T(0,t), \end{cases} \tag{5.49}$$

and,

$$f_L^{-1}(T(0,t)) = \begin{cases} 1 & \text{if } T(0,t) \le T_\alpha, \\ \dfrac{1}{1+g_1(T-T_\alpha)} & \text{if } T_\alpha < T(0,t) \le T_1, \\ \dfrac{1}{1+g_2(T_\beta - T)} & \text{if } T_1 < T(0,t) \le T_\beta, \\ 1 & \text{if } T_\beta \le T(0,t), \end{cases} \tag{5.50}$$

The overall expression of $q(t)$ is

$$q(t) = \begin{cases} f_L^{-1}\left(T\left(0,t\right)\right)u_d(t) & \text{if } t \in [t_k^*, t_{k+1}^*) \text{ and } k+1 \text{ odd}, \\ f_H^{-1}\left(T\left(0,t\right)\right)u_d(t) & \text{if } t \in [t_k^*, t_{k+1}^*) \text{ and } k+1 \text{ even}. \end{cases} \tag{5.51}$$

In the actual steel casting process, the hysteresis parameters are unknown, so the exact hysteresis inverse (5.49)-(5.51) is not implementable. Therefore, the following recalibration laws for hysteresis inverse parameters update are proposed. Let $\hat{T}_\alpha, \hat{T}_\beta, \hat{k}_1, \hat{k}_2, \hat{g}_1, \hat{g}_2$ be the estimates of the unknown hysteresis parameters $T_\alpha, T_\beta, k_1, k_2, g_1, g_2$. An estimated hysteresis inverse $\widehat{PI}(\cdot)$ is defined as,

$$q(t) = PI(T(0,t), u_d(t)) = \hat{F}^{-1}\left(\hat{T}_\alpha, \hat{T}_\beta, \hat{k}_1, \hat{k}_2, \hat{g}_1, \hat{g}_2; T\left(0,t\right)\right)u_d(t), \tag{5.52}$$

For the fixed hysteresis estimates $\hat{T}_\alpha, \hat{T}_\beta, \hat{k}_1, \hat{k}_2, \hat{g}_1, \hat{g}_2$ are constants based on a certain prior knowledge (like laboratory experiments). For an adaptive hysteresis, $\hat{\mathrm{T}}_\alpha = \hat{\mathrm{T}}_\alpha(\mathrm{t})$, $\hat{\mathrm{T}}_\beta = \hat{\mathrm{T}}_\beta(\mathrm{t})$, $\hat{\mathrm{k}}_1 = \hat{\mathrm{k}}_1(\mathrm{t})$, $\hat{\mathrm{k}}_2 = \hat{\mathrm{k}}_2(\mathrm{t})$, $\widehat{\mathrm{g}_1} = \widehat{\mathrm{g}_1}(\mathrm{t})$, $\widehat{\mathrm{g}_2} = \widehat{\mathrm{g}_2}(\mathrm{t})$ are time-varying signals generated by an adaptive update law.

Another assumption is made for the hysteresis parameters:

(A5) Positive constants $k_{11}, k_{12}, k_{21}, k_{22}, g_{11}, g_{12}, g_{21}, g_{22}$, and constants $T_{\alpha 1}, T_{\alpha 2}, T_{\beta 1}, T_{\beta 1}$ are known positive constants such that $k_{11} \le k_1 \le k_{12}$, $k_{21} \le k_2 \le k_{22}$, $g_{11} \le g_1 \le g_{12}$, $g_{21} \le g_2 \le g_{22}$, $T_{\alpha 1} \le T_\alpha \le T_{\alpha 2}$, $T_{\beta 1} \le T_\beta \le T_{\beta 1}$.

Even when not stated explicitly, the projection is used to ensure that the estimated hysteresis parameters satisfy the above inequalities. When the hysteresis is present, $q(t)$ is the accessible control which, by our design, is the output of the adaptive hysteresis inverse with the input $u_d(t)$, which is the desired boundary heat flux. A parameterization of the control error $u(t) - u_d(t)$ will help us to develop suitable adaptive laws for updating the estimates $\hat{T}_\alpha(t)$, $\hat{T}_\beta(t)$, $\hat{k}_1(t)$, $\hat{k}_2(t)$, $\widehat{g_1}(t)$, $\widehat{g_2}(t)$ to implement an adaptive hysteresis inverse. $\hat{T}_1(t)$, $\widehat{T_2}(t)$ can be calculated through (5.44).

Define the following indicator functions:

$$\mathcal{X}_1(t)=\begin{cases}1 & \text{if } T(0,t)<T_\alpha \text{ or } T(0,t)>T_\beta,\\ 0 & \text{otherwise.}\end{cases} \tag{5.53}$$

$$\mathcal{X}_{L_1}(t)=\begin{cases}1 & \text{if } T_\alpha<T(0,t)\le T_2,\ t\in[t_k^*,t_{k+1}^*),k+1 \text{ odd},\\ 0 & \text{otherwise.}\end{cases} \tag{5.54}$$

$$\mathcal{X}_{L_2}(t)=\begin{cases}1 & \text{if } T_2<T(0,t)\le T_\beta,\ t\in[t_k^*,t_{k+1}^*),k+1 \text{ odd},\\ 0 & \text{otherwise.}\end{cases} \tag{5.55}$$

$$\mathcal{X}_{H_1}(t)=\begin{cases}1 & \text{if } T_\alpha<T(0,t)\le T_1, t\in[t_k^*,t_{k+1}^*),k+1 \text{ even},\\ 0 & \text{otherwise.}\end{cases} \tag{5.56}$$

$$\mathcal{X}_{H_2}(t)=\begin{cases}1 & \text{if } T_1<T(0,t)\le T_\beta,\ t\in[t_k^*,t_{k+1}^*),k+1 \text{ even},\\ 0 & \text{otherwise.}\end{cases} \tag{5.57}$$

$$\hat{\mathcal{X}}_1(t)=\begin{cases}1 & \text{if } T(0,t)<\hat{T}_\alpha \text{ or } T(0,t)>\hat{T}_\beta,\\ 0 & \text{otherwise.}\end{cases} \tag{5.58}$$

$$\hat{\mathcal{X}}_{L_1}(t)=\begin{cases}1 & \text{if } \hat{T}_\alpha<T(0,t)\le \hat{T}_2, t\in[t_k^*,t_{k+1}^*),k+1 \text{ odd},\\ 0 & \text{otherwise.}\end{cases} \tag{5.59}$$

$$\hat{\mathcal{X}}_{L_2}(t)=\begin{cases}1 & \text{if } \hat{T}_2<T(0,t)\le \hat{T}_\beta, t\in[t_k^*,t_{k+1}^*),k+1 \text{ odd},\\ 0 & \text{otherwise.}\end{cases} \tag{5.60}$$

$$\mathcal{X}_{H_1}(t)=\begin{cases}1 & \text{if } \hat{T}_\alpha<T(0,t)\le \hat{T}_1, t\in[t_k^*,t_{k+1}^*),k+1 \text{ even},\\ 0 & \text{otherwise.}\end{cases} \tag{5.61}$$

$$\mathcal{X}_{H_2}(t)=\begin{cases}1 & \text{if } \hat{T}_1<T(0,t)\le \hat{T}_\beta, t\in[t_k^*,t_{k+1}^*),k+1 \text{ even},\\ 0 & \text{otherwise.}\end{cases} \tag{5.62}$$

In defining these indicator functions, no line segments of the hysteresis loop are repeatedly counted. Therefore, only one of these functions is nonzero at any given time t:

$$\mathcal{X}_1(t)+\mathcal{X}_{L1}(t)+\mathcal{X}_{L2}(t)+\mathcal{X}_{H1}(t)+\mathcal{X}_{H2}(t)=1, \tag{5.63}$$

$$\mathcal{X}_i^2(t)=\mathcal{X}_i(t), \mathcal{X}_i(t)\mathcal{X}_j(t)=0, i\neq j. \tag{5.64}$$

5.4.3 Recalibration design for the full-state feedback control

5.4.3.1 The recalibration law and the control law

When full state is available, the enthalpy $H(t)$ can be calculated. Similarly to (4.9), the following holds:

$$\frac{dH(t)}{dt}=-u(t). \tag{5.65}$$

Let $\Phi(t)=\left(\hat{g}_1(t),\hat{g}_2(t),\hat{k}_1(t),\hat{k}_2(t),\hat{T}_\alpha(t),\hat{T}_\beta(t)\right)$ denote the hysteresis parameter estimation at time t and $\Phi^*=\left(g_1,g_2,k_1,k_2,T_\alpha,T_\beta\right)$. A numerical scheme for implementing the estimated hysteresis inverse is developed next.

At time $t=t_k$, we have the knowledge of the desired boundary heat flux $u_d\left(t_{k-1}\right), u_d(t_k)$ from the control law,

$$u_d(t)=\bar{u}(t)+K(H(t)-\bar{H}(t)),$$

the temperature profile $T(x,t_{k-1})$, boundary location $s(t_{k-1})$, and the estimates of the hysteresis parameters $\Phi\left(t_{k-1}\right)$. The control command $q(t_k)$ can be calculated by (5.75). Then the temperature profile $T(x,t_k)$, and boundary location $s(t_{k-1})$ are available. Although the actual boundary heat flux $u\left(t_{k-1}\right)$is not available for direct measurement, its estimate, $\hat{u}\left(t_{k-1}\right)$,can be derived from the equation

$$\frac{H(t_k)-H(t_{k-1})}{\Delta t}=-\hat{u}(t_{k-1}). \tag{5.66}$$

The relation between $u(t_{k-1})$ and $u_d(t_{k-1})$ is as follows:

$$u(t_{k-1})=\frac{F_{\Phi^*}(T(0,t_{k-1}))}{F_{\Phi(t_{k-1})}(T(0,t_{k-1}))}u_d(t_{k-1}), \tag{5.67}$$

which, combining with (5.66), yields

$$\hat{F}_{\Phi^*}(T(0,t_{k-1}))\approx-\frac{H(t_k)-H(t_{k-1})}{\Delta t}\frac{F_{\Phi(t_{k-1})}(T(0,t_{k-1}))}{u_d(t_{k-1})}. \tag{5.68}$$

Denote $\widehat{\mathrm{X}}(\mathrm{t})=\left(\widehat{\mathrm{X}}_1(\mathrm{t}),\widehat{\mathrm{X}}_{\mathrm{L1}}(\mathrm{t}),\widehat{\mathrm{X}}_{\mathrm{L2}}(\mathrm{t}),\widehat{\mathrm{X}}_{\mathrm{H1}}(\mathrm{t}),\widehat{\mathrm{X}}_{\mathrm{H2}}(\mathrm{t})\right)^{\mathrm{T}}$. $\widehat{\mathrm{X}}(\mathrm{t_{k\text{-}1}})$ is the indicator function estimate at t_{k-1}, and $\widehat{\mathcal{X}}(t_{k-1}|t_k)$ is the re-estimate of the indicator function at t_{k-1} with the measurements at t_k.

Then, (5.68) can be used to update $\Phi(t_k)$ by means of the following adaptive law:

$$\Phi(t_k)=Proj\left[G\left(\hat{F}_{\Phi^*}(T(0,t_{k-1})),\mathcal{X}(t_{k-1}),\mathcal{X}(t_{k-1}\,|\,t_k),T(0,t_{k-1},\Theta(t_{k-1}))\right)\right], \tag{5.69}$$

where $Proj[\cdot]$ is the discrete projection operator used to ensure the boundedness of the parameters according to the assumption (A5). The detailed recalibration operator $G(\cdot)$ is as follows:

$$k_1(t_k)=\begin{cases}\dfrac{\hat{F}_{\Phi^*}(T(0,t_{k-1}))-1}{T(0,t_{k-1})-\hat{T}_\alpha(t_{k-1})}, & \text{if } \mathcal{X}_{H1}(t_{k-1})=1,\mathcal{X}_{H1}(t_{k-1}\,|\,t_k)=1\\ k_1(t_{k-1}), & \text{otherwise}\end{cases} \tag{5.70}$$

$$k_2(t_k)=\begin{cases}\dfrac{\hat{F}_{\Phi^*}(T(0,t_{k-1}))-1}{\hat{T}_\beta(t_{k-1})-T(0,t_{k-1})}, & \text{if } \mathcal{X}_{H2}(t_{k-1})=1,\mathcal{X}_{H2}(t_{k-1}\,|\,t_k)=1\\ k_1(t_{k-1}), & \text{otherwise}\end{cases} \tag{5.71}$$

$$g_1(t_k)=\begin{cases}\dfrac{\hat{F}_{\Phi^*}(T(0,t_{k-1}))-1}{T(0,t_{k-1})-\hat{T}_\alpha(t_{k-1})}, & \text{if } \mathcal{X}_{L1}(t_{k-1})=1, \mathcal{X}_{L1}(t_{k-1}\mid t_k)=1\\ g_1(t_{k-1}), & \text{otherwise}\end{cases} \tag{5.72}$$

$$\hat{T}_\alpha(t_k)=\begin{cases}T(0,t_{k-1}) & \text{if } \mathcal{X}_{H1}(t_{k-1})=1 \text{ or } \mathcal{X}_{L1}(t_{k-1})=1, \mathcal{X}_1(t_{k-1}\mid t_k)=1,\\ T(0,t_{k-1})-\dfrac{\hat{F}_{\Phi^*}(T(0,t_{k-1}))-1}{k_1(t_{k-1})} & \text{if } \mathcal{X}_1(t_{k-1})=1, \mathcal{X}_{H1}(t_{k-1}\mid t_k)=1,\\ T(0,t_{k-1})-\dfrac{\hat{F}_{\Phi^*}(T(0,t_{k-1}))-1}{g_1(t_{k-1})} & \text{if } \mathcal{X}_1(t_{k-1})=1, \mathcal{X}_{L1}(t_{k-1}\mid t_k)=1\\ \hat{T}_\alpha(t_{k-1}) & \text{otherwise}\end{cases} \tag{5.73}$$

$$\hat{T}_\beta(t_k)=\begin{cases}T(0,t_{k-1}) & \text{if } \mathcal{X}_{H2}(t_{k-1})=1 \text{or } \mathcal{X}_{L2}(t_{k-1})=1, \mathcal{X}_1(t_{k-1}\mid t_k)=1,\\ T(0,t_{k-1})+\dfrac{\hat{F}_{\Phi^*}(T(0,t_{k-1}))-1}{k_2(t_{k-1})} & \text{if } \mathcal{X}_1(t_{k-1})=1, \mathcal{X}_{H2}(t_{k-1}\mid t_k)=1,\\ T(0,t_{k-1})+\dfrac{\hat{F}_{\Phi^*}(T(0,t_{k-1}))-1}{g_2(t_{k-1})} & \text{if } \mathcal{X}_1(t_{k-1})=1, \mathcal{X}_{L2}(t_{k-1}\mid t_k)=1\\ \hat{T}_\alpha(t_{k-1}) & \text{otherwise}\end{cases} \tag{5.74}$$

Consider the following control problem. Assume the reference temperature, $\bar{T}(x,t)$, and the reference interface location, $\bar{s}(t)$, are given, which both represent the solution of the Stefan problem with the boundary heat flux, $\bar{u}(t)$, and the initial conditions $\bar{T}_0$, $\bar{s}_0$.

Conjecture 5.1: Suppose the initial conditions satisfy the assumption (A1), and the reference profile satisfies the assumption (A2) and (A3). Then, with the following enthalpy-based full-state feedback control law:

$$q(t)=\hat{F}_{\Phi(t_{k-1})}{}^{-1}\left(\bar{u}(t)+K(H(t)-\bar{H}(t))\right) \tag{5.75}$$

where K is the controller gain, the reference temperature error $\tilde{T}$ converges asymptotically to 0 uniformly over the domain, and the free boundary error $\tilde{s}$ also converges to 0 asymptotically.

The proof is under development, while simulation results confirming the conjecture are provided in the next section.

5.4.3.2 Numerical Simulation

As shown in Figure 35, the true and the initial estimated hysteresis parameters are

$$\Phi^* = \left(0.004, 0.004, 0.0025, 0.0025, 500, 900\right)^T,$$
$$\Phi(t_0) = \left(0.0036, 0.0036, 0.0023, 0.0022, 510, 910\right)^T.$$

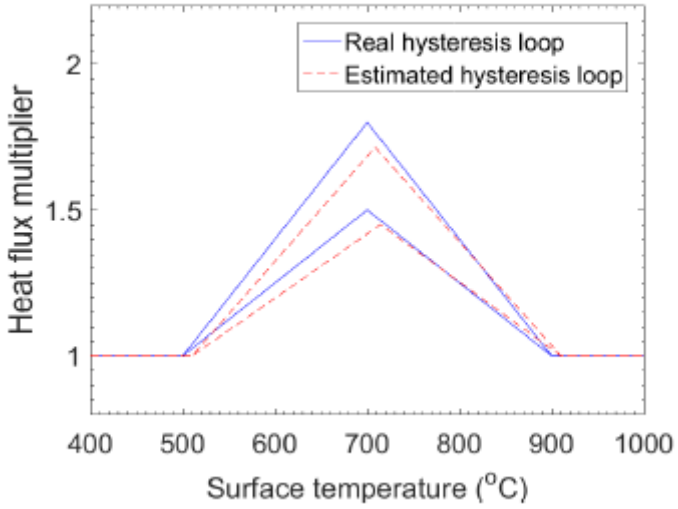

Figure 35. The true and the estimated hysteresis loop.

The upper and the lower bounds of the hysteresis parameters are, respectively,

$$\Phi_{ub} = \left(0.0045, 0.0045, 0.003, 0.003, 520, 920\right)^T,$$
$$\Phi_{lb} = \left(0.0035, 0.0035, 0.002, 0.002, 480, 880\right)^T.$$

The other simulation conditions are the same as in Section 5.3.3. The behavior of the surface temperature reference tracking error $\tilde{T}(0,t)$, the closed-loop response of the moving boundary $s(t)$, and the boundary heat flux error, $u(t) - u_d(t)$, are depicted in Figure 36. The hysteresis model with the recalibration and without it shows similar performance in driving $s(t)$ to $\bar{s}(t)$, as the difference between the initial estimates and the true hysteresis is small. However, for the

surface temperature, hysteresis model with the recalibration ensures that $\tilde{T}(0,t) \to 0$, while the hysteresis model without the recalibration does not provide such a behavior, as shown in Figure 37. Figure 39 shows the control input error $u(t) - u_d(t)$, where it is seen that with the recalibration law $G(\cdot)$, $u(t) - u_d(t) \to 0$. The final hysteresis estimation parameters given by the recalibration law are

$$\Phi = \left(0.004, 0.0039, 0.0025, 0.0025, 500.03, 899.97\right)^T$$

which are very close to the true values.

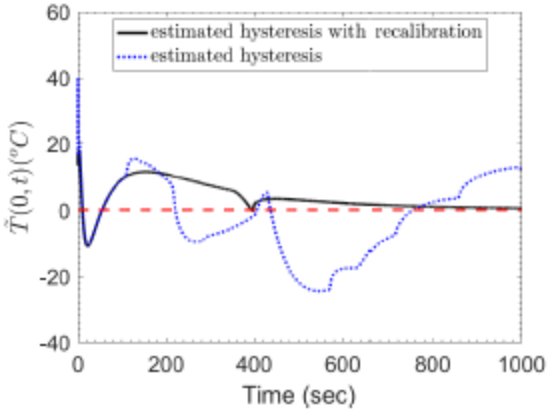

(a) Surface temperature reference error $\tilde{T}(0,t)$

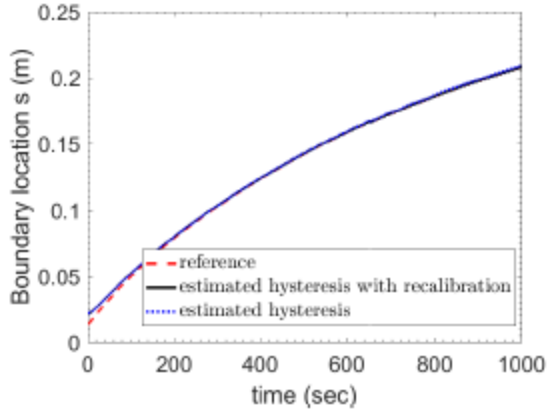

(b) Solidification front

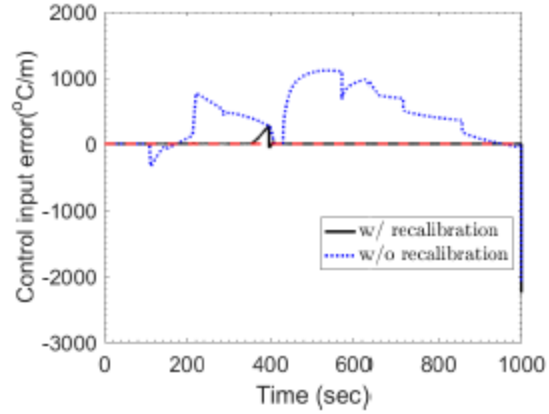

(c) Boundary heat flux error $u(t) - u_d(t)$

Figure 36. Simulation of system (2.24)-(2.27) with the initial condition mismatch.

5.4.4 Recalibration design for output feedback control

5.4.4.1 Observer Design

The proposed observer design is a modified version of (5.16)-(5.20) from Section 5.3: denote the estimate of the temperature by $\hat{T}(x,t)$, and the estimate of the solidification front by $\hat{s}(t)$. Consider the following estimator:

$$\hat{T}_t(x,t) = a\hat{T}_{xx}(x,t),\ 0 \le x \le s(t) \tag{5.76}$$

$$\hat{T}(\hat{s}(t),t) = T_f, \tag{5.77}$$

$$\hat{T}_x(0,t) = u_d(t), \tag{5.78}$$

$$\hat{T}(x,0) = \hat{T}_0(x),\ \hat{s}(0) = \hat{s}_0 > 0 \tag{5.79}$$

$$\dot{\hat{s}}(t) = -b\left(\hat{T}_x\left(\hat{s}(t)^+\right) - \hat{T}_x\left(\hat{s}(t)^-\right)\right) + l\left(\hat{T}(0,t) - T(0,t)\right), \tag{5.80}$$

where the initial conditions satisfy assumption (A1) and the estimation gain $l > 0$. The major difference lies in equation (5.78). As the exact hysteresis function in (5.18) is not available, the estimated hysteresis function is used and simplified to equation (5.78).

5.4.4.2 Recalibration law and control law

Following the same derivation as in Section 5.4.3.1, and replacing $H(t)$ with $\hat{H}(t)$, yields

$$\hat{F}_{\Phi^*}(T(0,t_{k-1})) \approx -\frac{\hat{H}(t_k) - \hat{H}(t_{k-1})}{\Delta t}\frac{\hat{F}_{\Phi(t_{k-1})}(\hat{T}(0,t_{k-1}))}{u_d(t_{k-1})}. \tag{5.81}$$

And recalibration law (5.70)-(5.74) can be used to update the hysteresis parameters. The same control problem as in Section 5.4.3.1 is considered

Conjecture 5.2: Suppose the initial conditions satisfy assumption (A1), the reference profile satisfies assumption (A2) and (A3). Then with the following enthalpy-based full-state feedback control law:

$$q(t) = \hat{F}_{\Phi(t_{k-1})}^{-1}\left(\bar{u}(t) + K(\hat{H}(t) - \bar{H}(t))\right) \tag{5.82}$$

where K is the controller gain. Then the reference temperature error $\tilde{T}$ and estimation error $\hat{T} - T$ converges asymptotically to 0 uniformly over the domain, the free boundary error $\tilde{s}$ and estimation error $\hat{s} - s$ also converges to 0 asymptotically.

The proof is under development while simulation results are provided in the next section.

5.4.4.3 Numerical simulation

The same simulation parameters as in Section 5.4.3.2 are used in this section.

The behavior of the surface temperature reference tracking error $\tilde{T}(0,t)$, the closed-loop response of the moving boundary $s(t)$, and the boundary heat flux error, $u(t) - u_d(t)$, are depicted in Figure 36. However, for the surface temperature, the hysteresis model with the recalibration ensures that $\tilde{T}(x,t) \to 0$. The control input error $u(t) - u_d(t) \to 0$, as well. The final hysteresis estimation parameters given by the recalibration law are

$$\Phi = \left(0.0039, 0.0039, 0.0025, 0.0025, 500.02, 900.29\right)^T$$

which are very close to the true values.

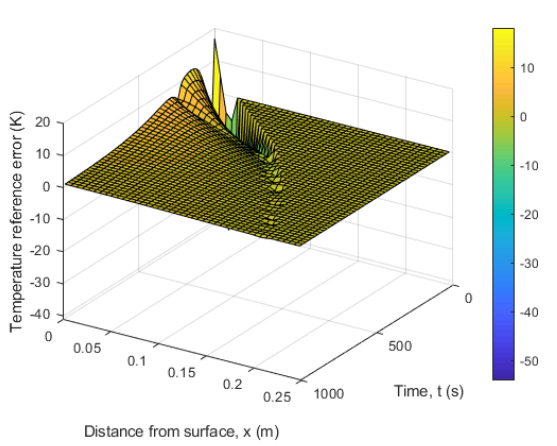

(a) The temperature reference error $\tilde{T}(x,t)$

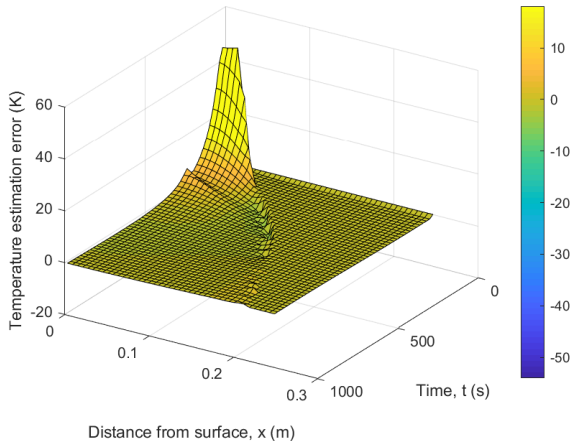

(b) The temperature estimation error $\hat{T}(x,t)-T(x,t)$

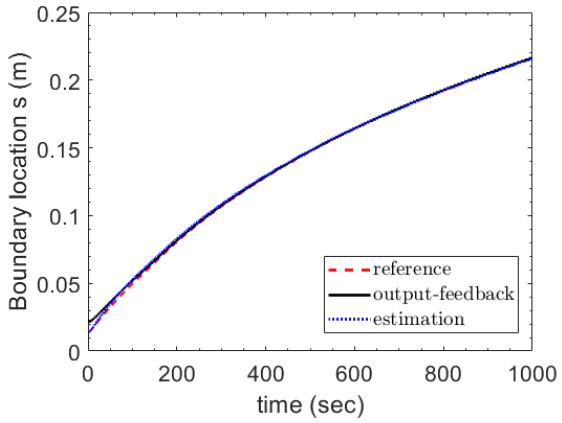

(c) The solidification front $s(t)$

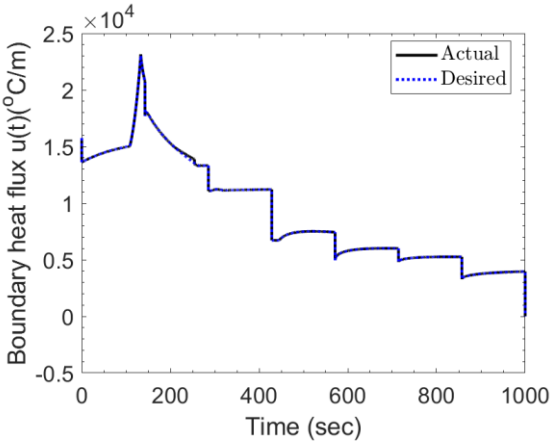

(d) boundary heat flux

Figure 37. Simulation results of output feedback control with recalibration of unknow hysteresis.

5.5 Summary

The control of the Stefan problem with the boundary hysteresis depending on the temperature due to the water boiling effect is discussed in this chapter. The enthalpy-based full-state feedback control law and the output feedback control law discussed in the previous chapter are extended to the Stefan problem with hysteresis via a hysteresis compensator. One weakness of the proposed control law discussed in Sections 5.2 and 5.3 lies in the assumption (A4) that the continuous hysteresis characteristics can be determined based on the lab experiments. However, the actual hysteresis characteristics may be different from the ones obtained through the lab measurements.

A recalibration law to update the hysteresis estimation based on the available measurements is proposed for the hysteresis model constructed in terms of the line segments. Extension of the results presented to an arbitrary hysteresis loop instead of a simple four-line-segments-model could be addressed in the future research.

CHAPTER 6.

OPTIMAL CONTROL FOR METALLURGICAL LENGTH MAINTENANCE

The control laws derived in the previous chapter all require a known reference temperature $\bar{T}(x,t)$ and solidification front position $\bar{s}(t)$, that are the solutions to (2.24)-(2.27) under the known reference control input $\bar{u}(t)$ with the initial conditions $\bar{T}(x,0)=\bar{T}_0$ and $\bar{s}(0)=\bar{s}_0$ satisfying the assumptions (A1) and (A2). This chapter presents one method of obtaining these reference states through optimization [12], [39], [50].

The control laws used in the steel industry generally provide a trade-off between the avoidance of the surface and the internal cracks and the enforcement of the desired metallurgical length. However, in the situation of the sudden speed increase, the metallurgical length maintenance becomes more critical than the crack avoidance due to the possibility of a whale phenomenon, the dangerous bursting of the not fully solidified strand outside of the containment zone. Therefore, this chapter puts an emphasis on the latter problem, while neglecting the temperature control. This leads to a different control objective - that of minimizing the time and the size of the deviation of the metallurgical length from the desired value. In order to solve this problem, an open-loop minimum time-optimal control problem needs to be formulated under hard constraints on deviation of the metallurgical length from the desired value.

The problem was heuristically addressed through simulation for a sudden speed drop [39] and a sudden speed increase [12]. Subsequently, [50] considered the same problem as in [12]: minimizing the ML deviation during a sudden, *and more dangerous due to the possibility of the molten steel escape,* casting speed increase. [50] provided the state-unconstrained non-minimum

time optimal control law derivation for the minimization of the deviation of the metallurgical length from the desired value. This chapter presents the results.

6.1 Single-slice Optimization Problem

6.1.1 Problem formulation

Denote z-axis as the casting direction, where $z=0$ and z_{end} represent, respectively, the meniscus and the end of the caster. ML is determined by the shell thickness profile along the caster, $s(z)$; therefore, the goal of minimizing the ML deviation can be recast into minimizing the deviation of the shell thickness profile from the reference one, $\bar{s}(z)$. By taking the Lagrangian reference frame, the simulation domain of the equations (2.24)-(2.27) moves in the casting direction at the casting speed, $v_c(t)$. Therefore, assuming the domain starts at the meniscus at time $t=0$, the reference $\bar{s}(z), 0<z<z_{end}$ can be transferred to the time domain, $\bar{s}(t), 0<t<t_f$, by

$$z(t)=\int_0^t v_c(\tau)d\tau, z_{end}=\int_0^{t_f} v_c(\tau)d\tau. \tag{6.1}$$

Even if the reference shell thickness profile along the z-axis, $\bar{s}(z)$, stays the same, the corresponding reference in time, $\bar{s}(t)$, may be different for different casting speed profiles. In the present work, the case of a sudden casting speed increase is considered: a slice starts at the meniscus at $t=0$, with the casting speed v_{c1}, and at $t=t^*$, the casting speed increases to v_{c2}. Let $s_1(t)$ and $s_2(t)$ denote, respectively, the shell thickness profiles of the slice and the reference. At the time of casting speed change, the slice resides at the location

$$z^*=v_{c1}t^* \tag{6.2}$$

and the total residence time remaining for this slice in the caster is

$$t_{f1} = t^* + \frac{z_{end} - v_{c1} t^*}{v_{c2}}. \tag{6.3}$$

Notice that under the settings of the present work, the shell thickness profile, $\bar{s}(z)$, is the one at the casting speed of v_{c1}. Therefore, $s_1(t) = \bar{s}(t)$ for $t \in (0, t^*)$. Then to minimize the metallurgical length deviation, we want to minimize the difference between $s(t)$ and $\bar{s}(t)$ for the remaining travel time of this slice before it reaches the end of caster.

Define a new time coordinate t' by taking a time shift of t^*, i.e. $t' = t - t^*$. Then $s_1(t')$ and $\bar{s}(t')$ is defined on $t' \in (-t^*, t_f)$, where $t_f = t_{f1} - t^*$ is the residence time of the slice being subjected to the optimal control after the speed increase.

Now, introduce the functional,

$$J_u(s) = \int_0^{t_f} (s(t') - \bar{s}(t'))^2 dt', \tag{6.4}$$

and consider the following control set:

$$U_{ad} = \{u \in L_\infty[0, t_f], M_1 \le u(t') \le M_2\}. \tag{6.5}$$

For simplicity, denote $J_u(s)$ as $J(u)$. Then, the optimal control problem can be stated as:

Problem (I) Find $u^o(t') \in U_{ad}$ such that

$$J(u^o) = \min_{u \in U_{ad}} J(u). \tag{6.6}$$

The time coordinate t' incorporates the moment of speed increase as t'=0. For the ease of notation, in the remaining part of this paper, the prime superscript is omitted, so that t is used in place of t'.

6.1.2 Existence of optimal controls

The existence and uniqueness of solution to the above single-phase Stefan problem under bang-bang control has been proven [12]. Here the proof of the existence of optimal solution to Problem (I) is given.

Theorem 6.1. There exists an optimal control $u^* \in U_{ad}$ that solves Problem (I).

Proof. Obviously J is bounded below, and there exists a minimizing sequence of J over U_{ad}. Let $u_n \in U_{ad}$ be a minimizing sequence over $J(u)$. Since U_{ad} is weakly compact in L_p, there exists a convergent subsequence u_n and u^* such that,

$$u_n \to u^* \text{ weakly in } L_p - \text{sense.}$$

Due to the uniqueness and existence of solution to (2.24)-(2.27), denote $s_n(t)$, $s^*(t)$ to be the corresponding solutions.

From Lemma 2.2, we have

$$| s_{u_n}(t) - s_{u^*}(t) | \le Cb \int_0^t | u_n(\tau) - u^*(\tau) | \, d\tau. \tag{6.7}$$

Therefore,

$$(s_n(t) - s^*(t))^2 \le C^2 b^2 (\int_0^t | u_n(\tau) - u^*(\tau) | \, d\tau)^2 \le C^2 b^2 (\int_0^t (u_n(\tau) - u^*(\tau))^2 \, d\tau. \tag{6.8}$$

Integrate from t to t_f on both sides,

$$\begin{aligned}\int_0^{t_f}\left(s_n(t)-s^*(t)\right)^2 dt &\le C^2b^2\int_0^{t_f}\int_0^t\left(u_n(\tau)-u^*(\tau)\right)^2 d\tau dt\\ &\le C^2b^2t_f\max_{0\le t\le t_f}\left(\int_0^t\left(u_n(\tau)-u^*(\tau)\right)^2 d\tau\right)\\ &\le C^2b^2t_f\int_0^{t_f}\left(u_n(\tau)-u^*(\tau)\right)^2 d\tau.\end{aligned} \tag{6.9}$$

Therefore,

$$s_n(t)\to s^*(t)\text{ weakly in }L_p-\text{sense,}$$

and thus $J_{u_n}(s)\to J_{u^*}(s)$ and u^* is a minimizer. □

6.1.3 Derivation of the optimality system

In this section, we derive the first-order necessary optimality condition for the minimization problem using the Lagrange approach. The following Lagrange functional is used:

$$L=\int_0^{t_f}(s-\bar{s})^2dx-\int_0^{t_f}\int_{s(t)}(T_t-aT_{xx})pdxdt-\int_0^{t_f}(T_x(0)-u)gdt-\int_0^{t_f}(\dot{s}-bT_x(s(t)))hdt. \tag{6.10}$$

The functions $p(x,t)$, $g(t)$, and $h(t)$ denote the Lagrange multipliers associated with (2.24) -(2.27). The first order necessary optimality condition for the optimization problem now is given by:

$$\nabla L=0,$$

and the adjoint equation system for our problem is defined through

$$L_T\tilde{T}=0\ \text{ and }\ L_s\tilde{s}=0,$$

for all feasible directions $\tilde{T}$ and $\tilde{s}$. L_T and L_s here denote the directional derivatives of L with respect to T and s, respectively.

The directive derivative of L with respect to T takes the form:

$$L_T\tilde{T} = -\int_0^{t_f}\int_0^{s(t)}(\tilde{T}_t - a\tilde{T}_{xx})pdxdt - \int_0^{t_f}\tilde{T}_x(0)gdt + \int_0^{t_f} b\tilde{T}_x(s(t))hdt. \tag{6.11}$$

Integrating by parts with respect to time and space yields,

$$\begin{aligned} L_T T = &-\int_0^{s(t_f)} T(t_f)\,p(t_f)dx + \int_0^{s_0} T(0)\,p(0)dx + \int_0^{t_f}\int_0^{s(t)} T\,p_t dxdt \\ &+ \int_0^{t_f} \dot{s}(t)T(s(t))\,p(s(t))dt + \int_0^{t_f} aT_x(s(t))\,p(s(t))dt \\ &- \int_0^{t_f} aT_x(0)\,p(0)dt - \int_0^{t_f} aT(s(t))\,p_x(s(t))dt + \int_0^{t_f} aT(0)\,p_x(0)dt \\ &+ \int_0^{t_f}\int_0^{s(t)} aT\,p_{xx}dxdt - \int_0^{t_f} T_x(0)gdt + \int_0^{t_f} b\widetilde{T_x(s(t))}\text{hdt}. \end{aligned} \tag{6.12}$$

Sorting the terms in (6.12) corresponding to their domains of integration, and using $\tilde{T}(x,0)$ (since $T(x,0) = T_0$ is required explicitly) yields

$$\begin{aligned} 0 = &-\int_0^{s(t_f)} T(t_f)\,p(t_f)dx + \int_0^{t_f} aT(0)\,p_x(0)dt \\ &+ \int_0^{t_f}\int_0^{s(t)} (p_t + ap_{xx})Tdxdt + \int_0^{t_f} (\dot{s}(t)\,p(s(t))dt \\ &- ap_x(s(t)))T(s(t))dt + \int_0^{t_f} (ap(s(t)) + bh)T_x(s(t))dt \\ &- \int_0^{t_f} (ap(0) + g)T_x(0)dt. \end{aligned} \tag{6.13}$$

Therefore, the adjoint system for the temperature takes the form:

$$p(x,t_f) = 0, x \in (0, s(t_f)), \tag{6.14}$$

$$p_x(0,t) = 0, t \in (0,t_f), \tag{6.15}$$

$$h(t) = -\frac{a}{b}\,p(s(t),t), t \in (0,t_f), \tag{6.16}$$

$$g(t) = -ap(0,t), t \in (0,t_f), \tag{6.17}$$

$$p_t(x,t) + ap_{xx}(x,t) = 0, x \in (0, s(t_f)), t \in (0,t_f) \tag{6.18}$$

$$\dot{s}(t)\,p(s(t),t) = ap_x(s(t),t), t \in (0,t_f) \tag{6.19}$$

Next, reassembling the Lagrange function by integration by parts (similarly to $L_T\tilde{T}$), and substituting the already known parts of the adjoint equation system obtained above yields

$$L = \int_0^{t_f} (s-\bar{s})^2 dt + \int_0^{s_0} \tilde{T}(0)\, p(0) dx + \int_0^{t_f} ugdt - \int_0^{t_f} \dot{s}hdt.$$

The directional derivative with respect to s is equal to

$$L_s\tilde{s} = \int_0^{t_f} 2(s-\bar{s})\tilde{s}dt - \int_0^{t_f} \dot{\tilde{s}}hdt.$$

Integration by parts yields

$$L_s\tilde{s} = \int_0^{t_f} 2(s-\bar{s}+\frac{1}{2}h_t)\tilde{s}dt + \tilde{s}(t_f)h(t_f) - \tilde{s}(0)h(0). \tag{6.20}$$

Using $\tilde{s}(0) = 0$ (since $s(0) = \bar{s}(0)$) and $h(t_f) = 0$ (which follows from (6.14) and (6.16)), the adjoint system for solidification front is given by

$$s(t) - \bar{s}(t) + \frac{1}{2}h_t(t) = 0 \tag{6.21}$$

Now, with the adjoint system (6.14)-(6.21), the only missing ingredient of the desired optimality system is $L_u\tilde{u}$. Differentiating (6.10) with regard to u yields:

$$L_u\tilde{u} = \int_0^{t_f} \tilde{u}gdt. \tag{6.22}$$

(6.22) is the first order necessary optimally condition when the control u is unconstrained. In our case, for $u \in U_{ad}$, the optimality condition is replaced by a variational inequality (Chapter 3 of [53]), which has the form:

$$L_u(v-u) = \int_0^{t_f} g(t)(v-u)dt \geq 0, \tag{6.23}$$

for all boundary functions v satisfying $M_1 \leq v \leq M_2$.

In summary, the optimality system of Problem (I) in the absence of control and state constraints is given by:

- the forward system (2.24)-(2.27)
- the adjoint system (6.14)-(6.19)
- the gradient equation (6.21)

6.2 Multi-slice Optimization Problem

The above optimization problem considers only a single slice of steel in the caster, and the boundary flux u can be chosen to best suit that particular slice's reference shell thickness. In commercial casters, the spray region is usually subdivided into several aggregated spray zones, each linking a group of spray nozzles together. Therefore, any slice inside the spray zone will be subject to the same boundary flux. Each spray zone may have a different feasibility region, U_{ad}, since $M_1,\ M_2$ can be different based on the caster settings. The optimal control problem described in Section 21 is for one spray zone, rather than for the entire caster. The results are extended next from a single-slice/single-spray-zone setting to a multi-slice/single-spray-zone one.

6.2.1 Control problem formulation

Let $s_0^i, T_0^i, z_i, \overline{s}_i, t_f^i, i = 1, 2, ..., N$ be the initial shell thickness, the initial temperature, the location at which speed increases, the reference shell thickness, and the residence time, respectively. If $z_1 > z_2 > \ldots > z_N$, then $t_{f1} < t_{f2} < ... < t_{fN}$.

Define the cost function:

$$J_N(u) = \sum_1^N \int_0^{t_{fi}} (s_i(\tau) - \bar{s}_i(\tau))^2 \, d\tau,$$

under the following control set:

$$U_N = \{u \in L_\infty[0, t_{fN}], M_1 \le u(t) \le M_2\}.$$

Problem (II) Find $u^* \in U_N$ such that

$$J_N(u^*) = \min_{u \in U_N} J_N(u). \tag{6.24}$$

Theorem 6.2. There exists an optimal control $u^* \in U_N$ that solves Problem (II).

Proof. The proof is similar to that of Theorem 6.1. □

6.2.2 Derivation of the optimality system

In this section we will derive the optimality system for *N* slices. The following Lagrange functional is used:

$$\begin{aligned} L = & \sum_{i=1}^N \int_0^{t_{fi}} (s_i - \bar{s}_i)^2 - \sum_{i=1}^N \int_0^{t_{fi}} \int_{s_i(t)} (T_{it} - aT_{ixx}) \, p_i \\ & - \sum_{i=1}^N \int_0^{t_{fi}} (T_{ix}(0) - u) g_i - \sum_{i=1}^N \int_0^{t_{fi}} (\dot{s}_i - bT_{ix}(s_i(t))) h_i. \end{aligned} \tag{6.25}$$

The functions $p_i(x,t), q_i(t), h_i(t), i = 1, 2, ..., N$ denote the Lagrange multipliers associated to (24)–(27). The adjoint equation system for our problem is defined through

$$L_{T_i} \tilde{T}_i = 0 \text{ and } L_{s_i} \tilde{s}_i = 0, i = 1, 2, ..., N.$$

Following the same procedure as in Subsection 6.1.3 yields the following adjoint system for each slice i:

$$p_i\left(x,t_{fi}\right)=0, x\in\left(0,s_i\left(t_{fi}\right)\right), \tag{6.26}$$

$$p_{ix}\left(0,t\right)=0, t\in\left(0,t_{fi}\right), \tag{6.27}$$

$$h_i\left(t\right)=-\frac{a}{b}\,p_i\left(s_i\left(t\right),t\right), t\in\left(0,t_{fi}\right), \tag{6.28}$$

$$g_i\left(t\right)=-ap_i\left(0,t\right), t\in\left(0,t_{fi}\right), \tag{6.29}$$

$$p_{it}\left(x,t\right)+ap_{ixx}\left(x,t\right)=0, \left(0,s_i\left(t_{fi}\right)\right)\times\left(0,t_{fi}\right), \tag{6.30}$$

$$\dot{s}_i\left(t\right)p_i\left(s_i\left(t\right),t\right)=ap_{ix}\left(s_i\left(t\right),t\right), t\in\left(0,t_{fi}\right), \tag{6.31}$$

$$h_{it}\left(t\right)=-2\left(s_i\left(t\right)-\overline{s}_i\left(t\right)\right), t\in\left(0,t_{fi}\right). \tag{6.32}$$

The gradient for the control is given by:

$$L_u\tilde{u}=\int_0^{t_{f1}}\sum_{i=1}^{N}g_i\tilde{u}+\sum_{i=1}^{N}\int_{t_{fi}}^{t_{fi+1}}\sum_{i+1}^{N}g_i\tilde{u}, \tag{6.33}$$

yielding

$$J'(u)=\begin{cases}-\sum_{i=1}^{N}g_i & 0\le t<t_{f1},\\ -\sum_{k=i}^{N}g_k & t_{fi}\le t\le t_{fi+1},\\ -g_N & t_{fN-1}\le t\le t_{f_N}.\end{cases} \tag{6.34}$$

Now, with the adjoint system, the procedure described in Section 6.1.3 can be used to solve the minimization problem.

6.3 Numerical Approach

This section illustrates numerical approach to solving the single-slice optimization problem, with the same procedure being applicable to the multi-slice optimization problem. The procedure used combines the explicit finite difference with the variable space grid (VSG) [63]. The number of space intervals between a fixed boundary $x = 0$ and a moving boundary $x = s(t)$ was kept constant and equal to N_x, so that the moving boundary always lie on the N^{th} grid. The grid at the time instance t is defined by

$$x_{i,j} = i\Delta x_j, \Delta x_j = \frac{s(t_j)}{N_x}, 0 \le i \le N_x. \tag{6.35}$$

For the time discretization,

$$\tau = \frac{t_f}{N_t}, t_j = j\tau, j = 0,..., N_t,$$

with $\hat{T}_{i,j}$ being the discrete temperature $\hat{T}_{i,j} \approx T(x_i(t_j), t_j)$, $\hat{s}_j$- the discrete free boundary $\hat{s}_j \approx s(t_j)$, $\hat{p}_{i,j} \approx \hat{p}_2(x_i(t_j), t_j)$- the discrete adjoint temperature, and $\hat{g}_j \approx \hat{g}(t_j), \hat{h}_j \approx \hat{h}_(t_j)$ – the adjoint boundary condition. The discrete versions of the other variables are also denoted with a hat.

In the presence of the point-wise control constraints U_{ad}, the gradient method is used (Algorithm 1). This is a popular approach to solution of constrained optimization problems and we refer the reader to [64]–[66] for an analysis of its convergence properties.

Algorithm 1: Adjoint-Based Projected Gradient Method

Input: u^0

Output: $\hat{u}, \hat{T}, \hat{s}, \hat{p}, \hat{q}, \hat{h}$

1. Initialize: $i = 0$.

while $1 \le k \le k_{max}$ **do:**

2. Solve the forward problem (24)-(27) for $\hat{T}^k$ and $\hat{s}^k$.
3. Solve the adjoint problem (199)-(206) for $\hat{p}^k, \hat{q}^k, \hat{h}^k$.
4. Construct the descent direction from (208): $v^k = -\hat{q}^k$.
5. Determine δ^k from:
$$\delta^k := \min_\delta J(P_{[M_1,M_2]}(u^k + \delta v^k)).$$
6. Set $u^{k+1} = P_{[M_1,M_2]}(u^k + \delta^k v^k), k \to k+1.$

In order to ensure that the computed controls $\hat{u} \in U$, the projection $P_{[M_1,M_2]}(u)$ is introduced and defined as:

$$P_{[M_1,M_2]}(u) = \min\{M_2, \max\{M_1, u\}\}. \tag{6.36}$$

Suitable stopping criteria for Algorithm 1 are

$$k_{max} := \min\left\{k : \frac{\hat{J}^{k-1} - \hat{J}^k}{\hat{J}^0} \le \epsilon_J\right\},$$

and/or

$$k_{max} = \min\{k : |\hat{u}^{k+1} - \hat{u}^k| \le \epsilon_u\}.$$

1) Forward step *k*

Following the same procedure as in [63], (2.24)-(2.27) can be recast into the following discretized version for $j = 0, 1, 2, ..., N_x - 1$:

$$\hat{T}^k_{0,j+1} = (1 - \frac{2a\tau}{\Delta x_j^2})\hat{T}^k_{0,j} + \frac{2a\tau}{\Delta x_j^2}\hat{T}^k_{1,j} - \frac{2a\tau}{\Delta x_j}u^k_j, \tag{6.37}$$

$$\hat{T}_{i,j+1}^{k} = \hat{T}_{i,j}^{k} + \frac{\tau}{2\Delta x_j}\frac{x_{i,j}\dot{\hat{s}}_j}{\hat{s}_j}(\hat{T}_{i+1,j}^{k} - \hat{T}_{i-1,j}^{k}) + \frac{a\tau}{\Delta x_j^2}(\hat{T}_{i+1,j}^{k} - 2\hat{T}_{i,j}^{k} + \hat{T}_{i-1,j}^{k}), 1 \le i \le N_x - 1, \quad (6.38)$$

$$\hat{T}_{N_x,j}^{k} = T_f, \quad (6.39)$$

$$\hat{s}_{j+1}^{k} = \hat{s}_j^{k} + \frac{b\tau}{2\Delta x_j}(3\hat{T}_{N_x,j}^{k} - 4\hat{T}_{N_x-1,j}^{k} + \hat{T}_{N_x-2,j}^{k}) \quad (6.40)$$

Then the algorithm for the forward step can be described as in Algorithm 2:

Algorithm 2: Forward step k
1. Initialize at t=0: $\hat{s}_0^k = s_0, \hat{T}_{i,0}^k = T_0(x_{i,j})$.
while $1 \le j \le N_t - 1$ **do:**
2. Compute the temperature $\hat{T}_{i,j}^k$ through (221)-(224).
3. Compute the free boundary $\hat{s}_{j+1}^k$ through (225).
4. Compute the new grid $x_{i,j+1}$ through (219).
end

2) Backward step *k*

The backward problem uses the same grid $x_{i,j}$ that is used in the forward problem. Similarly, we have the following discretized version of the adjoint system:

$$\hat{h}_{j-1}^{k} = \hat{h}_j^{k} + 2\tau(\hat{s}_j^{k} - \bar{s}_j), \quad (6.41)$$

$$\hat{p}_{N_x,j-1}^{k} = -\frac{b}{a}\hat{h}_{j-1}^{k}, \quad (6.42)$$

$$\hat{p}_{0,j-1}^{k} = (1 - \frac{2a\tau}{\Delta x_j^2})\hat{p}_{0,j}^{k} + \frac{2a\tau}{\Delta x_j^2}\hat{p}_{1,j}, \quad (6.43)$$

$$\hat{p}_{i,j-1}^{k} = \hat{p}_{i,j}^{k} - \frac{\tau}{2\Delta x_j}\frac{x_{i,j}\dot{\hat{s}}_j}{\hat{s}_j}(\hat{p}_{i+1,j}^{k} - \hat{p}_{i-1,j}^{k}) + \frac{a\tau}{\Delta x_j^2}(\hat{p}_{i+1,j}^{k} - 2\hat{p}_{i,j}^{k} + \hat{p}_{i-1,j}^{k}), 1 \le i \le N_x - 1. \quad (6.44)$$

Then the algorithm for the backward step can be described as in Algorithm 3:

Algorithm 3: Backward step k
1. Initialize at $t=t_f$: $\hat{p}^k_{i,N_t}=0, \hat{h}^k_{N_t}=0$.
while $1\le j\le N_t-1$ **do:**
2. Set the boundary conditions $\hat{p}^k_{N_x,j}$ and $\hat{p}^k_{N_x,j}$ by (226) - (228).
3. Compute $\hat{p}^k_{i,j}$ by (229).

3) Computation of the gradient

The choice of the descent direction v^k in step 4 of Algorithm 1 corresponds to the negative gradient, i.e., the direction of the steepest descent.

4) Line minimization

Determining the step size δ_k in step 5 of Algorithm 1 is too complicated a task to be solved exactly. Instead, the backtracking line search algorithm with Armijo condition (Chapter 3 of [67]) is used to determine an approximation to δ^k. Detailed algorithm is as follows:

Algorithm 4: Line minimization step k
1. Choose $\alpha_0>0, c_1, c_2\in(0,1)$; set $\alpha\leftarrow\alpha_0$
while $J\left(P_{[M_1,M_2]}(u^k+\delta v^k)\right)>J\left(u^k\right)+c_1\alpha\left(v^k\right)^T v^k$ **do:**
2. $\alpha\leftarrow c_2\alpha$

The numerical results will be provided in Section 6.4.

6.4 Numerical Results

The following simulations use the parameters given in Table 3. The simulation code based on VGS grid was verified against an analytical solution to the Stefan problem with Dirichlet boundary

condition from [44]. Unless otherwise noted, $N_x = 20$ and $\tau = 5 \times 10^{-4}$. The simulated zone length is $z_{end} = 1.75$m, and the speed increase is from $v_{c1} = 1.5$ m/min to $v_{c2} = 1.75$m/min. The control constraints are$M_1 = 0.5 \times 10^4$K/s, $M_2 = 4.0 \times 10^4$K/s.

Table 3. Thermodynamic Properties Used in Simulations

Symbol	Description	Value
k	Thermal conductivity	30 W/m·K
ρ	Density	7400 kg/m^3
c_p	Specific heat	670 J/kg·K
L_f	Latent heat of fusion	272 kJ/kg
T_f	Melting temperature	1811 K
L	Half thickness of strand	0.1 m

The spatial grid contains 21 points, and the temporal grid contains 10001 grid points, i.e. $N_x = 20$, and$N_t = 10000, \tau = 6 \times 10^{-3}$s. The stopping criteria are chosen as $\epsilon_J = 1 \times 10^{-8}$ m and $\epsilon_u = 1 \times 10^{-2}$ K/s. The parameter chosen for the line search is $\alpha = 1000, c_1 = 0.01, c_2 = 0.5$.

6.4.1 Single-slice optimization

The initial shell thickness is $s_0 = 0.01$ m, the initial temperature T_0 is chosen to be linear with $T_0(s_0) = T_f, T_0(0) = 1473$K , the dwell time after speed increase is $t_f = z_{end} / v_{c2} = 60$ sec, i.e. we optimize the solidification process over the time period [0, t_f]. This means that the number of optimization variables is approximately 2×10^5 for the chosen mesh grid. The reference shell thickness is the one with the casting speed v_{c1} and the initial control command $u(t) = 2.5\times10^4$ K/s.

The computational time for one forward step takes approximately 8.1 sec on Intel Xeon 3.4 GHz CPU with 8G RAM, for the backward step it takes 8.3 sec and the average computation time

for one line minimization step is 6.7 sec. The optimization procedure is terminated after 1790 iteration with approximately 11 hours. The iteration history is shown in Figure 38.

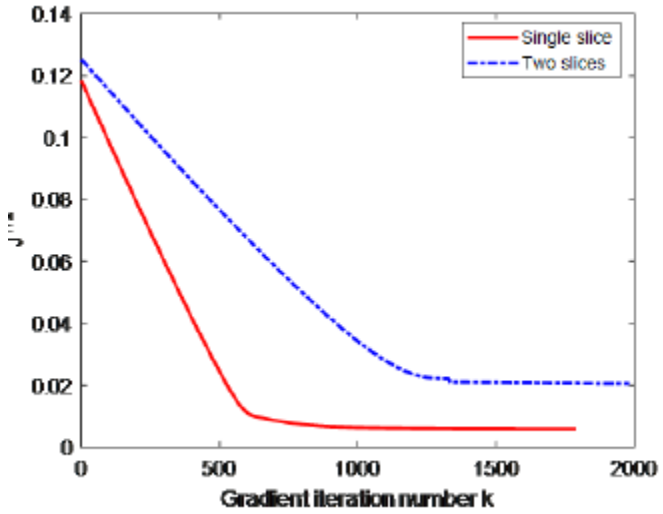

Figure 38. Iteration history of $J^{0.5}$.

After the speed increase, with the initial control $u(t)$, the cost value is $J(u) = 14.062\ mm^2$; with the optimal control u^* shown in Figure 39(b), the cost goes down two orders of magnitude to $J(u^*) = 3.41 \times 10^{-2}$ mm^2. Figure 39(a) shows that the shell thickness under u^* matches the reference closely.

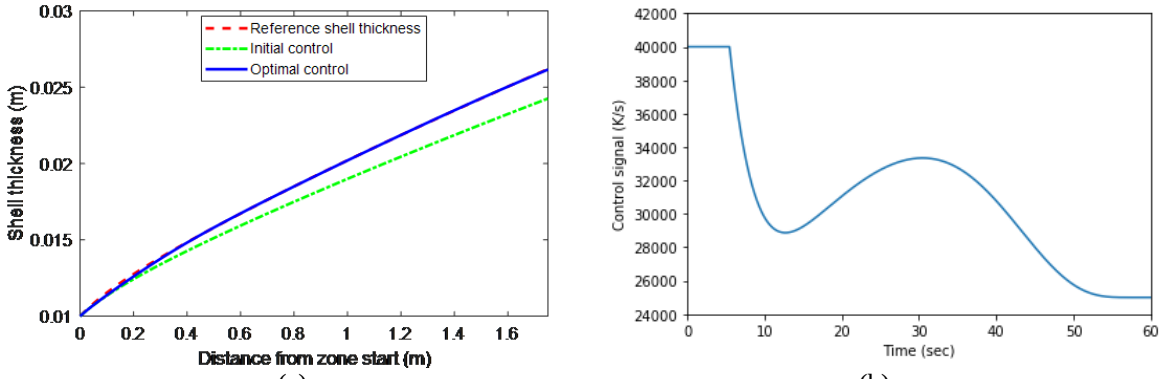

(a) (b)

Figure 39. Simulation result for the single slice optimization problem: (a) shell thickness profile under initial control and optimal control; (b) optimal control signal for the single-slice optimization.

6.4.2 Two-slice optimization

In this section, we use $N = 2$ to illustrate the method proposed in Section 6.2. When speed increases, the 1^{st} slice is in the middle of the spray zone with $t_{f1} = 30$ sec, the 2^{nd} slice is at the beginning of the spray zone with $t_{f2} = 60$s. Therefore, the control $u(t)$ controls both slices for $0 \leq t \leq 30$s, and controls only the 2^{nd} slice for $30 < t \leq 60$s. This means that the number of optimization variables is approximately 3×10^5.

The computational time for one forward step takes approximately 9.4 sec, for the backward step - 9.6 sec, and the average computation time for one line minimization step is 16.4 sec. The optimization procedure is terminated after 1980 iterations taking approximately 19 hours. The iteration history is shown in Figure 41.

With the initial control $u(t) = 2.5 \times 10^4$ K/s, $J(u) = 15.673$ mm^2; with the optimal control u^* shown in Figure 40(b), $J(u^*) = 0.42$ mm^2. Figure 40(a) shows the shell thickness profile along the casting direction z. The results show that the 2^{nd} slice has almost identical shell thickness as the reference, while the 1^{st} slice's shell thickness slightly differs from the reference.

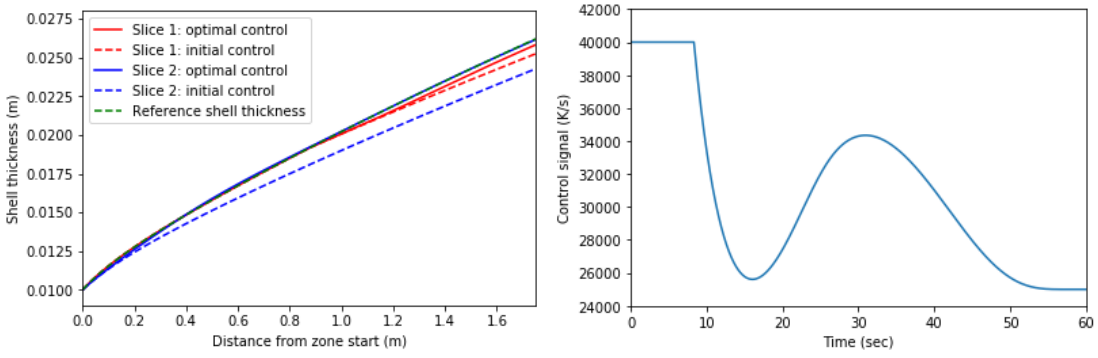

(a) (b)

Figure 40. Simulation result of for the single slice optimization problem: (a) shell thickness profile under initial and optimal control for slice 1 and slice 2; (b) optimal control signal for the two-slice optimization.

6.5 Summary

The optimal control signal, shown in Figure 40(a), increases to maximum immediately after the speed increase to maximize the shell growth (this matches the finding in [12], [39]). The results also show that better control is attained over the 2^{nd} slice than the 1^{st} one. This difference takes place because at the moment of the speed increase, the 2^{nd} slice is at the beginning of the spray zone, allowing for more time to control its shell growth under the input constraints.

The state-of-the-art on-line model of the continuous casting process, CONOFFLINE model, introduced in Section 3.3 and used in a commercial caster for several years [4], simulates 200 slices evenly spaced along a 15 m long caster. Even though the calculation time may be reduced by switching to GPU, reducing temporal grid points, and increasing stopping criteria, it may still not be feasible to use this procedure for real-time control.

However, this approach can be used to determine the optimal control strategy for casting speed change scenarios of interests. Then the control methods proposed in Chapter 4 and Chapter 5 can be used to ensure the convergence of the actual control signal, the shell thickness, and the temperature profile to the references.

CHAPTER 7.

INVESTIGATING THE CENTERLINE BRIDGING WITH CONOFFLINE

Bridging refers to the phenomenon where the dendritic solidification fronts growing from opposite sides of the strand wide faces meet at some location upstream of the final metallurgical length, and thereby isolate a liquid pocket downstream. This pocket is surrounded by solid steel on all sides, so its shrinkage cannot be fed by the molten steel pool when it solidifies. Thus, the isolated liquid pocket solidifies like the center of a cast ingot, which usually results in high segregation, shrinkage cavities, porosity, and other centerline defects. Indeed, this slab-casting phenomenon is sometimes referred to as "mini-ingotism" [9]. Bridging has been shown to increase the centerline segregation, because the latter can be created by suction of the alloy-rich liquid steel between the dendrites around the bridging region, due to the solidification shrinkage of the isolated liquid pocket [68]. One type of bridging is the periodic bridging, a phenomenon thought to result from the periodic buildup of the internal equiaxed grains settling down onto the outer radius of the strand's liquid core [69]. However, in this study, a mechanism for the non-periodic bridging is investigated.

The author's paper coauthored with undergraduate research student, William Drennan and the author's advisors [70] identifies an important new mechanism for the formation of the centerline bridging, due to the sudden drops in the casting speed, under the spray table control within both thin and thick steel slab casters. Such sudden speed drops commonly accompany sticker-breakout alarms. The dynamic solidification heat-transfer model of the continuous casting process, ConOffline, is used to investigate this phenomenon. This chapter first presents an example of bridging during a speed drop under the spray table control, and proposes a new mechanism for

bridging. Then, the parametric studies are performed to investigate this new bridging phenomenon using the ConOffline model.

7.1 The Centerline Bridging

Using ConOffline, numerical simulation were performed to investigate centerline bridging in a typical commercial caster. This section provides a detailed example.

7.1.1 A centreline bridging example

Simulations here are based on a thin (90 mm-thick) slab caster at Nucor Steel in Decatur, Alabama. The steel grade simulated is low (0.05 wt-%) Carbon steel, with the properties given in Table 4. The first case considered is a sudden speed slow-down from 3.5 m/min to 0.5 m/min, with spray water flow rates changed suddenly at the time of the casting speed drop, according to the spray table given in Figure 41. The heat flux in the mold depends on many complicated phenomena. In this work, the average mold heat flux was taken as a function of the casting speed, based on an empirical correlation for a thin slab caster developed previously [43],

$$\bar{q}_{\mathrm{m}}\left[\mathrm{MW/m^2}\right] = 1.197\left(v_{\mathrm{c}}\left[\mathrm{m/min}\right]\right)^{0.544}. \tag{7.1}$$

For the heat flux in the secondary cooling region, Nozaki's empirical correlation [46] was used for the spray cooling regions.

Table 4. Steel Properties Used in Simulations

Steep Property	**Value**
Liquidus temperature	1532.1 ^{o}C
Solidus temperature	1515.3 ^{o}C
Pouring temperature	1550 ^{o}C

Latent heat of fusion	271 kJ/kg

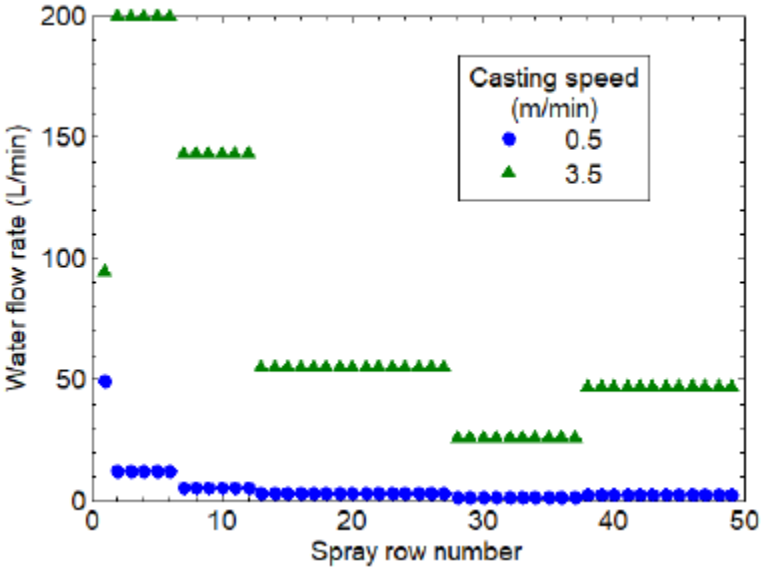

Figure 41. Portion of "spray-table" showing the spray water flow rates used at two casting speeds of interest.

The evolution of the metallurgical length with time during the sudden speed drop is shown in Figure 42. The metallurgical length gets shorter, with decreasing rate after t = 0 when the speed change begins. At 180 s, there is a sudden drop in the metallurgical length. This drop is due to the centerline bridging of the liquid core, which is illustrated in the snapshots of the shell thickness profile down the strand in Figure 43. At 60 seconds after the speed drop, the shell thickness no longer increases continuously with the distance from the meniscus. The shell at approximately 1.5 m from the meniscus is thinner than both upstream and downstream. This thin spot persists and moves downward with the moving strand. By 187 seconds after the speed drop, the steel is fully solid around 2.17 m, when the two thick spots upstream of the thin spot touch. At the thin spots, there is still liquid further on down the caster. After enough time passes, the liquid in the thin spots solidifies as well, and a final, continuously-increasing profile is reached at 208 seconds after the speed drop, which is the new steady-state profile.

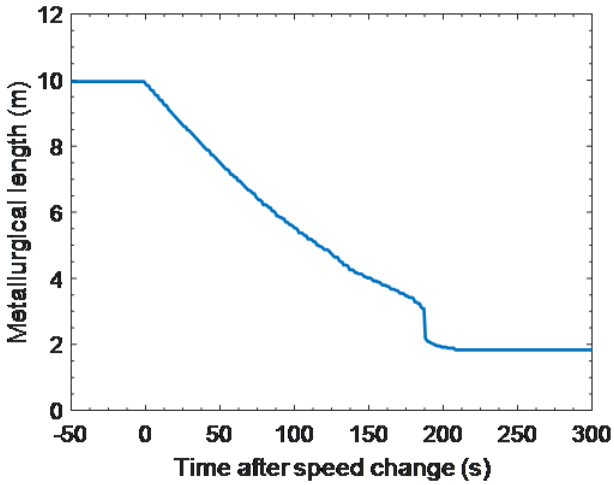

Figure 42. Metallurgical length during a sudden speed drop from 3.5 to 0.5 m/min under the spray table control.

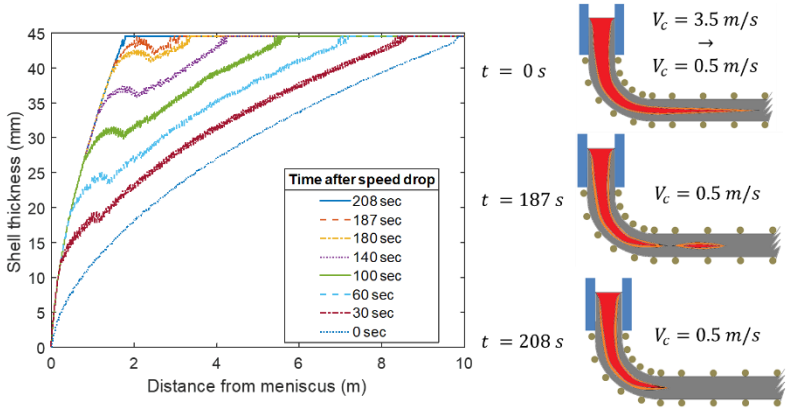

Figure 43. The shell thickness history during a sudden speed drop from 3.5 to 0.5 m/min under the spray table control.

7.1.2 Steps in the bridging mechanism

As shown in Figure 43, a thin spot is observed to develop approximately 1.5 m from the meniscus at 60 seconds after the speed drop. This thin spot persists as solidification proceeds and moves downstream, and it eventually entraps liquid and results in the centerline segregation defects in the final product.

At the time of the speed drop, the spray-water flow rate in each secondary cooling zone drops immediately from the flow rate at 3.0 m/min to that at 0.5 m/min, according to Figure 41. The heat flux in the mold also drops according to (7.1). The drop in the surface cooling just below the mold

is relatively more severe than the heat flux drop near the mold exit. This produces a thin spot in the shell just below the mold exit just after the speed drop, and a corresponding thick spot just above that region that solidifies a thicker shell than both upstream and downstream locations, denoted as slice *i* in Figure 44. The thick spot moves with the strand through the secondary cooling, eventually meeting its other half, and entrapping the liquid pocket just below. Eventually, the liquid pocket solidifies, and shrinks, leaving behind a region of the centerline segregation and the shrinkage cavities just below the bridged region of the strand.

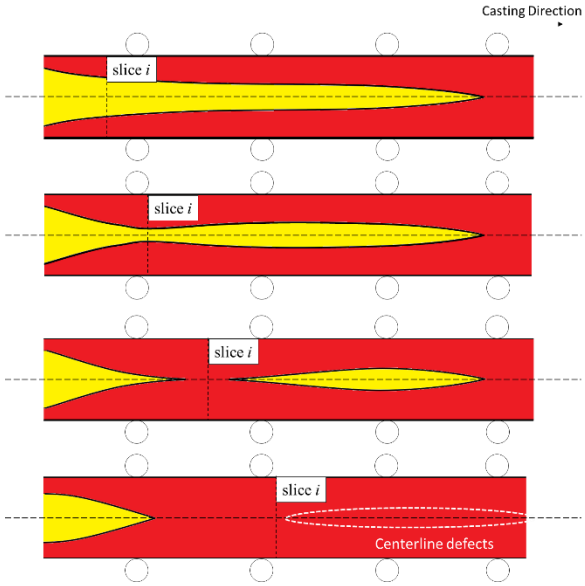

Figure 44. Illustration of the steps in the centerline bridging after a sudden casting speed drop.

7.2 Parametric Studies

In this section, a series of speed drops are simulated with models of a 90 mm caster [47] inspired by the Nucor, Decatur thin slab caster, and a 220 mm caster [39]. In each test, at time $t = 0$, the speed dropped suddenly from v_{c0} and v_{cf}, and the spray water flow rates dropped from Q_0 to Q_f. Different tests varied the speed drop, and the initial casting speed. The initial water

flow rates Q_0 were taken from the caster-specific spray tables for the initial casting speed given in Figure 41 for the 90mm caster. In most tests, the final water flow rates were also taken from the caster specific spray tables, but in several tests, these final flow rates were modified.

7.2.1 Effect of the speed drop size

Results for the 90 mm caster are given in Figure 45, showing the area of the trapped liquid pocket. Figure 45(a) indicates that for a given initial casting speed, the area of the liquid pocket entrapped by bridging decreases with the extent of the speed drop. Also, for a given speed drop, increasing the initial casting speed causes a decrease in the area of the liquid pocket. This second trend is seen better by replotting the results according to the final casting speed, as shown in Figure 45(b), which shows that the liquid pocket area decreases with the increasing final casting speed. In summary, the centerline bridging is more severe with the larger sudden speed drops, especially when the speeds are low.

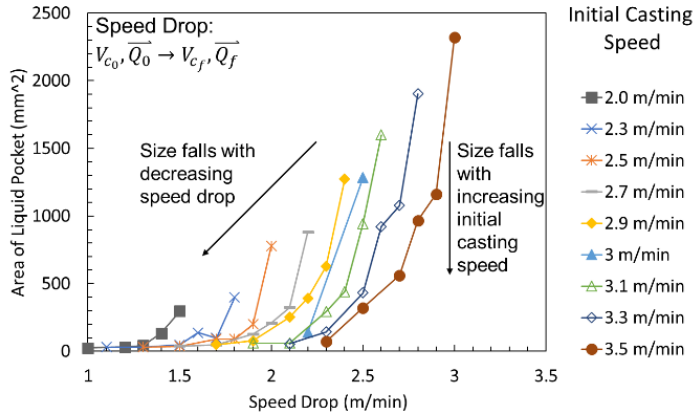

(a) Cases grouped according to initial casting speed

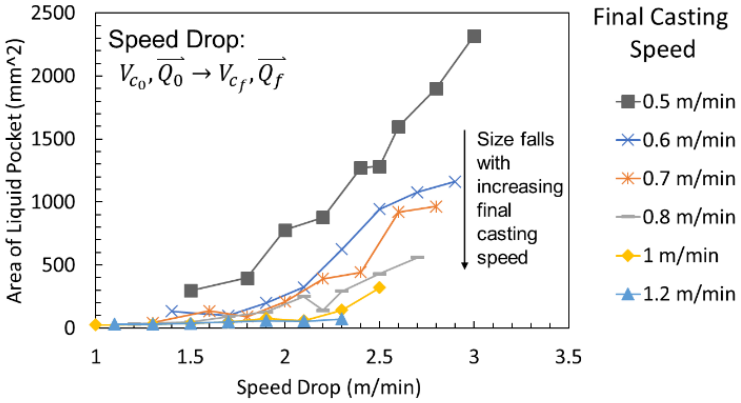

(b) Cases grouped according to final casting speed

Figure 45. Effect of the casting speed drop on the area of the entrapped liquid pocket (90 mm thick caster).

7.2.2 Effect of the strand thickness

To investigate the effect of the strand thickness on this centerline bridging phenomenon, similar tests were conducted for a 220 mm thick-slab caster. Details of the caster and the spray table are given in [39]. Sample results are shown in Figure 46, which shows similar trends as in Figure 45: the area of the liquid pocket increases with the extent of the speed drop, and with smaller initial and final casting speeds.

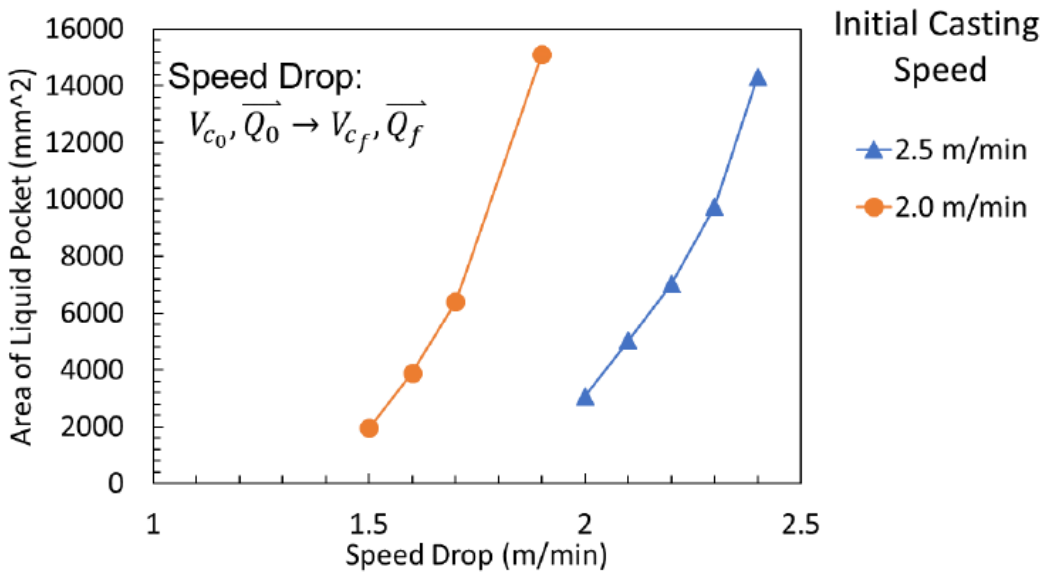

Figure 46. Effect of the strand thickness on the area of the entrapped liquid pocket.

Comparing the results in Figure 45 and Figure 46 for the same casting speed conditions (the speed drop, the initial and the final casting speeds), the entrapped liquid pockets are about ten times larger with the 220 mm caster than with the 90 mm caster. Although each caster has its own spray water zones and spray table, it appears that the bridging mechanism due to the casting speed slowdowns causes more severe centerline defects in the thicker slab casters.

7.2.3 Effect of incrementally dropping speed

Considering the drastic increase in the size of the liquid pocket with the increasing speed drop, it seemed logical that a more gradual speed drop would lessen the bridging problem. To investigate this idea, two simulations of incremental speed drops were performed for the 90 mm (thin) slab caster. Results are shown in Figure 47.

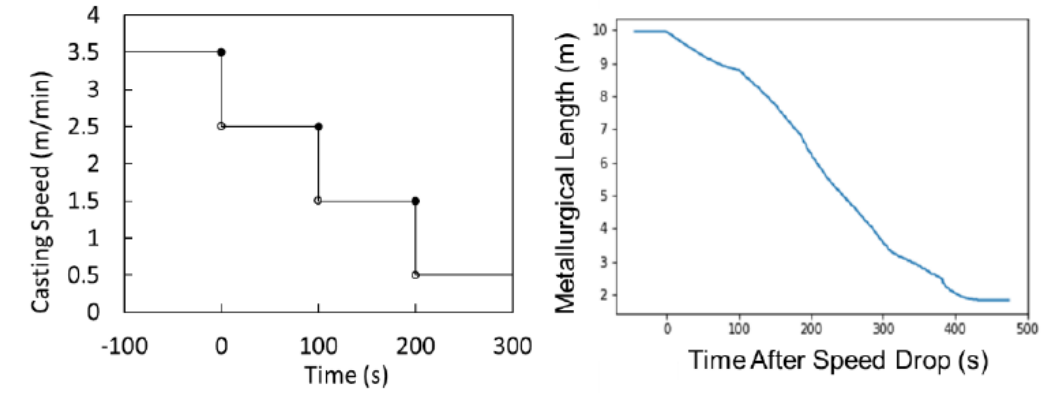

(a) Casting speed drops of 1 m/min every 100s from 3.5 m/min to 0.5 m/min

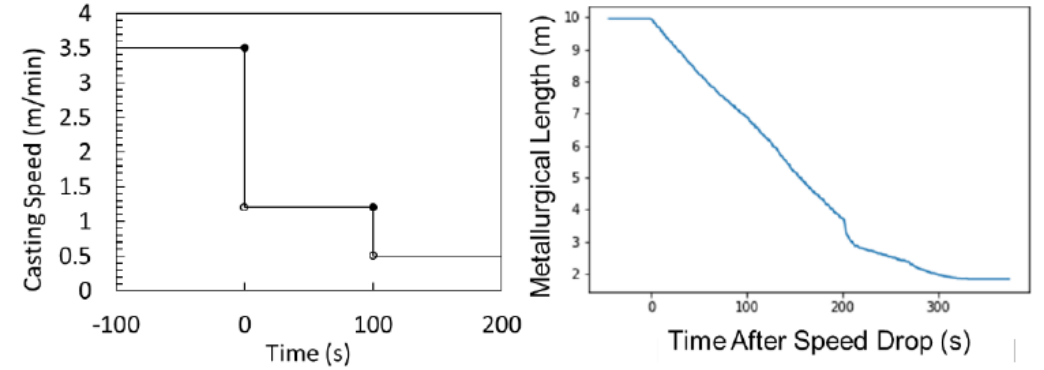

(b) Casting speed drops from 3.5 to 1.2 m/min and to 0.5 m/min after 100s

Figure 47. Simulation results for the incremental speed drops (220 mm thick caster with the spray table control).

The first simulation involved dropping speed from 3.5 to 0.5 m/min via speed drops of 1 m/min every 100s. This case was chosen because no bridging was observed for speed drops of this size in the previous tests (see Figure 45). As hoped, bridging was completely eliminated, as indicated by the lack of the vertical drops in Figure 47. This finding is significant, considering that the bridging experienced with the single speed drop from 3.5 to 0.5 m/min produced the worst bridging of all the cases in this caster, with an entrapped liquid pocket area of 2300 mm^2.

Considering this success, this same speed drop scenario was repeated using only two speed-drop increments. The first drop was chosen to be greater, from 3.5 m/min to 1.2 m/min, knowing from the results in Figure 45 that the drops at the higher speeds produce a less severe bridging.

The second-step speed drop (from 1.2 to 0.5 m/min) of only 0.7 m/min, was expected to decrease the bridging severity. The results, given in Figure 47, show no bridging, although the crook at around 100 seconds confirms that bridging almost occurred, so this is a borderline case. These results confirm that dropping speed more gradually, such as using a few steps, permits avoiding the bridging phenomenon uncovered in this work. Further work is needed to optimize the speed drops for different casters.

7.2.4 The effect of a steel alloy

To investigate the effect of the steel alloy composition on the bridging phenomenon, further simulations were conducted to compare two different steel grades: the low carbon steel (0.05wt % C), and the higher alloy steel (0.4 % C, 1.1 % Mn). The results in Figure 48 for the 90-mm thick caster show that the entrapped liquid pockets for the alloy steel are about twice as large and much deeper than that for the low carbon steel under the same casting speed and the spray-water conditions. This confirms expectations that higher alloying leads to more severe centerline segregation problems from bridging.

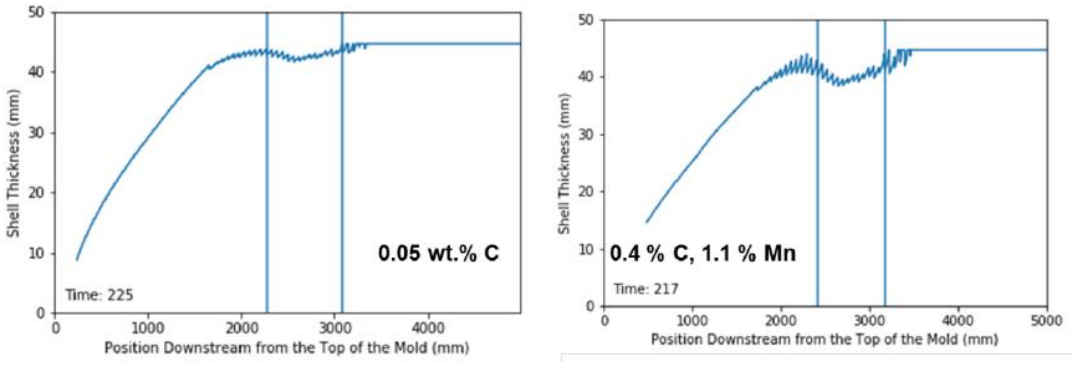

Figure 48. The shell thickness profiles down the caster at the time of the maximum bridging (speed drop from 3.5 to 0.5 m/min).

7.2.5 Effect of the spray cooling control

In this section, the effect of the spray cooling control methods on the creation of the centerline bridging are presented and analyzed.

7.2.5.1 Spray table control

For the spray table control, the spray flow rates in spray zones, or spray patterns, that produce good quality steel are determined by experience, the plant trial and error, and the steady state modeling. A higher casting speed requires the higher water flow rates to maintain the same cooling conditions. These spray patterns depend on the steel grade, the production dimension, the casting speed, and the machine design. During the continuous casting process, if the casting speed changes, plant operators or an automatic level 2 control system will instantly change the spray water flow rates according to the spray patterns defined in the table for that speed.

A typical spray table is shown in Table 5, where $Q_{sw}^{i}\left(v_{cj}\right)$ represents the spray flow rate of a spray zone i at a casting speed v_{cj}. For an arbitrary casting speed v_c, define v_c^{upper} as the minimum casting speed v_{cj} in the spray table that is bigger than v_c, and v_c^{lower} as the maximum casting speed in spray table that is smaller than v_c. For the current casting speed $v_c(t)$, ConOffline searches through the casting speeds v_{cj} in the spray table to find the corresponding v_c^{lower} and v_c^{upper}. Then, the spray flow rate of the spray zone i at the casting speed v_c can be calculated by the following equation:

$$Q_{sw}^{i}(v_c) = Q_{sw}^{i}(v_c^{lower})\frac{v_c^{upper} - v_c}{v_c^{upper} - v_c^{lower}} + Q_{sw}^{i}(v_c^{upper})\frac{v_c - v_c^{lower}}{v_c^{upper} - v_c^{lower}}. \quad (7.2)$$

Table 5. Generalized spray table

Spray zone	Q_{sw} at v_{c1}	Q_{sw} at v_{c2}	Q_{sw} at v_{c3}	…
1	$Q_{sw}^{1}(v_{c1})$	$Q_{sw}^{1}(v_{c2})$.	$Q_{sw}^{1}(v_{c3})$	…
2	$Q_{sw}^{2}(v_{c1})$	$Q_{sw}^{2}(v_{c2})$	$Q_{sw}^{2}(v_{c3})$	…
3	$Q_{sw}^{3}(v_{c1})$	$Q_{sw}^{3}(v_{c2})$	$Q_{sw}^{3}(v_{c3})$	…
4	$Q_{sw}^{4}(v_{c1})$	$Q_{sw}^{4}(v_{c2})$	$Q_{sw}^{4}(v_{c3})$	…
…	…	…	….	…

7.2.5.2 The time-constant control

The spray table control method simply gives the different flow rates for a different casting speed. The sudden speed changes will lead to the sudden flow rate changes; This will result in the sudden fluctuations of the surface temperature, which is not good for the steel surface quality. Therefore, a classic type of a control algorithm, which is often called "dynamic spray cooling", has been developed and widely used in the steel industry to improve on a simple spray table control. One of them is the "time-constant control" introduced in the author's paper author's paper coauthored with the author's advisors and Akitoshi Matsui, a researcher at JFE Steel, who supplied the plant data [39], which combines the spray table cooling velocity and cooling with time concepts together through an empirical mixture constant. With the time-constant control, the average casting speed is used to get flow rates from the spray table. Even with the sudden speed change, the average casting speed of steel also changes gradually.

Consider the following general case: at wall-clock time $t = 0$, the caster starts casting and the steel is casting at a time-varying casting speed $v_c(t)$, z being an arbitrary location in the caster. The dwell time $\tau(z,t)$ is defined as the time it takes for the steel to travel from the meniscus to the location z at time t, and it can be found by solving the inverse of the following equation:

$$z = \int_{t-\tau(z,t)}^{t} v_c(s)ds. \tag{7.3}$$

Then the average casting speed for the steel to move from the meniscus to the location z at time t from the start up of the casting process can be calculated:

$$\overline{v_c}(z,t) = \frac{z}{\tau(z,t)}. \tag{7.4}$$

In the continuous casting process, one spray zone usually can have only one spray flow rate, so instead of the average casting speed $\bar{v}_c(z,t)$ for the location z, the average casting speed $\overline{v}_{ci}(t)$ for the spray zone i at time$t$ needs to be calculated. Then $\overline{v}_{ci}(t)$ can be substituted into the equation (7.2) as v_c to get the spray flow rate for the spray zone i.

In the time-constant control method, the following equation is used to calculate $\overline{v}_{ci}(t)$:

$$\overline{v}_{ci}(t) = \frac{z_{mid}(i)}{\tau(z_{end}(i),t)}, \tag{7.5}$$

where, $\tau(z_{end}(i),t)$ is the solution to the inverse of equation (233), $z_{end}(i)$ is the distance from the meniscus to the end of the spray zone i and $z_{mid}(i)$ is the distance from the meniscus to the middle of the spray zone i.

Then the spray flow rate for the spray zone i is given by:

$$Q_{sw}^{i}(t) = Q_{sw}^{i}(\overline{v_{ci}(t)}) = Q_{sw}^{i}(v_c^{lower})\frac{v_c^{upper} - \overline{v_{ci}}}{v_c^{upper} - v_c^{lower}} + Q_{sw}^{i}(v_c^{upper})\frac{\overline{v_{ci}} - v_c^{lower}}{v_c^{upper} - v_c^{lower}}. \tag{7.6}$$

7.2.5.3 PI control

An important feature of the caster spray configuration is that the rows of the individual spray nozzles are grouped into N_{zone} spray zones according to the nozzle location and control the authority (which depends on how the nozzles are connected through the headers and the pipes to a given valve). Each individual spray zone corresponds to an area in which the spray water to the

nozzles has a single inlet valve. This means that all the rows of the nozzles in a zone have the same spray-water flow rate and the spray density profile.

ConOffline system has a PI controller for the surface temperature built-in. First, the plant operators will decide the desired temperature, T_{set}^{i} (or the reference input temperature) for each spray zone, then the reference temperature is compared with the measured average surface temperature in each zone, T_i (or the measured output), to get the measured error $e_i(t)$.

$$e_i(t) = T_{set}^{i} - T_i(t). \tag{7.7}$$

The control signal $u_i(t)$ is then determined based on the measured temperature error:

$$u_i(t) = k_i^P e_i(t) + k_i^I \int_0^t e_i(s)ds + u_i(0), \tag{7.8}$$

where k_i^P and k_i^I are called the P-controller gain and the I-controller gain, $u_i(0)$ are the initial control signals at $t = 0$. In the case of the speed drop, since the caster operates at a constant casting speed before the speed drop, $u_i(0)$ is the control signal before the speed drop. The temperature setpoints for the different spray zones are chosen to be the steady state average surface temperature values under the spray at 3.5 m/min provided in Figure 41 and listed in Table 6.

Table 6. Fixed temperature setpoints for PI control method

Zone	**Setpoints °C**	k^P	k^i
1	1122.909	0.2	0.2
2	1057.4	2	0.5
3	1007.85	1.2	0.3
4	1009.73	0.5	0.2
5	1029.88	2.5	0.25
6	1049.61	2.5	0.25
7	1012.52	1.5	0.2

The initial control signal of a spray zone i before the speed change is the flow rate at the initial casting speed of 3.5 m/min, $Q_{sw}^{i}(0)$. Therefore, under the PI control, the spray flow rate of a spray zone i can be calculated as:

$$Q_{sw}^{i}(t) = k_i^P \Delta T_i(t) + k_i^I \int_0^t \Delta T_i(s)ds + Q_{sw}^{i}(0), \tag{7.9}$$

where

$$\Delta T_i = \frac{\int_{zonei} \left(T(z,t) - T_{set}^{i}\right)}{Li}, \tag{7.10}$$

with L_i being the total length of zone i. Since CONCONTROLLER updates the control commands every Δt seconds, the spray flow rate of a spray zone i is:

$$Q_{sw}^{i}(t+\Delta t) = u_i^P(t+\Delta t) + u_i^I(t+\Delta t), \tag{7.11}$$

where the proportional (u_i^P) and the integral (u_i^I) components are defined as follows:

$$u_i^P(t+\Delta t) = k_i^P \Delta T_i(t), \tag{7.12}$$

$$u_i^I(t+\Delta t) = u_i^I(t) + k_i^I \Delta T_i(t)\Delta t. \tag{7.13}$$

Because of the physical limitations of the spray cooling system at the caster, it is possible that the spray flow rate requested by the PI control signal $u_i(t)$ is infeasible, yielding the actual flow rate different than the requested one. Even when the requested flow rate is feasible, the requested and the actual flow rates $u_i'(t)$ also may be different because of the dynamics such as the actuator interactions with the header piping system. For the simulations in this study, no actual plant is involved, so the requested and the actual flow rates always match when the requested flow rates is feasible. The differences between the requested and the actual flow rates tend to cause controller instability, known as "windup". Therefore, a classic anti-windup is adopted to avoid the integrator windup:

$$u_i^I(t+\Delta t) = u_i^I(t) + k_i^I \Delta T_i(t)\Delta t + k_i^{aw}(u'_i(t) - u_i(t)) \tag{7.14}$$

where k_i^{aw} are the tuning parameters that can be used to relax the rate of windup. Here, all k_i^{aw} are set to 1.

The P-controller gain k_i^P, the I-controller gain k_i^I, and temperature setpoints used in the simulation are listed in Table 6. The P gains are tuned based on the total flow rates change at the two steady states; a bigger P gain is used for the zones with a larger flow rate change. The I gains are tuned based on the P gain value. The PI controller's performance vitally depends on the choice of the PI controller gains, yielding a good performance for a good gains choice.

7.2.5.4 The performance comparison

The sudden speed drop of 3.5 m/min to 0.5 m/min is considered as it is the most severe speed drop and there is the centerline bridging under the spray table control. Figure 49 shows the metallurgical length profiles produced by all three control methods. As the figure shows, there are no sudden changes of the metallurgical length under the time-constant control and the PI control, indicating that there is no bridging phenomenon present.

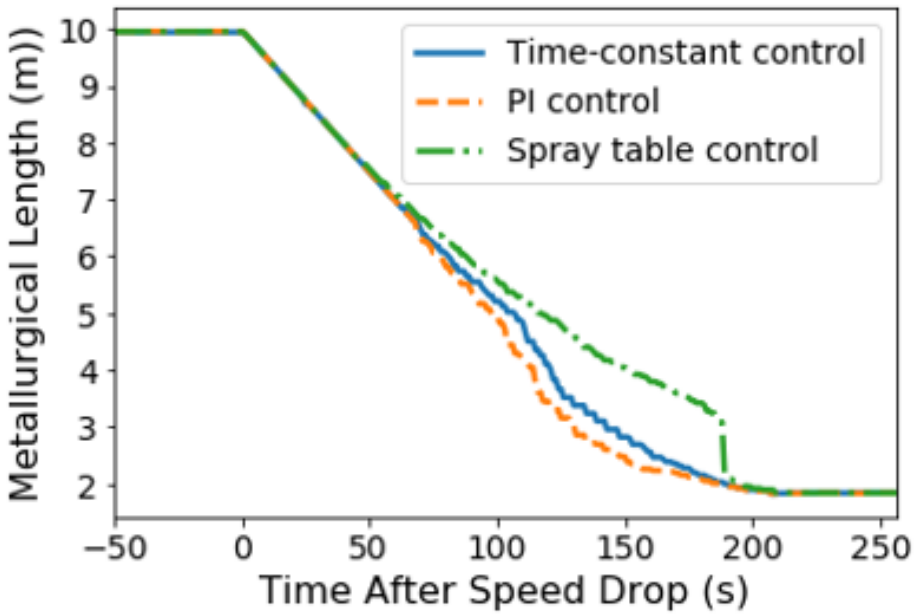

Figure 49. The metallurgical length profiles under the control methods considered.

7.3 Summary

This study shows that the centerline bridging, which leads to the centerline segregation and the porosity defects, may occur after a sudden drop in the casting speed. This is due to a thick spot in the solidifying steel shell forming high in the caster just after the speed drop. The size of the resulting entrapped liquid pocket can be reduced by decreasing the extent of the speed drop, by increasing the initial and the final casting speeds, and by decreasing the alloy content. Two strategies to avoid this problem are recommended. First: avoid the sudden large speed drops to the low casting speeds, opting instead for an incremental or a continuous decrease in the casting speed. Second, avoid large drops in the spray water flow rates. Instead, use dynamic decrease in the spray water flow rates, dropping more gradually towards the steady-state flow rates in the spray table. A spray cooling control like the PI control or the Dynamic spray cooling control can lessen the creation of bridging.

CHAPTER 8.

DYNAMIC MODELING OF THE UNSTEADY BULGING WITH CONOFFLINE

In the continuous casting of steel, bulging is an important phenomenon where the internal ferrostatic pressure, partially restrained by the support rolls, causes the partially solidified shell to bulge outward between each pair of rolls. Bulging is directly responsible for internal cracks, centerline segregation, and permanent slab-width variations [71]–[73]. It also increases roll forces and roll wear. In addition, time-variations of the bulged shape may cause volume changes of the molten steel contained within the solidifying shell in the strand, leading to mold level fluctuations. Such fluctuations may correspond to the time period between certain roll pitches, or certain roll diameters in different zones of the caster [73].

It is well known that excessive mold level fluctuations lead to strand surface cracks, and even breakouts. Mold level control has been studied for many years [74], [75] to minimize these problems. However, the mold level control system has difficulty recognizing and responding to dynamic bulging and cannot prevent it. Other methods, such as increasing the spray cooling in the secondary cooling region to decrease the surface temperature and thicken the shell, and adoption of non-uniform roll pitch have been proposed to reduce dynamic bulging problems [73], [76].

The previous work to study bulging has focused mainly on the steady bulging, using Finite Element Analysis (FEM) [71], [77], [78]. A few recent studies have measured the unsteady bulging in the casting machine using the position detectors between the rolls [73], [79]. Such detectors are useful for model validation but are not feasible for every-day online use, especially in the thin-slab

casters, and have never been used to help mold level control systems. Our approach is to use the dynamic model, ConOffline, to predict the bulging amplitude.

To the best of the author's knowledge, this work is the first attempt to develop a dynamic bulging model that is calculated fast enough for implementation into the real-time online control systems and validated with the plant measurements. The dynamic model, ConOffline, which captures the behavior of the 2-D longitudinal domain through interpolation of multiple 1-D moving slices, is used to calculate the bulging amplitudes. A new dynamic-volume model then calculates the volume change induced by the dynamic bulging and the stopper rod movement. This model is verified through the plant measurements and applied to gain new insight into the dynamic bulging phenomenon.

8.1 A Dynamic Bulging Model

8.1.1 A steady bulging model

The maximum bulging amplitude, δ_{max}, within each within each roll pitch is found from the following equation based on fitting many FEM simulations, proposed by Yu [78], knowing the local strand surface temperature, the shell thickness, the roll pitch, and the ferrostatic pressure calculated using $P = \rho g h$.

$$\delta_{\max}\left(mm\right) = 7.1496\times10^{-34}\,\frac{L_{(mm)}^{6.5}P_{(MPa)}^{1.993}T_{surf\,(^{o}C)}^{8.766}}{d_{(mm)}^{5.333}} \tag{8.1}$$

where P is the ferrostatic pressure, L is the roll pitch, T_{surf} is the strand surface temperature, and d is the solidified shell thickness.

8.1.2 A dynamic bulging model for the unsteady bulging

Bulging of the strand involves both the static and the dynamic components according to the time variations of the bulging which accompany the movement of the strand. Figure 50 illustrates the steady and the unsteady bulging. With the steady bulging, the surface profile of a strand is constant with time, and each portion of the steel shell follows the bulged profile, wiggling akin to a snake as it moves down with the casting speed. Although the strand bulges outwards between rolls, and is pushed back beneath rolls, the mold level stays constant because the volume of molten steel obtained inside the solidifying shell does not change with time. In contrast, with unsteady bulging, the contorted shape of the strand surface becomes partially frozen, so the bulged profile moves down the caster. When the steady bulged shape of the solidified shell, called the “concave profile”, moves between the rolls, the strand must be squeezed inwards. The total volume of molten steel contained within the strand decreases which causes the mold level to rise. Continuing down the caster, the strand experiences repeated transverse expansions and contractions, resulting in the repeated vertical mold level fluctuations.

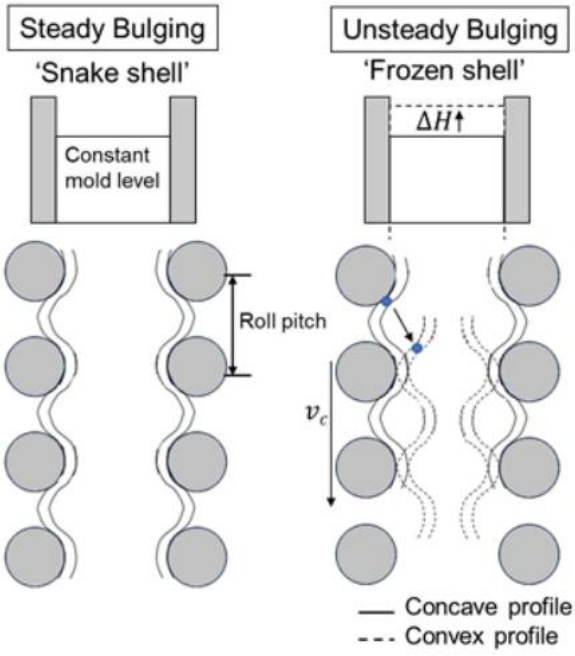

Figure 50. Schematic illustration of steady, unsteady dynamic bulging.

To model this behavior, molten steel flow is divided into three components: inflow into the mold through the stopper rod, outflow due to the downward movement of the solidifying shell at the casting speed, and the liquid steel flow due to the transverse movement of the solidified shell. The latter component is found by tracking the changes in the volume of the molten steel inside the solidified shell according to the shape of the bulged strand, the extent to which it is partially "frozen", and its downward movement. This volume change, ΔV_b, will induce the mold level fluctuations, which the mold level control system will attempt to compensate. The resulting movement of the stopper rod, which changes the inlet steel flow rate from the tundish, induces the transient volume changes, ΔV_s. Any time-variation in the casting speed will introduce further volume changes, ΔV_o. As shown in Figure 51, ignoring the other effects, the following volume conservation equation gives the total time-varying volume change of the strand, ΔV_m:

$$\Delta V_m = -\Delta V_b + \Delta V_s - \Delta V_o \tag{8.2}$$

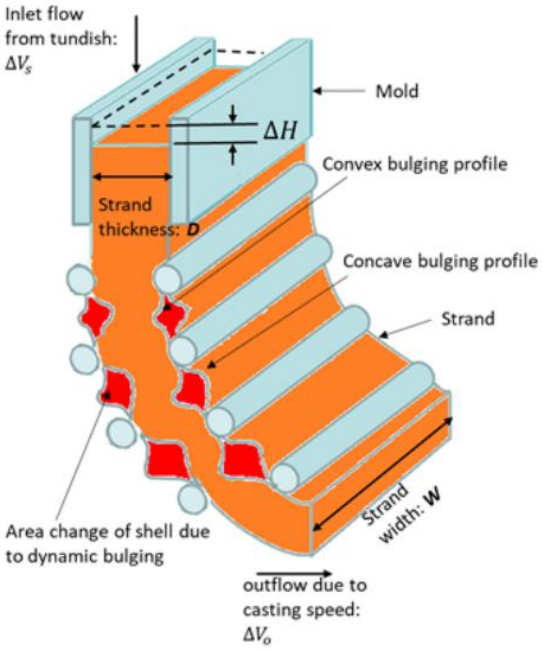

Figure 51. A schematic diagram of an evaluation of the volume change due to the unsteady bulging.

This total volume change of the molten steel also can be found from the measured mold level fluctuations, ΔH:

$$\Delta V_m(t) = \Delta H\left(t\right)WD, \tag{8.3}$$

where W is the strand width, D is the strand thickness, and the average $\Delta H(t)$ is estimated by the mold level sensor. In the steady-state, or the "snaking shell" case, the volume change induced by the bulging is zero, i.e. $\Delta V_b = 0$. In the partially-frozen shell case, it depends on both the inter-roll bulging profile along the entire strand, and the shape change as the strand moves down the caster. In a slab caster with a relatively constant width, this simplifies to:

$$\Delta V_b = \sum A_i W, \tag{8.4}$$

where A_i is the area change in the i^{th} roll pitch induced by the repeated transverse expansions and contractions of the strand. The dynamic bulging model in this section is developed for the unsteady

bulging case. For simplicity, the maximum bulging location is assumed to be at the center of the roll pitch, midway between the rolls, and the bulging profile was very roughly approximated as triangular. Figure 52 shows the two extreme cases in unsteady bulging over one roll pitch: the concave and the convex profiles. Due to the creep deformation, the bulging amplitude is assumed to decrease after the bulged 'peak' moves from midway between rolls to lie directly under the next roll. The following assumptions were made for simplicity: 1) this decrease in the height happens linearly from the concave profile to the convex one; 2) $\delta_{min} = f\delta_{max}$, f is set to be 0.5 in this study; 3) the bulging at each roll pitch is independent.

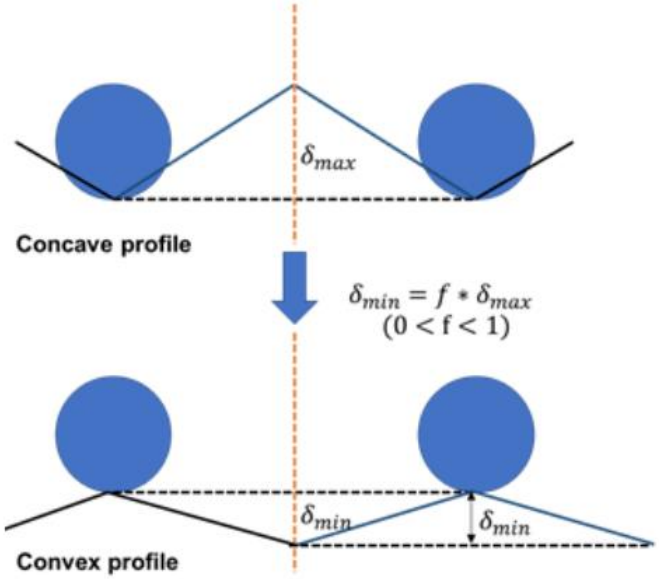

Figure 52. The concave and the convex profile formed as realization of the triangular bulging profile assumption.

To calculate the time evolution of the $x - z$ area change of the bulging profile with the strand movement, the concave profile of the steady bulging was taken as the initial state. The passing line of the steel strand was taken as the zero reference. Denoting by z the strand position along the casting direction starting from time $t = 0$, the area change in a single roll pitch L can be given by

$$A_i(z)=\begin{cases} 0.5\left((L-2z')\left(1-\dfrac{2z'}{L}\right)-\dfrac{4z'^2}{L}\right)\left(1-(1-f)\dfrac{2z'}{L}\right)\delta_{\max}, z\in[nL,\dfrac{L}{2}+nL), \\ 0.5\left(-2(L-z')*\left(1-\dfrac{2z'-L}{L}\right)+\dfrac{(2z'-L)^2}{L}\right)\left(f+(1-f)\dfrac{2z'-L}{L}\right)\delta_{\max}, z\in[\dfrac{L}{2}+nL,L+nL), \end{cases} \tag{8.5}$$

where $z'=z \bmod L, n=1,2,.....$ The distance that the strand moved, z(t), can be calculated from the casting speed $v_c(t)$:

$$z(t)=\int_0^t v_c(\tau)\,d\tau. \tag{8.6}$$

Then the total volume change due to bulging can be calculated as:

$$\Delta V_b(t)=\sum A_i\left(z(t)\right)W \tag{8.7}$$

8.1.3 A stopper rod flow model

A pressure drop - flow rate model for the stopper rod systems (PFSR), developed at the Colorado School of Mines [32] is used to estimate the time-dependent inlet steel flow rate, based on the input stopper position history recorded at the plant. The PFSR is a stand-alone MATLAB based program that solves a system of Bernoulli equations for the flow rate and the pressure distribution down the entire system from the tundish top surface, through the SEN, to the mold top surface. The details of the model are presented in [32].

During continuous casting, the stopper rod is susceptible to erosion. To minimize the effect of erosion, the data were collected from the temporal regions in the plant measurements where there was a constant casting speed followed by a sudden change (increase or decrease of the casting

speed), and finally followed by another time period of a constant casting speed. The throughput differences within this short period should be attributed to the stopper rod movement.

The average erosion rate was estimated for the entire casting sequence, according to the flow-rate changes during the time periods of the constant speed. After accounting for the erosion, the stopper rod data were extrapolated to the zero flow rate at the zero stopper position. After further calibration and validation of the PFSR with the 18 sets of the measurements, the following linear interpolation of the stopper rod inlet flow rate by the PFSR was obtained

$$Q_s(t) = 0.5942 \times h(t) + 0.764, \tag{8.8}$$

where Q_s(ton/min) is the inlet flow through the stopper rod opening, $h(t)$ (mm) is the stopper rod opening. This linear interpolation is considered to be valid only for a narrow range of stopper rod opening (3.2 mm - 4.7 mm) and the flow rate (2.66 (ton/min) -3.53 (ton/min)), which happens to be relevant for the typical casting conditions at the plant.

8.1.4 The computational procedure

The calculation procedure based on these models is as follows:

- ConOffline calculates the maximum bulging amplitude at each roll pitch based on the recorded or the specified casting conditions including the slab geometry, the casting speed, the spray flow rates, the steel grade, etc. for each time step, Δt (1 sec in this study), based on the shell-thickness and the surface temperature profiles down the strand.

- Next, the dynamic bulging model calculates the mold level fluctuation caused by the volume changed due to bulging, $\Delta V_b(t)$ from equations (8.2)-(8.7) knowing the local

strand surface temperature, the shell thickness, the roll pitch, the ferrostatic pressure, and the casting speed.

- The inflow volume induced by the stopper-rod movements is calculated from the inlet steel flow based on equation(8.8), knowing the stopper rod position measurement $h(t)$ as follows:

$$\Delta V_s(t) = Q_s(t)\Delta t \tag{8.9}$$

- The outflow volume due to the downward movement at the casting speed, $v_c(t)$, is found from

$$\Delta V_o(t) = v_c(t) WD\rho\Delta t \tag{8.10}$$

Since, the casting speed is relatively constant during this simulation, the variation of the outflow volume from mold is almost negligible.

- The total volume change history in the mold can be calculated from equation (8.3) knowing the mold level position measurement.

8.2 Simulation Results and Discussion

8.2.1 The casting conditions

The casting scenario simulated is shown in Figure 53. The first plot shows the casting speed history, which is relatively constant around 3.1 m/min. The spray flow rates in the secondary cooling zones 5 and 6 were increased at around 1000 seconds because large bulging in these 2 zones was suspected. The last two plots are the measured mold level position and the stopper rod

position, which show the evidence of a significant dynamic bulging followed by a time interval where only small bulging is suspected. Steel composition was changed at around 2700 seconds, which appears to be at least partly responsible for the decrease of the unsteady bulging.

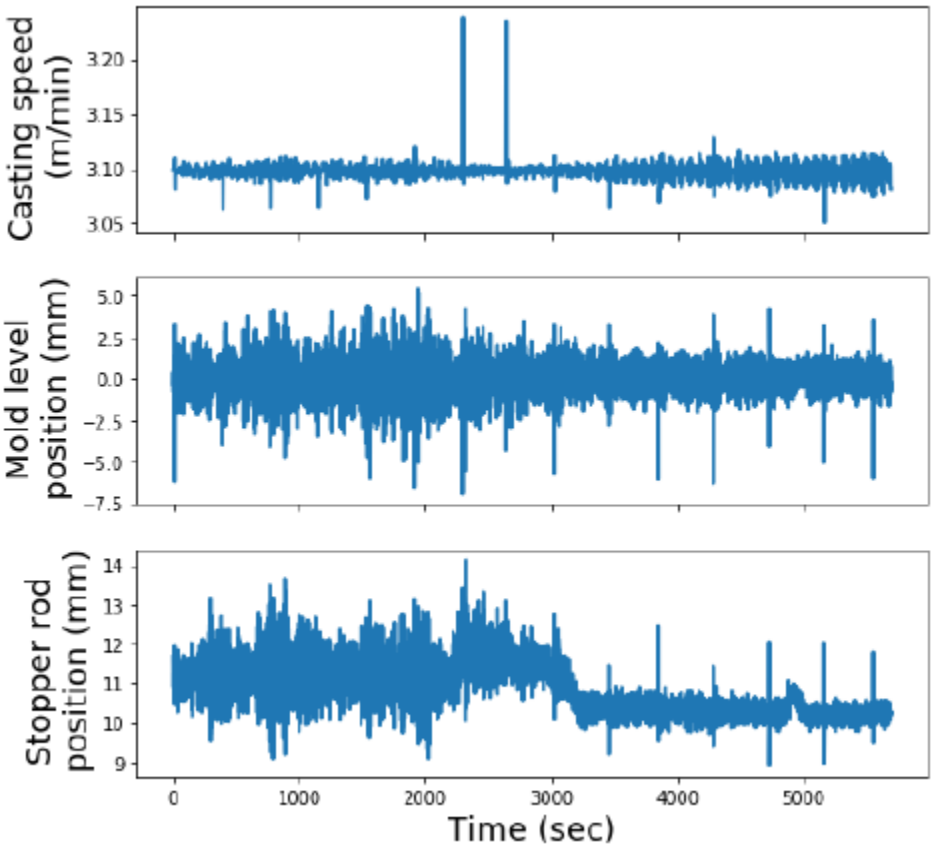

Figure 53. The simulated casting scenario.

8.2.2 The stopper rod flow model results

First, the new volume model was applied to the measured scenario, including only the effect of the stopper rod movements, and neglecting any dynamic bulging. A comparison of the calculated and the measured mold level position histories is shown in Figure 54 for two time intervals: 500-510 seconds (dynamic bulging suspected) and 3400-3410 second (no bulging problems suspected). The differences between the calculated mold level from the stopper rod flow

model and the measured mold level should be explained by the dynamic bulging. When the dynamic bulging is suspected to be large (the left figures), the model greatly over-predicts the level fluctuations. This indicates that in the real caster, the level control system was compensating for those changes. This is also indicated by the difference between the measured throughput, which was constant, and the model predicted inlet flow, which appears to have been almost exactly compensating for the significant dynamic bulging. When dynamic bulging was small, (right figures), the predicted mold level is similar to the measurements indicating that the mild level fluctuations are caused by the stopper rod movement and the surface waves.

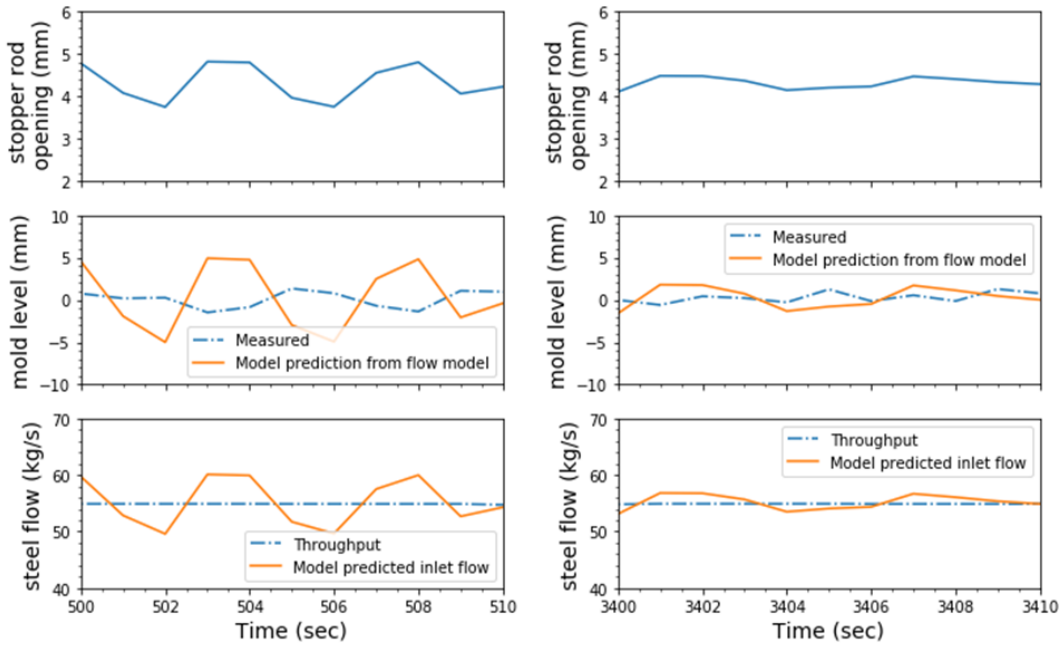

Figure 54. Measured mold level position and calculated mold level position due to the variation of inlet steel flow.

To better illustrate the importance of dynamic bulging, the model prediction of the mold level (considering the stopper-rod movement only) was subtracted from the measured mold level signal, i.e. $\Delta V_m - \Delta V_s + \Delta V_o$, and converted into $\Delta H(t)$ using (247) This new prediction, "model prediction with no level control", represents the expected mold level history if the stopper opening had been held constant (i.e., with no level control system). This prediction shown in Figure 55,

confirms the suspicion that dynamic bulging must have been very severe during this time interval. Furthermore, it shows that the stopper rod movement due to the level control system was helping to decrease the mold level fluctuations. Note, however, that there is still much room for improvement, if the unsteady bulging could be decreased or eliminated, or the mold level control system could be improved.

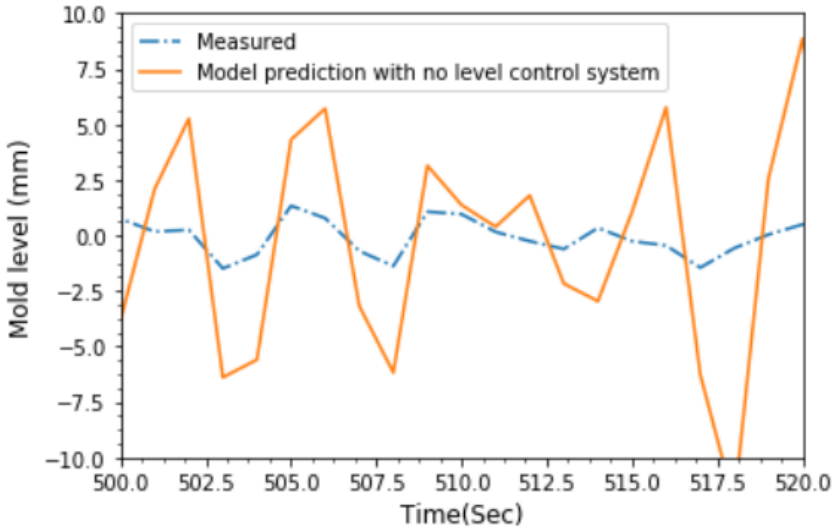

Figure 55. A comparison of the measured and the calculated mold level histories, including dynamic bulging.

8.2.3 The dynamic bulging model results

Next, to predict dynamic bulging, the bulging amplitude calculated from equation (245) was simulated for each roll pitch, and used to predict the mold level fluctuation induced by the dynamic bugling. The “model prediction with no level control” explained in the previous sections, which is the differences between the calculated mold level from the stopper rod flow model and the measured mold level, was used as a comparison with the dynamic bulging model prediction. Figure 56 shows these two predictions for the time intervals of 500-700 seconds and 4400-4600 seconds. In the interval of 500-700 seconds, during which a significant dynamic bulging was suspected, the magnitude of the prediction from the dynamic bulging model is two times bigger than the model

prediction with no level control system. We argue that this difference is caused by assuming dynamic bugling in all zones in the dynamic bulging model, while in the real caster, it may be the steady bulging in certain regions and the dynamic unsteady bulging in the other regions. The trend of the two signals shows a qualitative match with similar clustering of the peaks. However, for 4400-4600 seconds, the two signals do not match. This suggests that after the steel grade change, the new shell becomes more susceptible to creep, so the bulging profile reverts from the dynamic to the more steady bulging, with the smaller f-value, and thus reduces the volume changes and the mold level fluctuations. Indeed, with the minimal dynamic bulging, the measured signal is more likely to be caused by the random turbulent flow and the surface waves, which cannot be controlled by the stopper-rod movement

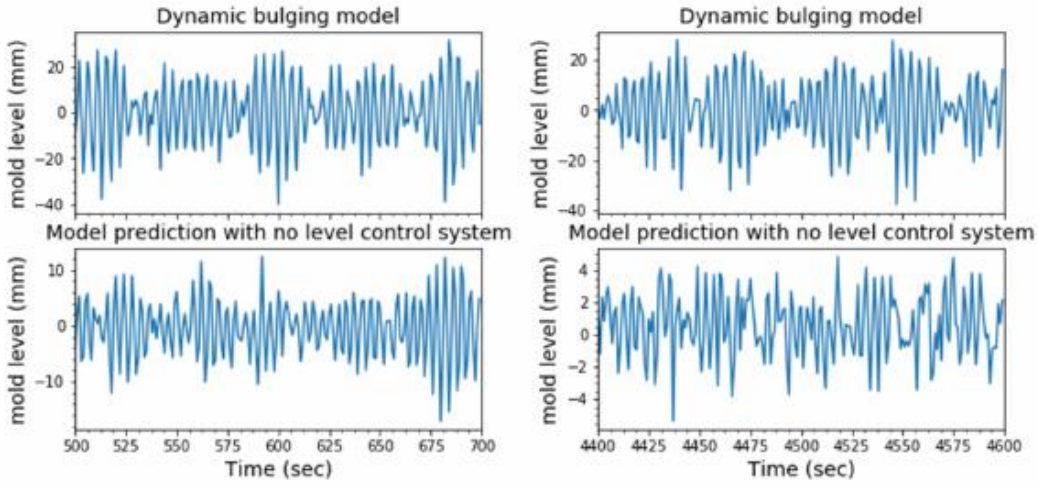

Figure 56. A mold level prediction with the dynamic bugling model with no control system for 500-700 sec and 4400-4600 sec.

The power spectrum density (PSD) analysis of the signals in Figure 56 is shown in Figure 57. The period used for the Fast Fourier Transform is 200 seconds. When a bad dynamic bulging is suspected (500-700 sec), the PSD of the measured signal shows that the main frequency is the frequency corresponding to the roll pitch in zone 5, while the PSD of the estimation shows the matching frequency at zone 5, and zone 6. When a small dynamic bulging is suspected (4400-4600

sec), the PSD of the measurement shows no matching frequency of the roll pitch in the spray zones, and it appears to be the random noise. This also supports the hypothesis that there is the steady bulging during the 4400-4600 seconds interval. However, peaks with smaller magnitude can be spotted at the frequency corresponding to zone 5 and zone 6 in the PSD of the estimation of the mold level, i.e. the model predicts unsteady building at zone 5 and zone 6 as well. This is because the dynamic bulging model was simulating a case of unsteady bulging throughout the caster. Therefore, it should not match the steady bulging results.

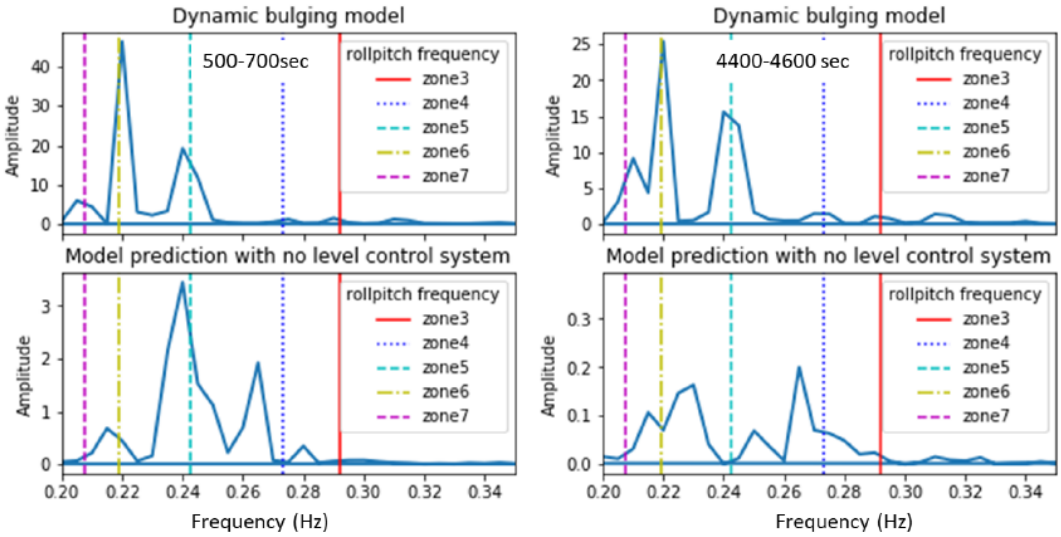

Figure 57. The power spectral density analysis of the measured and the estimated mold level position-time signals shown in Figure 56.

8.3 Summary

A dynamic-volume model has been developed to relate the volume changes from the dynamic unsteady bulging and the stopper-rod movements to the level fluctuations in the continuous slab-casting process. The model incorporates separate submodels to predict the steady-state bulging and the relation between the flow-rate and the pressure drops according to the stopper-rod position. The model predictions of the history of the mold level variations caused by the unsteady bulging matches reasonably with the measurements of the mold level history in a thin-slab caster. The

Power Spectral Density analysis shows that for the studied case, the dynamic bulging in zone 5 appears to be responsible for the level fluctuations, as the dynamic volume model is able to catch the zone 5 frequency peaks. This work confirms that dynamic bulging is responsible for the significant mold level fluctuations in the plant under some circumstances. Furthermore, the model shows that the mold level control system only partly compensates the level fluctuations induced by the dynamic bulging, making them only slightly less severe than the ones that would have occurred with a constant stopper position. This leaves a significant room for possible improvement of the mold-level control systems. This work is only a preliminary step in modeling of the unsteady dynamic bulging. To fully understand the dynamic bulging, much more work would be required.

CHAPTER 9.

SUGGESTION FOR FUTURE WORK

9.1 Motion Planning for Steel Casting

Profitability changes according to many circumstances that introduce significant complexity in determining optimal casting conditions. Avoiding cracking problems is the most important concern that determines cooling conditions for some steel grades: automotive grades are prone to surface problems, while high-alloy structural steels suffer more from internal cracks. Many other grades are not particularly crack prone, however, so other concerns dominate. Maximizing productivity is the objective when there is a backlog of steel at the ladle station and a shortage at the rolling mill. This problem is common in good economic times, especially when the casting capacity is the rate-limiting processing step. At other times, a backlog at the rolling mill may require the caster to run as slowly as possible to avoid an expensive and defect-prone "tailout", where the entire casting operation is stopped and restarted. Between these two extremes, a common objective is to "pace" the caster by choosing a casting speed that balances the throughput with the other plant operations in order to maximize the length of a casting sequence. Finally, an environmentally-conscious operation should conserve energy by cooling the slab as little as possible to retain its internal energy. The caster operation should adapt according to the most urgent need, while still optimizing other aspects as much as possible. This is the real, difficult, unaddressed task in controlling the commercial continuous casters, and the goal of the proposed work is to rigorously address this task at the fundamental broadly applicable level.

In Chapter 6 an optimal control approach for minimizing the metallurgical length deviation during the casting speed increase under the constraints on the secondary cooling flow rates for the

continuous steel casting process is proposed. This approach can be extended to the more complicated operational objectives: 1) Pacing Mode – balancing throughput with the rest of the plant in order to maximize the continuous-casting sequence length, 2) Maximum Productivity Mode - maximizing caster throughput, 3) Time Conservation Mode - maximizing casting time to provide a temporal buffer between upstream and downstream operating units, 4) Energy Conservation Mode - maximizing the thermal post-casting slab energy to reduce the reheating furnace energy loss; all subject to the following constraints: 1) Internal and 2) Surface Quality – maintaining surface temperature history within a process window that minimizes possibility of forming an internal or surface crack, 3) Whale formation avoidance – keeping the metallurgical length (the liquid core of the strand) within the containment zone of the roll support.

An obvious approach is to design different cost functions for different objectives and solve the optimal control problem numerically. However, there are several considerations to take into account. 1) While solving the new problems one should be careful to avoid bringing back the old ones - steel casting is a complicated process, therefore adding the new cost functions, tweaking the existing ones, or changing the weights may degrade the solutions that already reasonably work. 2) Balancing the costs at the drastically different magnitude scales, while considering the controller feasibility, the operation safety, and the efficiency. 3) Creating the cost functions - in the metallurgical length control, formulating the cost function is obvious, but in many other situations, like, fir example, bulging, it is not.

Another challenge lies in the calculation time. Currently, the calculation time for the case of one 1.75 m long zone with the two slices simulation takes approximately 8.1 s on Intel Xeon 3.4 GHz CPU with 8G RAM for one forward step, for the backward step it takes 8.3 s, and the average computation time for a one line minimization step is 6.7 s. The optimization procedure is

terminated after 1790 iteration with approximately 11 hours. For an entire caster, such as a thick-slab one – with the length of more than 10 m, and many spray zones and slices to consider, the calculation time would be much higher.

9.2 Developing Realistic Hysteresis Operator and Proving the Convergence

In Chapter 5, the hysteresis due to boiling $F(T(0,t)$ is modeled using the line segments and the heat flux multipliers, whereas in the actual application, the hysteresis operator may be a random curvature function.

Also the closed loop convergence of $\tilde{T}, \tilde{s}$ to 0 is not proved yet. For this, an obvious Lyapunov functional has not been yet found. Another possible approach is to abandon the Lyapunov stability theory and examine the solutions of the error system using more sophisticated functional analysis.

9.3 The Spray-zone Control

The most critical step standing between the current algorithm and its implementation is that the current control design only follows a single slice of the caster. At any point in the caster, the work in this dissertation implicitly assumed that the water flow rate could be chosen to best suit that particular slice's temperature. Casters, however, only have a handful of spray zones in which the water flow rate through every nozzle is the same. Any slice in each zone will receive the same water flow rate. Rather than following the material as it moves through the caster, which was useful for simplifying the governing nonlinear PDE to a 1-D problem that could be easily analyzed mathematically, the spray zone covers a fixed 2-D spatial domain. There are two problems with designing a similar enthalpy-based control law.

First, the temperature upstream of the spray zone cannot be controlled by changing the water in the spray zone. Second, by studying a fixed spatial domain, advection must be considered at the same time as conduction. This shows up as a term $v_c \frac{\partial T}{\partial z}$ in the PDE. That is, changing the casting speed changes the differential operator. Both problems lead to the same conclusion: matching a fixed reference profile in a spray zone is fundamentally impossible.

That being said, this does not mean that control of the spray zone is impossible. A good option for applying the controllers designed in this work is to develop a reference profile generator that translates the operational requirements into the realizable reference temperature motions and casting speed input sequences ensuring safety and product quality. Then, similar controllers as the ones designed in this work can be implemented to regulate the temperature and the shell thickness

9.4 Extended Application

Due to the complex nature of the steel casting process, it is dangerous and expensive to perform experiments on the actual caster. With the help of the model, ConOffline, which acts as a digital twin of the casting process that provides insight into the caster, many new applications are possible with ConOffline.

In the development of the new generations of steel, like the high strength steel, there are many new challenges in the casting process. Dynamic bulging of the steel strand is one of the challenges. In Chapter 8, a preliminary step was taken to model the dynamic bulging using the ConOffline model. A more sophisticated model of the bulging between the rolls is needed to make the ConOffline model prediction of bulging more accurat.

APPENDIX A.

NUMERICAL SIMULATION BACKGROUND

Th e simulation technique used is a straightforward calculation of (48) using the Finite Difference Method (FDM). Denote the discretized temperature as

$$\left\{T^i\left(t\right)\right\}_{i=0}^{n} = \left\{T\left(i\Delta x, t\right)\right\}_{i=0}^{n} \tag{A.1}$$

where

$$\Delta x = \frac{L}{n} \tag{A.2}$$

is the grid spacing. Then, the well-known second–order accurate difference approximation for the second spatial derivative is

$$\frac{d}{dt}h\left(T^i\right) = kT_{xx}\left(i\Delta x, t\right) = k\left(\frac{T^{i+1} - 2T^i + T^{i-1}}{\left(\Delta x\right)^2} + O\left(\left(\Delta x\right)^2\right)\right). \tag{A.3}$$

Therefore, using the simple forward Euler integration scheme in time for (48),

$$h\left(T^i\left(t + \Delta t\right)\right) \approx h\left(T^i\left(t\right)\right) + k\frac{T^{i+1} - 2T^i + T^{i-1}}{\left(\Delta x\right)^2}\Delta t. \tag{A.4}$$

Obviously, this only applies to the internal nodes, for which T^{i-1} and T^{i+1} are within the problem domain. For this to be applied to the boundary nodes $i = 0$ and$i = n$ would require values for T^{-1} and T^{n+1}, respectively, which are not physically meaningful in the discretization scheme given, since they refer to points outside of the problem domain.

However, the boundary conditions (2.25) should apply, and this suggests a way of creating these “dummy node” values. If T^{-1} did exist, then applying the boundary condition and the second–order accurate difference equation would mean that

$$T_x(0,t) = \frac{T^1 - T^{-1}}{2\Delta x} + O\left((\Delta x)^2\right) = u. \tag{A.5}$$

Solving this for the dummy node T_{-1} gives the approximation

$$T_{-1} \approx T_1 - 2u\Delta x. \tag{A.6}$$

This approximation can be used in (A.4) to update the boundary node $i = 0$. Similarly, the approximation for node $i = n$ uses the dummy node

$$T_{n+1} \approx T_{n-1}, \tag{A.7}$$

based on the boundary conditions.

Altogether, the following procedure is used to numerically integrate the PDE using this FDM.

1. From the previous nodal temperature values, calculate the new nodal values of the enthalpy $h(T_i)$ using equations (A.4)–(A.7).

2. From these new enthalpy values, calculate the new nodal values of the temperature by inverting equation (2.2).

Analytical solution for (2.24), (2.27)with Dirichlet boundary condition is given in [44] (pp 113-115).

APPENDIX B. MATHEMATIC BACKGROUND

B.1 Lagrangian and Eulerian Coordinates System

There are two methods that are widely used to observe and analyze fluid flows, either by observing the trajectories of the specific fluid parcels, which yields what is commonly termed a Lagrangian representation, or by observing the fluid velocity at fixed positions, which yields an Eulerian representation [80].

B.1.1 Lagrangian description

In the Lagrangian description of fluid flow, the individual fluid particles are tracked. Each fluid particle caries its own properties such as density, momentum, velocity, etc. As the particle advances its properties may change in time. The procedure of describing the entire flow by recording the detailed histories of each fluid particle is the Lagrangian description. The properties of particle P such as density, velocity, temperature, etc. can be mathematically represented as $\rho_P(t), \vec{v}_P(t), T_P(t)$. The Lagrangian description is simple to understand: conservation of mass and Newton's laws apply directly to each fluid particle . However, it is computationally expensive to keep track of the trajectories of all the fluid particles in a flow.

B.1.2 Eulerian description

In the Eulerian description of the fluid flow, the individual fluid particles are not identified. Instead, a control volume is defined. Pressure, velocity, acceleration, and all other flow properties are described as fields within the control volume. In other words, each property is expressed as a function of space and time. For example, the density, velocity, temperature, etc. can be

mathematically represented as $\rho(\vec{x},t), \vec{v}(\vec{x},t), T(\vec{x},t)$, where $\vec{x}$ represents space vector. However, the physical laws such as Newton's laws and the laws of conservation of mass and energy apply directly to particles in a Lagrangian description. Hence, some translation or reformulation of these laws is required for use with an Eulerian description.

B.1.3 Material derivative

The material derivative gives a way to relate the Lagrangian description to the Eulerian one. The material derivative of some flow quantity Q (like temperature, pressure, etc.) is defined as the rate of change of that quantity following a fluid particle. For an arbitrary fluid property $Q(x,y,z,t)$ in a 3D domain,

$$\begin{aligned}\frac{DQ}{Dt} &= \frac{\partial Q}{\partial t}\frac{dt}{dt} + \frac{\partial Q}{\partial x}\frac{dx}{dt} + \frac{\partial Q}{\partial y}\frac{dy}{dt} + \frac{\partial Q}{\partial z}\frac{dz}{dt} \\ &= \frac{\partial Q}{\partial t} + \frac{\partial Q}{\partial x}v_x + \frac{\partial Q}{\partial y}v_y + \frac{\partial Q}{\partial z}v_z\end{aligned} \tag{B.1}$$

The generalized notation:

$$\underbrace{\frac{D}{Dt}}_{\text{Lagrangian}} = \underbrace{\frac{\partial}{\partial t} + \vec{v}\cdot\nabla}_{\text{Eulerian}} \tag{B.2}$$

Note that Q can be any fluid property, scalar or vector. Taking steel casting as an example, Q represents the temperature, in which case one obtains the material derivative or substantial derivative of the temperature. In other words, dT/dt is the rate of change of temperature following a fluid particle. The material derivative is a filed quantity, i.e. it is expressed in the Eulerian frame of reference as a function of space and time (x,y,z,t). Thus, at some given spatial location (x,y,z) and at some given time t, DQ/Dt is the material derivative of Q, and is defined as the total rate of change of Q with respect to time as one fluid particle happens to be at that location at

that instant of time. Q changes for two reasons: first, if the flow is unsteady, Q changes directly with respect to time. This is called the local or unsteady rate of change of Q. Second, Q changes as the fluid particle migrates or convects to a new location in the flow field. This is called the convective or advective rate of change of Q.

B.2 Lyapunov Stability and LaSalle Invariance

A "finite-dimensional" dynamical system is the one that can be described by the differential equation

$$\dot{x} = f(x) \tag{B.3}$$

where x is the state of the system in the state space $X = \mathbb{R}^n$, with Euclidean norm $\|x\|$. The function $f(x)$ is a (possibly nonlinear) function. In general, the main focus of modern control theory is finding ways to put some limits on the behavior of the system without actually having to solve the differential equations.

One of the most important tools is the LaSalle's invariance principle, which is written as follows (Theorem 4.4, [81]):

Theorem B.1. Let $\Omega \subset D$ be a compact set that is positively invariant with respect to (B.3). Let $V: D \to \mathbb{R}$ be a continuously differentiable function such that $\dot{V}(x) \leq 0$ in Ω. Let E be the set of all points in Ω where $\dot{V}(x) = 0$. Let M be the largest invariant set in E. Then, every solution starting in Ω approaches M as $t \to \infty$.

The result can be strengthened further if V is assumed to be radially unbounded (the limit as $\|x\| \to \infty$ of $V(x)$ is ∞) with $\dot{V} \leq 0$. In that case, any sublevel set $\{x \mid V(x) \leq c\}$ is compact and positively invariant.

Without repeating the full proof, the basic idea is that if the trajectory stays in a compact set, it must have "positive limit points," a set of points to which some subset of the trajectory converges. It turns out that the trajectory itself must converge to the set of all such positive limit points. This set is then proven to be contained in M, which finishes the proof.

B.3 Infinite–dimensional Systems

An "infinite-dimensional" (or often, "distributed parameter") system is defined similarly to (B.3), but instead of $\mathbb{R}^n$, the state space is represented by some infinite-dimensional space X with norm $\|y\|$. In this dissertation, the space used most commonly is the Sobolev space $H^2(0,\ell)$, the space of all functions with a weak derivative in $L^2(0,\ell)$. The norm in this case is

$$\|y\| = \|y\|_2 + \left\|\frac{\partial y}{\partial x}\right\|_2$$

where $\|y\|_2$ is the usual L^2 norm,

$$\int_0^\ell y(x)^2\,dx.$$

The problem with applying LaSalle's theorem to this system is that the idea of compactness is different for infinite-dimensional systems. LaSalle's theorem used the fact that the trajectory $f(x)$ is closed and bounded to say that it contained convergent subsequences, with limits in the positive limit set. In finite-dimensional spaces, any sequence that is closed and bounded is compact, in the sense that it has such limits. If the state-space is infinite dimensional, this is not true, and compactness of the trajectory has to be proven some other way.

The book [57] by Walker gives some examples of extensions of LaSalle's principle to infinite dimensional system. In that book, a dynamical system is defined by a strongly continuous semigroup, $S(x)$, where $S(x)y_0$ maps the initial condition of the system $y(0) = y_0$ to its state at time t,

$$y(t) = S(x)y_0.$$

In finite dimensions, this is the state-transition matrix. In infinite-dimensions, it has a more abstract definition.

Theorem 6.3 in Chapter IV of [57] is the equivalent of LaSalle's theorem used in this dissertation:

Theorem B.2. Let $S(x)$ be a dynamical system on metric space $\mathcal{X}$, and let $V: \mathcal{X} \to \mathbb{R}$ be a Lyapunov function on a set $\mathcal{G} \subset \mathcal{X}$. Let $\mathcal{Y}$ be a complete metric space such that $\mathcal{X} \subset \mathcal{Y}$ and the injection $\hat{I}: \mathcal{X} \to \mathcal{Y}$ is compact and continuous. Let there exist lower semicontinuous functions $\hat{V}: \mathcal{Y} \to \mathbb{R}$, $\hat{W}: \mathrm{Cl}_{\mathcal{Y}}\mathcal{G} \to \mathbb{R}^+$, such that

$$\begin{aligned} V(x) &= \hat{V}(x), x \in \mathcal{G} \subset \mathcal{Y}, \\ \dot{V}(x) &\le \hat{W}(x), x \in \mathcal{G} \subset \mathcal{Y}, \\ \hat{V}(x) &> -\infty, y \in \mathrm{Cl}_{\mathcal{Y}}\mathcal{G}. \end{aligned}$$

If the set $\gamma(x)\{S(x)x | t \ge 0\}$ satisfies $\gamma(x) \subset \mathcal{G}$ and $\gamma(x)$ is bounded in $\mathcal{X}$, then $\hat{d}_y\left(S(t)x, \mathcal{M}_3\right) \to 0$ as $t \to \infty$, where

$$\mathcal{M}_3 \left\{ y \in \mathrm{Cl}_{\mathcal{Y}}\mathcal{G} | \hat{W}(y) = 0 \right\} \in \mathcal{Y}.$$

Comparing Theorems B.2.1 with B.3.1, the equivalents of the space, $\mathcal{X}$, subset containing the trajectory, $\mathcal{G}$, and invariant limit set $\mathcal{M}_3$ in Theorem B.2 are respectively X, Ω, and M in Theorem B.1. Although $\mathcal{G}$ is not bounded by assumption like Ω is, the trajectories $\gamma(x)$ are. The new wrinkle is showing that $\gamma(x)$ is compact, in order to have positive limit points. This is done by embedding $\mathcal{X}$ compactly in another state space $\mathcal{Y}$, which has a different norm. This means that

sets that are bounded by the norm in $\mathcal{X}$ are precompact (i.e. their closure is compact) in the norm in $\mathcal{Y}$, which means the invariance principle can be stated using the norm in $\mathcal{Y}$.

A useful theorem for determining when a set is precompact is the Arzela-Ascoli Theorem (see Appendix C.7 in [35]):

Theorem B.3. A set of continuous functions $\{f_n(x)\}$ on the closed and bounded interval $[a,b]$ is compact in the supremum norm if and only if the functions are uniformly bounded, i.e.

$$f_n(x) \le M \quad \forall n$$

and equicontinuous, i.e. for any $\varepsilon > 0$, there exists a δ. such that

$$\left| f_n(x) - f_n(y) \right| \le \epsilon, \quad \forall \left| x - y \right| < \delta, \quad \forall n.$$

In conjunction with this theorem, there is also the Rellich-Kondrachov Theorem (Theorem 5.5 in [35]) which gives continuous, but not necessarily compact embeddings of Sobolev spaces into other spaces. There are multiple such embeddings for different Sobolev spaces and spatial dimensions. Since the only space used here is $H^2(0,\ell)$, the only embedding of interest is:

Theorem B.4. The Sobolev space $H^2(0,\ell)$ can be continuously embedded in the Holder space $C^{0,\frac{1}{2}}(0,\ell)$, i.e. the set of functions $f(x)$ for which

$$\left\| f \right\|_{0,\frac{1}{2}} = \sup_{x,y\in(0,\ell),x\neq y} \frac{\left| f(x) - f(y) \right|^{\frac{1}{2}}}{\left| x - y \right|} < \infty. \tag{B.4}$$

A continuous embedding maps bounded sets to bounded sets, not precompact sets. However, this can be used sequentially with Ascoli-Arzela Theorem, since a continuous embedding of one space into a second space, followed by a compact embedding of the second space into the third space, is overall a compact embedding of the first space into the third. In this case:

Lemma B.1. The Sobolev space $H^2(0,\ell)$ can be compactly embedded in $C^0(0,\ell)$, the space of continuous functions under the norm

$$\|f\|_\infty = \sup_{x\in(0,\ell)} |f(x)|. \tag{B.5}$$

Proof. By Theorem B.4, $H^2(0,\ell)$ can be continuously embedded in $C^{0,\frac{1}{2}}(0,\ell)$. Take any bounded subset of $C^{0,\frac{1}{2}}(0,\ell)$, which means

$$\frac{|fx-fy|^{\frac{1}{2}}}{|x-y|} \le M. \tag{B.6}$$

Then, for $\varepsilon > 0$, choose $\delta(\frac{\varepsilon}{M})^{\frac{1}{2}}$. Substituting this into (B.6), for any $|x-y| < \delta$

$$|fx-fy| \le M|x-y|^2 \le M\delta^2 = \epsilon.$$

That is, the functions are uniformly equicontinuous and Arzela -Ascoli Theorem implies the set is precompact in $C^{0,\frac{1}{2}}(0,\ell)$. □

B.4 Useful Inequalities and Estimates

The previous section gives the functional analysis results that allow the extension of LaSalle's theorem to infinite-dimensions for the purposes of this dissertation. However, to apply these results requires estimates on the norms of functions on the interval $(0,\ell)$.

The first few of these apply to functions either in $L^2(0,\ell)$ when there is no derivative in the inequality, or the Sobolev space $H^2(0,\ell)$, when a derivative is present. More details on the inequalities, and their use in examining stability of PDEs, can be found in [56]. The Cauchy-Schartz inequality bounds the inner product of two functions by their individual L^2 norms:

$$\int_0^{\ell} y_1(x) y_2(x) dx \le \|y_1\|_2 \|y_2\|_2 \tag{B.7}$$

Poincare's inequality bounds the L^2 norm of a continuously differentiable function by the L^2 norm of its derivative:

$$\|y\|_2^2 \le 2\big(y(\ell)\big)^2 + 4\ell^2 \|y_x\|_2^2 \tag{B.8}$$

Finally, Agmon's inequality gives an absolute bound for a function in terms of the L^2 norms of the function and its derivative:

$$\|y\|_\infty^2 \le \big(y(\ell)\big)^2 + C\|y\|_2 \|y_x\|_2 . \tag{B.9}$$

REFERENCES

[1] "Steel Statistical Yearbook 2017." 2017.

[2] J. Sengupta, B. G. Thomas, and M. A. Wells, "The Use of Water Cooling During the Continuous Casting of Steel and Aluminum Alloys," *Metall. Mater. Trans. A – Phys. Metall. Mater. Sci.*, vol. 36, no. 1, pp. 187–204, 2005.

[3] Y. A. Meng and B. G. Thomas, "Heat Transfer and Solidification Model of Continuous Slab Casting: CON1D," *Metall. Mater. Trans. B*, vol. 34, no. 5, pp. 685–705, 2003.

[4] B. Petrus, K. Zheng, X. Zhou, B. G. Thomas, and J. Bentsman, "Real-Time, Model-Based Spray-Cooling Control System for Steel Continuous Casting," *Metall. Mater. Trans. B*, vol. 42, no. 1, pp. 87–103, 2011, doi: 10.1007/s11663-010-9452-7.

[5] J. K. Brimacombe and K. Sorimachi, "Crack formation in the continuous casting of steel," *Metall. Trans. B*, vol. 8, no. 2, pp. 489–505, 1977, doi: 10.1007/BF02696937.

[6] J. a. J. A. Sirgo *et al.*, "Measurement of centerline segregation in steel slabs," *Conf. Rec. - IAS Annu. Meet. (IEEE Ind. Appl. Soc.*, vol. 1, no. c, pp. 516–520, 2006, doi: 10.1109/IAS.2006.256568.

[7] L. Su *et al.*, "Automatic measurement of Centreline segregation in continuously cast line pipe steel slabs," *Energy Mater. 2014, Conf. Proc.*, no. November, pp. 575–581, 2014, doi: 10.1007/978-3-319-48765-6_70.

[8] G. W. Zuspan, *Basic Metallurgy: Metallurgical equipment and laboratory techniques Ed. by G. William Zuspan*, vol. 2. American Society for Metals, 1957.

[9] K. Fischer, H. Litterscheidt, W. Rudack, R. Simon, and R. Weber, "Industrial experience

gathered in the production of continuously cast slabs," *Thyssen Tech. Berichte*, vol. 10, no. 2, pp. 13–18, 1978.

[10] S. Louhenkilpi, "Chapter 1.8 - Continuous Casting of Steel," in *Treatise on Process Metallurgy*, Elsevier, 2014, pp. 373–434.

[11] C. a. Hernández-Bocanegra, a. H. Castillejos E., F. a. Acosta-González, X. Zhou, and B. G. Thomas, "Measurement of heat flux in dense air-mist cooling: Part I - A novel steady-state technique," *Exp. Therm. Fluid Sci.*, vol. 44, pp. 147–160, 2013, doi: 10.1016/j.expthermflusci.2012.06.015.

[12] Z. Chen, J. Bentsman, and B. G. Thomas, "Bang-Bang Free Boundary Control of a Stefan Problem for Metallurgical Length Maintenance," in *2018 Annual American Control Conference (ACC)*, 2018, pp. 116–121, doi: 10.23919/ACC.2018.8431904.

[13] B. Petrus, J. Bentsman, and B. G. Thomas, "Enthalpy-based Feedback Control Algorithms for the Stefan Problem," in *51st IEEE Conference on Decision and Control (CDC)*, 2012, pp. 7037–7042, doi: 10.1109/CDC.2012.6426035.

[14] W. B. Dunbar, N. Petit, P. Rouchon, and P. Martin, "Motion planning for a nonlinear Stefan problem," *ESAIM Control. Optim. Calc. Var.*, vol. 9, pp. 275–296, 2003, doi: 10.1051/cocv.

[15] B. Petrus, J. Bentsman, and B. G. Thomas, "Feedback control of the two-phase Stefan problem, with an application to the continuous casting of steel," *49th IEEE Conf. Decis. Control*, pp. 1731–1736, 2010.

[16] B. Petrus, J. Bentsman, and B. G. Thomas, "Application of Enthalpy-based Feedback Control Methodology to the Two-sided Stefan Problem," in *American Control Conference*

(ACC) 2, 2014, pp. 1015–1020, doi: 10.1109/ACC.2014.6859062.

[17] A. Maidi and J. P. Corriou, "Boundary geometric control of a linear Stefan problem," *J. Process Control*, 2014, doi: 10.1016/j.jprocont.2014.04.010.

[18] S. Koga, M. Diagne, and M. Krstic, "Control and State Estimation of the One-Phase Stefan Problem via Backstepping Design," *IEEE Trans. Automat. Contr.*, vol. 64, no. 2, pp. 510–525, 2019, doi: 10.1109/TAC.2018.2836018.

[19] S. Koga and M. Krstic, "Arctic sea ice state estimation from thermodynamic PDE model," *arXiv Prepr. arXiv1901.10678*, no. January, 2019.

[20] A. Friedman and L.-S. JIANG, "Nonlinear Optimal Control Problems in Heat Conduction," *SIAM J. Control Optim.*, vol. 21, no. 6, pp. 940–952, 1983.

[21] M. Hinze and S. Ziegenbalg, "Optimal Control of the Free Boundary in A Two-Phase Stefan Problem," *J. Comput. Phys.*, vol. 223, no. 2, pp. 657–684, 2007, doi: 10.1016/j.jcp.2006.09.030.

[22] M. Krasnosel'skii and A. V. Pokrovskii, *System with Hysteresis*. Springer-Verlag Berlin Heidelberg, 1989.

[23] J. W. Macki, P. Nistri, and P. Zecca, "Mathematical models for hysteresis," *SIAM Rev.*, vol. 35, no. 1, pp. 94–123, 1993.

[24] A. Visintin, *Differential models of hysteresis*, vol. 111. Springer Science & Business Media, 2013.

[25] G. Tao and P. V Kokotovic, "Adaptive control of plants with unknown hystereses," *IEEE Trans. Automat. Contr.*, vol. 40, no. 2, pp. 200–212, 1995.

[26] G. Song, X. Zhou, J. A. De Abreu-García, and J. Zhao, “Tracking Control of a Piezoceramic Actuator a Piezoceramic Actuator With Hysteresis Compensation Using Inverse Preisach Model,” *Trans. Mechatronics*, vol. 10, no. 2, pp. 198–209, 2005.

[27] R. V. Iyer and X. Tan, “Control of hysteretic systems through inverse compensation,” *IEEE Control Syst. Mag.*, vol. 29, no. 1, pp. 83–99, Feb. 2009, doi: 10.1109/MCS.2008.930924.

[28] D. S. D. S. Shook, C. Mohtadi, and S. L. S. L. Shah, “Identification for long-range predictive control,” in *IEE Proceedings D (Control Theory and Applications)*, 1991, vol. 138, no. 1, pp. 75–84, doi: 10.1049/ip-d.1991.0010.

[29] S. Tong and Y. Li, “Adaptive fuzzy output feedback control of MIMO nonlinear systems with unknown dead-zone inputs,” *IEEE Trans. Fuzzy Syst.*, vol. 21, no. 1, pp. 134–146, 2013.

[30] A. Friedman and K.-H. K.-H. Hoffmann, “Control of free boundary problems with hysteresis,” *SIAM J. Control Optim.*, vol. 26, no. 1, pp. 42–55, 1988.

[31] I. G. Götz, K.-H. Hoffmann, and A. M. Meirmanov, “Periodic solutions of the Stefan problem with hysteresis-type boundary conditions,” *Manuscripta Math.*, vol. 78, no. 1, pp. 179–199, 1993.

[32] H. Olia and B. G. G. Thomas, “Flow Rate - Stopper Position Model of NUCOR Caster using Pressure Drop Flow Rate Model for Stopper Rod Flow Control Systems (PFSR),” Golden, Co, 2018.

[33] N. Gregurich, G. Flick, R. Moravec, and K. Blazek, “In-depth Analysis of Continuous Caster Machine Behavior During Casting with Different Roll Gap Taper Profiles,” *Iron*

Steel Technol., vol. 9, no. 12, p. 62, 2012.

[34] L. I. Rubinstein, *The Stefan Problem*. Providence, RI: American Mathematical Society, 1971.

[35] L. C. Evans, *Partial Differential Equations (2nd ed.)*. 2010.

[36] J. R. Cannon and C. D. Hill, "Existence, uniqueness, stability, and monotone dependence in a Stefan problem for the heat equation," *J. Math. Mech.*, vol. 17, no. 1, pp. 1–19, 1967, doi: 10.1512/iumj.1968.17.17001.

[37] J. R. Cannon and M. Primicerio, "A two phase Stefan problem with flux boundary conditions," *Ann. di Mat. Pura ed Appl.*, vol. 88, no. 1, pp. 193–205, 1971.

[38] A. Damlamian, "Some results on the multi-phase Stefan problem," *Commun. Partial Differ. Equations*, vol. 2, no. 10, pp. 1017–1044, 1977, doi: 10.1080/03605307708820053.

[39] Z. Chen, J. Bentsman, B. G. Thomas, and A. Matsui, "Study of spray cooling control to maintain metallurgical length during speed drop in steel continuous casting," in *Iron and Steel Technology*, 2017, vol. 14, no. 10, pp. 92–103.

[40] K. Harste, "Investigation of the shrinkage and the origin of mechanical tension during solidification and successive cooling of cylindrical bars of Fe–C alloys," Technical University of Clausthal, 1989.

[41] A. Jablonka, K. Harste, and K. Schwerdtfeger, "Thermomechanical Properties of Iron and Iron-Carbon Alloys: Density and Thermal Contraction," *Steel Res. Int.*, vol. 62, no. 1, pp. 24–33, 1991.

[42] I. Jimbo and A. A. W. Cramb, "The Density of Liquid Iron-Carbon Alloys," *Metall. Trans. B*, vol. 24, no. 1, pp. 5–10, 1993.

[43] P. Duvvuri, B. Petrus, and B. G. Thomas, “Correlation for mold heat flux measured in a thin slab casting mold,” in *AISTech - Iron and Steel Technology Conference Proceedings*, 2014, pp. 2881–2893.

[44] J. A. Dantzig and C. L. Tucker, *Modeling in Materials Processing*. Cambridge University Press, 2001.

[45] C. Cicutti, M. Valdez, T. Perez, G. Gresia, W. Balante, and J. Petroni, “Mould Thermal Evaluation in a Slab Continuous Casting Machine,” in *Proceedings of the 85th Steelmaking Conference*, 2002.

[46] T. Nozaki, J. Matsuno, K. Murata, H. Ooi, and M. Kodama, “A Secondary Cooling Pattern for Preventing Surface Cracks of Continuous Casting Slab,” *Trans. Iron Steel Inst. Jpn.*, vol. 18, no. 6, pp. 330–338, 1978.

[47] B. Petrus *et al.*, “New Method to Measure Metallurgical Length and Application to Improve Computational Models,” *Iron Steel Technol.*, vol. 12, no. 12, pp. 58–66, 2015.

[48] L. C. Hibbeler, B. G. Thomas, R. C. Schimmel, and G. Abbel, “The thermal distortion of a funnel mold,” *Metall. Mater. Trans. B*, vol. 43, no. 5, pp. 1156–1172, 2012.

[49] R. a. Hardin, K. Liu, C. Beckermann, and A. Kapoor, “A transient simulation and dynamic spray cooling control model for continuous steel casting,” *Metall. Mater. Trans. B*, vol. 34, no. 3, pp. 297–306, 2003, doi: 10.1007/s11663-003-0075-0.

[50] Z. Chen, J. Bentsman, and B. G. Thomas, “Optimal Control of Free Boundary of a Stefan Problem for Metallurgical Length Maintenance in Continuous Steel Casting,” in *2019 American Control Conference (ACC)*, 2019, pp. 3206–3211.

[51] B. Petrus, Z. Chen, J. Bentsman, and B. G. Thomas, “Online recalibration of the state

estimators for a system with moving boundaries using sparse discrete-in-time temperature measurements," *IEEE Trans. Automat. Contr.*, vol. 63, no. 4, pp. 1090–1096, Apr. 2018, doi: 10.1109/TAC.2017.2736950.

[52] C. Saguez, "Optimal control of free boundary problems," in *System Modelling and Optimization*, Heidelberg: Springer Berlin, 1986, pp. 776–788.

[53] P. Neittaanmaki and D. Tiba, *Optimal Control of Nonlinear Parabolic Systems: Theory, Algorithms, and Applications*. Marcel Dekker, 1994.

[54] W. B. Dunbar, N. Petit, P. Rouchon, and P. Martin, "Boundary control of a nonlinear Stefan Problem," in *Proceedings ofthe 42nd IEEE Conference on Decision and Control*, 2003, pp. 1309–1314.

[55] O. A. Ladyzenskaja, V. A. Solonnikov, and N. N. Uralceva, *Linear and Quasilinear Equations of Parabolic Type*. American Mathematical Society, 1968.

[56] M. Krstic and A. Smyshlyaev, *Boundary Control of PDEs: A course on Backstepping Designs*. Philadelphia: SIAM, 2008.

[57] J. A. Walker, *Dynamical Systems and Evolution Equations: Theory and Applications*. New York: Plenum Press, 1980.

[58] J. R. Cannon and M. Primicerio, "Remarks on the one-phase Stefan problem for the heat equation with the flux prescribed on the fixed boundary," *J. Math. Anal. Appl.*, vol. 35, no. 2, pp. 361–373, 1971, doi: 10.1016/0022-247X(71)90223-X.

[59] M. A. Krasnosel'skii and A. V Pokrovskii, *Systems with hysteresis*. Springer Science & Business Media, 2012.

[60] K.-H. K.-H. Hoffmann and J. Sprekels, "Real-time control in a free boundary problem

connected with the continuous casting of steel," in *Optimal Control of Partial Differential Equations*, vol. 68, K.-H. Hoffmann and W. Krabs, Eds. Basel, Switzerland: Birkhauser, 1984, pp. 127–143.

[61] X. Zhou, B. G. Thomas, B. C. A. Hernández, E. a H. Castillejos, and A. F. Acosta G.F.A., "Measuring heat transfer during spray cooling using controlled induction-heating experiments and computational models," *Appl. Math. Model.*, vol. 37, no. 5, pp. 3181–3192, 2013, doi: 10.1016/j.apm.2012.07.039.

[62] X. Zhou and B. G. Thomas, "Continuous Casting Consortium Annual Report 2008: New features of CON1D- Version 9.6," Urbana, 2008.

[63] J. Caldwell and Y. Y. Kwan, "Numerical methods for one-dimensional Stefan problems," *Int. j. numer. method. biomed. eng.*, vol. 20, no. 7, pp. 535–545, 2004, doi: 10.2298/TSCI0902061C.

[64] L. M. G. Drummond, A. N. Iusem, L. M. Graña Drummond, and A. N. Iusem, "A projected gradient method for vector optimization problems," *Comput. Optim. Appl.*, vol. 28, no. 1, pp. 5–29, 2004, doi: 10.1023/B:COAP.0000018877.86161.8b.

[65] A. N. Iusem, "On the convergence properties of the projected gradient method for convex optimization," *Comput. Appl. Math.*, vol. 22, no. 1, pp. 37–52, 2003, doi: 10.1590/s1807-03022003000100003.

[66] E. H. Fukuda, L. M. G. Drummond, and L. M. Graña Drummond, "On the convergence of the projected gradient method for vector optimization," *Optimization*, vol. 60, no. 8–9, pp. 1009–1021, 2011, doi: 10.1080/02331934.2010.522710.

[67] J. Nocedal and S. J. S. Wright, *Numerical Optimization*, 2nd ed. New York: Springer,

2006.

[68] T. Murao, T. Kajitani, H. Yamamura, K. Anzai, K. Oikawa, and T. Sawada, “Simulation of the Center-Line Segregation Generated by the Formation of Bridging,” *ISIJ Int.*, vol. 54, no. 2, pp. 359–365, 2014.

[69] T. Piccone, T. Natarajan, S. Story, B. Jones, and D. Hreso, “Quantitative Methods for Evaluation of Centerline Segregation,” in *AISTech - Iron and Steel Technology Conference Proceedings*, 2016.

[70] Z. Chen, W. Drennan, B. G. Thomas, J. Bentsman, and B. G. Thomas, “Investigating Centerline Bridging in Continuous Casting During Speed Drops with ConOffline,” in *2019 AISTech - Iron and Steel Technology Conference Proceedings*, 2019, no. May, pp. 2075–2084, doi: 10.1000.377.213.

[71] J. B. Dalin and J. L. Chenot, “Finite Element Computation of Bulging in Continuously Cast Steel with a Viscoplastic Model,” *Int. J. Numer. Methods Eng.*, vol. 25, no. 1, pp. 147–163, 1988.

[72] B. Barber, B. A. Lewis, and B. M. Leckenby, “Finiteelement analysis of strand deformation and strain distribution in solidifying shell during condinuous slab casting,” *Ironmak. Steelmak.*, vol. 12, no. 4, pp. 171–175, 1985.

[73] H. Ohno, Y. Miki, and Y. Nishizawa, “Generation mechanism of unsteady bulging in continuous casting-1-Development of method for measurement of unsteady bulging in continuous casting,” *ISIJ Int.*, vol. 56, no. 10, pp. 1758–1763, 2016, doi: 10.2355/isijinternational.ISIJINT-2016-172.

[74] T. J. Manayathara, T.-C. Tsao, and J. Bentsman, “Rejection of Unknown Periodic Load

Disturbances in Continuous Steel Casting Process Using Learning Repetitive Control Approach," *IEEE Trans. Control Syst. Technol.*, vol. 4, no. 3, pp. 259–265, 1996.

[75] M. Dussud, S. Galichet, and L. P. Foulloy, "Application of Fuzzy Logic Control for Continuous Casting Mold Level Control," *IEEE Trans. Control Syst. Technol.*, vol. 6, no. 2, pp. 246–256, 1998.

[76] J. D. Lee and C. H. Yim, "The Mechanism of Unsteady Bulging and its Analysis with the Finite Element Method for Continuously Cast Steel," *ISIJ Int.*, vol. 40, no. 8, pp. 765–770, 2000.

[77] K. Miyazawa and K. Schwerdtfeger, "Computation of bulging of continuously cast slabs with simple bending theory," *Ironmak. Steelmak.*, vol. 6, no. 2, pp. 68–74, 1979.

[78] L. Yu, "FEM Analysis of Bulging Between Rolls in Continuous Casting," University of Illinois Urbana-Champaign, 2000.

[79] U.-S. Yoon *et al.*, "Analysis of Mold Level Hunching by Unsteady Bulging During Thin Slab Casting," *ISIJ Int.*, vol. 42, no. 10, pp. 1103–1111, 2002, doi: 10.2355/isijinternational.42.1103.

[80] J. F. Price, *Lagrangian and eulerian representations of fluid flow: Kinematics and the equations of motion*. 2006.

[81] H. K. Khalil, *Nonlinear Systems*. Upper Saddle, New Jersey: Prentice Hall, 2002.

[1] “Steel Statistical Yearbook 2017.” 2017.

[2] J. Sengupta, B. G. Thomas, and M. A. Wells, “The Use of Water Cooling During the Continuous Casting of Steel and Aluminum Alloys,” *Metall. Mater. Trans. A – Phys. Metall. Mater. Sci.*, vol. 36, no. 1, pp. 187–204, 2005.

[3] Y. A. Meng and B. G. Thomas, “Heat Transfer and Solidification Model of Continuous Slab Casting: CON1D,” *Metall. Mater. Trans. B*, vol. 34, no. 5, pp. 685–705, 2003.

[4] B. Petrus, K. Zheng, X. Zhou, B. G. Thomas, and J. Bentsman, “Real-Time, Model-Based Spray-Cooling Control System for Steel Continuous Casting,” *Metall. Mater. Trans. B*, vol. 42, no. 1, pp. 87–103, 2011, doi: 10.1007/s11663-010-9452-7.

[5] J. K. Brimacombe and K. Sorimachi, “Crack formation in the continuous casting of steel,” *Metall. Trans. B*, vol. 8, no. 2, pp. 489–505, 1977, doi: 10.1007/BF02696937.

[6] J. a. J. A. Sirgo *et al.*, “Measurement of centerline segregation in steel slabs,” *Conf. Rec. - IAS Annu. Meet. (IEEE Ind. Appl. Soc.*, vol. 1, no. c, pp. 516–520, 2006, doi: 10.1109/IAS.2006.256568.

[7] L. Su *et al.*, “Automatic measurement of Centreline segregation in continuously cast line pipe steel slabs,” *Energy Mater. 2014, Conf. Proc.*, no. November, pp. 575–581, 2014, doi: 10.1007/978-3-319-48765-6_70.

[8] G. W. Zuspan, *Basic Metallurgy: Metallurgical equipment and laboratory techniques Ed. by G. William Zuspan*, vol. 2. American Society for Metals, 1957.

[9] K. Fischer, H. Litterscheidt, W. Rudack, R. Simon, and R. Weber, “Industrial experience gathered in the production of continuously cast slabs,” *Thyssen Tech. Berichte*, vol. 10, no. 2, pp. 13–18, 1978.

[10] S. Louhenkilpi, “Chapter 1.8 - Continuous Casting of Steel,” in *Treatise on Process Metallurgy*, Elsevier, 2014, pp. 373–434.

[11] C. a. Hernández-Bocanegra, a. H. Castillejos E., F. a. Acosta-González, X. Zhou, and B. G. Thomas, “Measurement of heat flux in dense air-mist cooling: Part I - A novel steady-state technique,” *Exp. Therm. Fluid Sci.*, vol. 44, pp. 147–160, 2013, doi: 10.1016/j.expthermflusci.2012.06.015.

[12] Z. Chen, J. Bentsman, and B. G. Thomas, “Bang-Bang Free Boundary Control of a Stefan Problem for Metallurgical Length Maintenance,” in *2018 Annual American Control Conference (ACC)*, 2018, pp. 116–121, doi: 10.23919/ACC.2018.8431904.

[13] B. Petrus, J. Bentsman, and B. G. Thomas, “Enthalpy-based Feedback Control Algorithms for the Stefan Problem,” in *51st IEEE Conference on Decision and Control (CDC)*, 2012, pp. 7037–7042, doi: 10.1109/CDC.2012.6426035.

[14] W. B. Dunbar, N. Petit, P. Rouchon, and P. Martin, “Motion planning for a nonlinear Stefan problem,” *ESAIM Control. Optim. Calc. Var.*, vol. 9, pp. 275–296, 2003, doi: 10.1051/cocv.

[15] B. Petrus, J. Bentsman, and B. G. Thomas, “Feedback control of the two-phase Stefan problem, with an application to the continuous casting of steel,” *49th IEEE Conf. Decis. Control*, pp. 1731–1736, 2010.

[16] B. Petrus, J. Bentsman, and B. G. Thomas, “Application of Enthalpy-based Feedback Control Methodology to the Two-sided Stefan Problem,” in *American Control Conference (ACC) 2*, 2014, pp. 1015–1020, doi: 10.1109/ACC.2014.6859062.

[17] A. Maidi and J. P. Corriou, “Boundary geometric control of a linear Stefan problem,” *J.*

Process Control, 2014, doi: 10.1016/j.jprocont.2014.04.010.

[18] S. Koga, M. Diagne, and M. Krstic, "Control and State Estimation of the One-Phase Stefan Problem via Backstepping Design," *IEEE Trans. Automat. Contr.*, vol. 64, no. 2, pp. 510–525, 2019, doi: 10.1109/TAC.2018.2836018.

[19] S. Koga and M. Krstic, "Arctic sea ice state estimation from thermodynamic PDE model," *arXiv Prepr. arXiv1901.10678*, no. January, 2019.

[20] A. Friedman and L.-S. JIANG, "Nonlinear Optimal Control Problems in Heat Conduction," *SIAM J. Control Optim.*, vol. 21, no. 6, pp. 940–952, 1983.

[21] M. Hinze and S. Ziegenbalg, "Optimal Control of the Free Boundary in A Two-Phase Stefan Problem," *J. Comput. Phys.*, vol. 223, no. 2, pp. 657–684, 2007, doi: 10.1016/j.jcp.2006.09.030.

[22] M. Krasnosel'skii and A. V. Pokrovskii, *System with Hysteresis*. Springer-Verlag Berlin Heidelberg, 1989.

[23] J. W. Macki, P. Nistri, and P. Zecca, "Mathematical models for hysteresis," *SIAM Rev.*, vol. 35, no. 1, pp. 94–123, 1993.

[24] A. Visintin, *Differential models of hysteresis*, vol. 111. Springer Science & Business Media, 2013.

[25] G. Tao and P. V Kokotovic, "Adaptive control of plants with unknown hystereses," *IEEE Trans. Automat. Contr.*, vol. 40, no. 2, pp. 200–212, 1995.

[26] G. Song, X. Zhou, J. A. De Abreu-García, and J. Zhao, "Tracking Control of a Piezoceramic Actuator a Piezoceramic Actuator With Hysteresis Compensation Using Inverse Preisach Model," *Trans. Mechatronics*, vol. 10, no. 2, pp. 198–209, 2005.

[27] R. V. Iyer and X. Tan, “Control of hysteretic systems through inverse compensation,” *IEEE Control Syst. Mag.*, vol. 29, no. 1, pp. 83–99, Feb. 2009, doi: 10.1109/MCS.2008.930924.

[28] D. S. D. S. Shook, C. Mohtadi, and S. L. S. L. Shah, “Identification for long-range predictive control,” in *IEE Proceedings D (Control Theory and Applications)*, 1991, vol. 138, no. 1, pp. 75–84, doi: 10.1049/ip-d.1991.0010.

[29] S. Tong and Y. Li, “Adaptive fuzzy output feedback control of MIMO nonlinear systems with unknown dead-zone inputs,” *IEEE Trans. Fuzzy Syst.*, vol. 21, no. 1, pp. 134–146, 2013.

[30] A. Friedman and K.-H. K.-H. Hoffmann, “Control of free boundary problems with hysteresis,” *SIAM J. Control Optim.*, vol. 26, no. 1, pp. 42–55, 1988.

[31] I. G. Götz, K.-H. Hoffmann, and A. M. Meirmanov, “Periodic solutions of the Stefan problem with hysteresis-type boundary conditions,” *Manuscripta Math.*, vol. 78, no. 1, pp. 179–199, 1993.

[32] H. Olia and B. G. G. Thomas, “Flow Rate - Stopper Position Model of NUCOR Caster using Pressure Drop Flow Rate Model for Stopper Rod Flow Control Systems (PFSR),” Golden, Co, 2018.

[33] N. Gregurich, G. Flick, R. Moravec, and K. Blazek, “In-depth Analysis of Continuous Caster Machine Behavior During Casting with Different Roll Gap Taper Profiles,” *Iron Steel Technol.*, vol. 9, no. 12, p. 62, 2012.

[34] L. I. Rubinstein, *The Stefan Problem*. Providence, RI: American Mathematical Society, 1971.

[35] L. C. Evans, *Partial Differential Equations (2nd ed.)*. 2010.

[36] J. R. Cannon and C. D. Hill, “Existence, uniqueness, stability, and monotone dependence in a Stefan problem for the heat equation,” *J. Math. Mech.*, vol. 17, no. 1, pp. 1–19, 1967, doi: 10.1512/iumj.1968.17.17001.

[37] J. R. Cannon and M. Primicerio, “A two phase Stefan problem with flux boundary conditions,” *Ann. di Mat. Pura ed Appl.*, vol. 88, no. 1, pp. 193–205, 1971.

[38] A. Damlamian, “Some results on the multi-phase Stefan problem,” *Commun. Partial Differ. Equations*, vol. 2, no. 10, pp. 1017–1044, 1977, doi: 10.1080/03605307708820053.

[39] Z. Chen, J. Bentsman, B. G. Thomas, and A. Matsui, “Study of spray cooling control to maintain metallurgical length during speed drop in steel continuous casting,” in *Iron and Steel Technology*, 2017, vol. 14, no. 10, pp. 92–103.

[40] K. Harste, “Investigation of the shrinkage and the origin of mechanical tension during solidification and successive cooling of cylindrical bars of Fe–C alloys,” Technical University of Clausthal, 1989.

[41] A. Jablonka, K. Harste, and K. Schwerdtfeger, “Thermomechanical Properties of Iron and Iron-Carbon Alloys: Density and Thermal Contraction,” *Steel Res. Int.*, vol. 62, no. 1, pp. 24–33, 1991.

[42] I. Jimbo and A. A. W. Cramb, “The Density of Liquid Iron-Carbon Alloys,” *Metall. Trans. B*, vol. 24, no. 1, pp. 5–10, 1993.

[43] P. Duvvuri, B. Petrus, and B. G. Thomas, “Correlation for mold heat flux measured in a thin slab casting mold,” in *AISTech - Iron and Steel Technology Conference Proceedings*, 2014, pp. 2881–2893.

[44] J. A. Dantzig and C. L. Tucker, *Modeling in Materials Processing*. Cambridge University Press, 2001.

[45] C. Cicutti, M. Valdez, T. Perez, G. Gresia, W. Balante, and J. Petroni, "Mould Thermal Evaluation in a Slab Continuous Casting Machine," in *Proceedings of the 85th Steelmaking Conference*, 2002.

[46] T. Nozaki, J. Matsuno, K. Murata, H. Ooi, and M. Kodama, "A Secondary Cooling Pattern for Preventing Surface Cracks of Continuous Casting Slab," *Trans. Iron Steel Inst. Jpn.*, vol. 18, no. 6, pp. 330–338, 1978.

[47] B. Petrus *et al.*, "New Method to Measure Metallurgical Length and Application to Improve Computational Models," *Iron Steel Technol.*, vol. 12, no. 12, pp. 58–66, 2015.

[48] L. C. Hibbeler, B. G. Thomas, R. C. Schimmel, and G. Abbel, "The thermal distortion of a funnel mold," *Metall. Mater. Trans. B*, vol. 43, no. 5, pp. 1156–1172, 2012.

[49] R. a. Hardin, K. Liu, C. Beckermann, and A. Kapoor, "A transient simulation and dynamic spray cooling control model for continuous steel casting," *Metall. Mater. Trans. B*, vol. 34, no. 3, pp. 297–306, 2003, doi: 10.1007/s11663-003-0075-0.

[50] Z. Chen, J. Bentsman, and B. G. Thomas, "Optimal Control of Free Boundary of a Stefan Problem for Metallurgical Length Maintenance in Continuous Steel Casting," in *2019 American Control Conference (ACC)*, 2019, pp. 3206–3211.

[51] B. Petrus, Z. Chen, J. Bentsman, and B. G. Thomas, "Online recalibration of the state estimators for a system with moving boundaries using sparse discrete-in-time temperature measurements," *IEEE Trans. Automat. Contr.*, vol. 63, no. 4, pp. 1090–1096, Apr. 2018, doi: 10.1109/TAC.2017.2736950.

[52] C. Saguez, “Optimal control of free boundary problems,” in *System Modelling and Optimization*, Heidelberg: Springer Berlin, 1986, pp. 776–788.

[53] P. Neittaanmaki and D. Tiba, *Optimal Control of Nonlinear Parabolic Systems: Theory, Algorithms, and Applications*. Marcel Dekker, 1994.

[54] W. B. Dunbar, N. Petit, P. Rouchon, and P. Martin, “Boundary control of a nonlinear Stefan Problem,” in *Proceedings ofthe 42nd IEEE Conference on Decision and Control*, 2003, pp. 1309–1314.

[55] O. A. Ladyzenskaja, V. A. Solonnikov, and N. N. Uralceva, *Linear and Quasilinear Equations of Parabolic Type*. American Mathematical Society, 1968.

[56] M. Krstic and A. Smyshlyaev, *Boundary Control of PDEs: A course on Backstepping Designs*. Philadelphia: SIAM, 2008.

[57] J. A. Walker, *Dynamical Systems and Evolution Equations: Theory and Applications*. New York: Plenum Press, 1980.

[58] J. R. Cannon and M. Primicerio, “Remarks on the one-phase Stefan problem for the heat equation with the flux prescribed on the fixed boundary,” *J. Math. Anal. Appl.*, vol. 35, no. 2, pp. 361–373, 1971, doi: 10.1016/0022-247X(71)90223-X.

[59] M. A. Krasnosel’skii and A. V Pokrovskii, *Systems with hysteresis*. Springer Science & Business Media, 2012.

[60] K.-H. K.-H. Hoffmann and J. Sprekels, “Real-time control in a free boundary problem connected with the continuous casting of steel,” in *Optimal Control of Partial Differential Equations*, vol. 68, K.-H. Hoffmann and W. Krabs, Eds. Basel, Switzerland: Birkhauser, 1984, pp. 127–143.

[61] X. Zhou, B. G. Thomas, B. C. A. Hernández, E. a H. Castillejos, and A. F. Acosta G.F.A., "Measuring heat transfer during spray cooling using controlled induction-heating experiments and computational models," *Appl. Math. Model.*, vol. 37, no. 5, pp. 3181–3192, 2013, doi: 10.1016/j.apm.2012.07.039.

[62] X. Zhou and B. G. Thomas, "Continuous Casting Consortium Annual Report 2008: New features of CON1D- Version 9.6," Urbana, 2008.

[63] J. Caldwell and Y. Y. Kwan, "Numerical methods for one-dimensional Stefan problems," *Int. j. numer. method. biomed. eng.*, vol. 20, no. 7, pp. 535–545, 2004, doi: 10.2298/TSCI0902061C.

[64] L. M. G. Drummond, A. N. Iusem, L. M. Graña Drummond, and A. N. Iusem, "A projected gradient method for vector optimization problems," *Comput. Optim. Appl.*, vol. 28, no. 1, pp. 5–29, 2004, doi: 10.1023/B:COAP.0000018877.86161.8b.

[65] A. N. Iusem, "On the convergence properties of the projected gradient method for convex optimization," *Comput. Appl. Math.*, vol. 22, no. 1, pp. 37–52, 2003, doi: 10.1590/s1807-03022003000100003.

[66] E. H. Fukuda, L. M. G. Drummond, and L. M. Graña Drummond, "On the convergence of the projected gradient method for vector optimization," *Optimization*, vol. 60, no. 8–9, pp. 1009–1021, 2011, doi: 10.1080/02331934.2010.522710.

[67] J. Nocedal and S. J. S. Wright, *Numerical Optimization*, 2nd ed. New York: Springer, 2006.

[68] T. Murao, T. Kajitani, H. Yamamura, K. Anzai, K. Oikawa, and T. Sawada, "Simulation of the Center-Line Segregation Generated by the Formation of Bridging," *ISIJ Int.*, vol.

54, no. 2, pp. 359–365, 2014.

[69] T. Piccone, T. Natarajan, S. Story, B. Jones, and D. Hreso, “Quantitative Methods for Evaluation of Centerline Segregation,” in *AISTech - Iron and Steel Technology Conference Proceedings*, 2016.

[70] Z. Chen, W. Drennan, B. G. Thomas, J. Bentsman, and B. G. Thomas, “Investigating Centerline Bridging in Continuous Casting During Speed Drops with ConOffline,” in *2019 AISTech - Iron and Steel Technology Conference Proceedings*, 2019, no. May, pp. 2075–2084, doi: 10.1000.377.213.

[71] J. B. Dalin and J. L. Chenot, “Finite Element Computation of Bulging in Continuously Cast Steel with a Viscoplastic Model,” *Int. J. Numer. Methods Eng.*, vol. 25, no. 1, pp. 147–163, 1988.

[72] B. Barber, B. A. Lewis, and B. M. Leckenby, “Finiteelement analysis of strand deformation and strain distribution in solidifying shell during condinuous slab casting,” *Ironmak. Steelmak.*, vol. 12, no. 4, pp. 171–175, 1985.

[73] H. Ohno, Y. Miki, and Y. Nishizawa, “Generation mechanism of unsteady bulging in continuous casting-1-Development of method for measurement of unsteady bulging in continuous casting,” *ISIJ Int.*, vol. 56, no. 10, pp. 1758–1763, 2016, doi: 10.2355/isijinternational.ISIJINT-2016-172.

[74] T. J. Manayathara, T.-C. Tsao, and J. Bentsman, “Rejection of Unknown Periodic Load Disturbances in Continuous Steel Casting Process Using Learning Repetitive Control Approach,” *IEEE Trans. Control Syst. Technol.*, vol. 4, no. 3, pp. 259–265, 1996.

[75] M. Dussud, S. Galichet, and L. P. Foulloy, “Application of Fuzzy Logic Control for

Continuous Casting Mold Level Control," *IEEE Trans. Control Syst. Technol.*, vol. 6, no. 2, pp. 246–256, 1998.

[76] J. D. Lee and C. H. Yim, "The Mechanism of Unsteady Bulging and its Analysis with the Finite Element Method for Continuously Cast Steel," *ISIJ Int.*, vol. 40, no. 8, pp. 765–770, 2000.

[77] K. Miyazawa and K. Schwerdtfeger, "Computation of bulging of continuously cast slabs with simple bending theory," *Ironmak. Steelmak.*, vol. 6, no. 2, pp. 68–74, 1979.

[78] L. Yu, "FEM Analysis of Bulging Between Rolls in Continuous Casting," University of Illinois Urbana-Champaign, 2000.

[79] U.-S. Yoon *et al.*, "Analysis of Mold Level Hunching by Unsteady Bulging During Thin Slab Casting," *ISIJ Int.*, vol. 42, no. 10, pp. 1103–1111, 2002, doi: 10.2355/isijinternational.42.1103.

[80] J. F. Price, *Lagrangian and eulerian representations of fluid flow: Kinematics and the equations of motion*. 2006.

[81] H. K. Khalil, *Nonlinear Systems*. Upper Saddle, New Jersey: Prentice Hall, 2002.